Doctoral Dissertation

Systematic Study on Electrocatalytic Properties of Perovskite Oxides for Energy Conversion and Storage Systems

Ohhun Gwon

Department of Energy Engineering

(Energy Engineering)

Graduate School of UNIST

2019

Systematic Study on Electrocatalytic Properties of Perovskite Oxides for Energy Conversion and Storage Systems

Ohhun Gwon

Department of Energy Engineering

(Energy Engineering)

Graduate School of UNIST

Systematic Study on Electrocatalytic Properties of Perovskite Oxides for Energy Conversion and Storage Systems

A dissertation
submitted to the Graduate School of UNIST
in partial fulfillment of the
requirements for the degree of
Doctor of Philosophy

Ohhun Gwon

12/28/2018
Approved by

Advisor
Guntae Kim

Systematic Study on Electrocatalytic Properties of Perovskite Oxides for Energy Conversion and Storage Systems

Ohhun Gwon

This certifies that the dissertation of Ohhun Gwon is approved.

12/28/2018

Advisor: Guntae Kim

Jong-Beom Baek

Hu Young Jeong

Jeeyoung Shin

Ikwhang Chang

Abstract

Efficiency, cost and environment-friendly must be considered when developing energy conversion and storage systems such as solid oxide fuel cell (SOFC), metal-air battery (MAB), water splitting, and solar synthetic reactor. Particularly, in terms of efficiency, improvement of catalytic activity for oxygen reduction and evolution reactions (ORR and OER) is most important. To date, noble metal catalysts (such as platinum (Pt), ruthenium oxide (RuO_2), and iridium oxide (IrO_2)) are generally used because of their high catalytic activity. However, it is limited to use the noble metal catalysts for large-scale applications due to their expensive cost and scarcity. In this regard, the simpler and more economical design of bifunctional catalysts will directly benefit efficient energy conversion and storage systems. Recently, it is received enormous attention that the development of transition-metal oxide materials because of their cheap cost and high performances. Among the transition-metal oxide materials, perovskite oxides are reported as exceptional electrocatalysts due to their outstanding catalytic activity, excellent cyclic stability, and high conductivity.

This dissertation focuses on the analysis of the catalytic factors which can affect ORR and OER with perovskite catalysts and develop new perovskite catalyst cathode materials for MAB and SOFC applications. These materials thus can be presented as a promising catalyst with remarkable performances and stabilities. Herein, I introduce my research papers studying perovskite catalysts as following,

1. Conductivity-Dependent Completion of Oxygen Reduction on Oxide Catalysts
2. Major role of surface area in perovskite electrocatalysts for alkaline systems
3. Enhancing Bifunctional Electrocatalytic activities via Metal d-Band-Center-Lift in $Sm_{0.5}Sr_{0.5}CoO_{3-\delta}$ Perovskite
4. Optimization of $La_xSr_{1-x}CoO_{3-\delta}$ perovskite cathodes for intermediate temperature solid oxide fuel cells through the analysis of structural and electrical properties
5. An Efficient Oxygen Evolution Catalyst for Hybrid Lithium Air Batteries: Almond Stick Type Composite of Perovskite and Cobalt Oxide
6. A Highly Efficient and Robust Cation Ordered Perovskite Oxides as a Bi-Functional Catalyst for Rechargeable Zinc-Air Batteries

Contents

List of Figures

slopes (b) by using the relationship: b = 60 mV dec^{-1}/(n_{RDS} α), where the transfer coefficient (α) was assumed to be 0.5. A single catalyst particle (yellow circle) surrounded by multiple carbon black (black circles) represents carbon compositions on the top of (b) and (c).

Figure 2.3 The effects of local potential distribution near the active sites on $n_{overall}$. (a) Potential dependency of $n_{overall}$. The critical overpotentials (η_c) at which the $n_{overall}$ dramatically decreases were indicated. (b) BSCFO and NBSCO as representative examples of less versus more conductive catalysts, respectively. Overpotential (η) gradients decrease with distance away from the contact point with carbon through the body of the catalyst.

Figure 3.1 Powder X-ray diffraction patterns of the cubic perovskite nano-crystallites prepared at different temperatures. (a) PSC calcined at 650 and 750 °C, (b) NSC calcined at 600 and 700 °C, (c) SSC calcined at 650 and 750 °C, and (d) GSC calcined at 700 and 800 °C. While the patterns in black are taken from the nanoparticles obtained at their minimum crystallization temperatures for each lanthanide ion, those in blue are taken from nano-crystallites calcined at 100 °C higher temperatures.

Figure 3.2 FE-SEM images of the (a) PSC-650, (b) PSC-750, (c) NSC-600, (d) NSC-700, (e) SSC-650, (f) SSC-750, (g) GSC-700, and (h) GSC-800. Note the size of each nano-crystallite increases as the calcination temperatures increases.

Figure 3.3 Disc current of (a) ORR and (b) OER measured by LSV with 10 mV s^{-1} scan rate at 1600 rpm.

Figure 3.4 Cobalt 2P XPS spectra of (a) NSC, (b) PSC, (c) SSC, and (d) GSC.

Figure 3.5 (a) Disc current of ORR and (b) disc current of oxygen evolution reaction of NSC 600, 700, 800, and 900, measured by RRDE with 10 mV s^{-1} scan rate at 1600 rpm.

Figure 3.6 Cobalt 2P XPS spectra of (a) NSC 600, (b) NSC 700, (c) NSC 800, and (d) NSC 900.

Figure 4.1 XRD of SSC30, SSC29, and SSC28.

Figure 4.2 SEM images of (a) SSC30, (b) SSC29, and (c) SSC28.

Figure 4.3 Particle size distribution of (a) SSC30, (b) SSC29, and (c) SSC28.

Figure 4.4 N_2 adsorption–desorption isotherms of SSC30, SSC29, and SSC28. The surface area of each samples is 1.75, 1.81 and 1.74 $m^2 g^{-1}$, respectively.

Figure 4.5 (a) ORR and (b) OER activity of the Sm0.5Sr0.5CoO3-δ (δ = 0.0, 0.1, and 0.2) in O2-saturated 0.1 M KOH at a scan rate of 10 mV s−1 and a rotation rate of 1,600 rpm.

Figure 4.6 (a) Disc current, (b) ring current, (c) electrons transfer number, and (d) peroxide yield of ORR are measured by a RRDE test. The test is operated in O_2-saturated 0.1 M KOH at 10 mV s^{-1} scan rate and 1,600 rpm rotation rate from 0.1 V to -0.9 V.

Figure 4.7 (a) Schematic rigid band diagrams of the late transition metal oxide. (b) Variation in the M_d energy levels and the energy level differences between M_d and O_p (ΔE_{d-p}) with the number of oxygen defects in the SSC. All band centers are relative to the Fermi level. (c) The ORR and OER experimental overpotentials of the SSC at −0.5 and 1.0 mA cm^{-2}, respectively.

Figure 4.8 (a) Theoretical ratio of Co ions according to the number of oxygen defects. (b) Experimental ratio of Co ions according to the number of oxygen vacancies measured by XPS (Fig. 4.9). (c) From left to right, intermediate spin states (IS) of Co^{4+}, IS of Co^{3+}, crossover of Co^{2+} between intermediate- and low-spin states (IS/LS), and LS of Co^{3+}. Positive values indicate majority spin states while negative values indicate minority spin states. The black dashed line represents the e_g orbital and the black solid line represents the t_{2g} orbital of the Co 3d orbital. The blue solid line indicates the calculated d-band center (M_d) position. The dashed horizontal line appears at the Fermi level, with occupied states at negative energies and unoccupied states at positive energies.

Figure 4.9 XPS measurements of (a) SSC30, (b) SSC29, and (c) SSC28.

Figure 4.10 (a) The illustration shows the position of oxygen vacancies (V_O) for the various vacancy configurations. The blue, green, and purple circles represent the positions of oxygen vacancies in the 1st, 2nd, and 3rd layers, respectively. (b) Formation energies of oxygen vacancies for the bulk, 1st, 2nd, and 3rd layers. (c) The overpotential and ΔE_{d-p} values of the OER based on the oxygen vacancy position. (d) and (e) The calculated free energy profiles of the ORR and the OER on the (001) surface of SSC under equilibrium potential in alkaline media.

Figure 4.11. The overpotential of three configurations (Voi free, in 1st layer, and in 2nd layer) for LOM pathway are 0.89, 0.60, 0.98 eV, which are relatively high compared to that for AEM pathway. The rate-determining step in all the configurations are third reaction step. Voi represents internal oxygen vacancy existing

the PBSCF-NF. (f) Line scan across the PBSCF-NF from a red line on the nanofiber in (d).

Figure 7.7 OER activities of PBSCF-NF, PBSCF-P, BSCF and IrO_2. (a) Polarization curves of PBSCF-NF, PBSCF-P, BSCF and IrO_2 electrocatalysts in 0.1 M KOH solution at 1600 rpm with 10 mV s^{-1} scan rate. (b) Tafel plots obtained from the polarization curves in (a). (c) Overpotentials of PBSCF-NF, PBSCF-P, BSCF and IrO_2 at a current density of 10 mA cm^{-2}. (d) Currents densities of PBSCF-NF, PBSCF-P, BSCF and IrO_2 at an overpotential of 0.3 V.

Figure 7.8 ORR activity of PBSCF-NF, PBSCF-P, and Pt/C. (a) Polarization curves of PBSCF-NF, PBSCF-P, and Pt/C electrocatalysts in 0.1 M KOH solution. (b) Tafel plots obtained from the polarization curves in (a). (c) The electron transfer numbers of PBSCF-NF, PBSCF-P, and Pt/C at different potentials. (d) H_2O_2 yield of PBSCF-NF, PBSCF-P, and Pt/C. (Electrode rotation speed: 1600 rpm, Scan rate: 10 mV s^{-1}, Catalyst loading = 0.796 mg cm^{-2})

Figure 7.9 Cyclic voltammetry profiles of PBSCF-NF in an O_2-saturated 0.1 M KOH solution with scan rate of 10 mV s^{-1}.

Figure 7.10 the HR-TEM picture after the long stability test.

Figure 7.11 (a) Current density–voltage curves. (b) Power density curves. (c) Discharge curves at a current density of 10 mA cm^{-2} of Zn–air battery using Pt/C, PBSCF-NF and pristine air electrode. (d) Discharge and charge cycling curves of rechargeable Zn–air batteries based on PBSCF-NF and the mixed Pt/C+IrO_2 composite at a current density of 10 mA cm^{-2}.

List of Tables

Explanation of Terms and Abbreviations

1. SOFC: Solid Oxide Fuel Cell
2. MAB: Metal-Air Battery
3. ORR: Oxygen Reduction Reaction
4. OER: Oxygen Evolution Reaction
5. Pt: Platinum
6. RuO_2: Ruthenium Oxide
7. IrO_2: Iridium Oxide
8. IT: Intermediate Temperature
9. *n*: Number of Electron Transfer
10. I_d: Disk Current
11. I_r: Ring Current
12. HO_2^-: Hydrogen Peroxide
13. $K_3[Fe(CN)_6]$: Potassium Ferricyanide
14. RRDE: Rotating Ring-Disk Electrodes
15. *N*: Collection Efficiency
16. i_L: Limiting Current
17. F: Faraday constant (96,487 C mol^{-1})
18. D_O: Diffusion Coefficient of Oxygen
19. C_O: Concentration of Oxygen
20. ν: Kinematic Viscosity of Electrolyte (0.01 cm s^{-1})
21. ω: Electrode-Rotation Rate (rpm)
22. η: Overpotential
23. i_o: Exchange Current
24. α: Transfer Coefficient
25. R: Ideal Gas Constant (8.314 J mol^{-1} K^{-1})
26. T: Absolute Temperature (K)
27. MIEC: Mixed Ionic and Electronic Conductor
28. k_o: Standard Rate Constant
29. BSCF: $Ba_{0.5}Sr_{0.5}Co_{0.8}Fe_{0.2}O_{3-\delta}$
30. LSC: $La_xSr_{1-x}CoO_{3-\delta}$
31. NBSCO: $NdBa_{0.25}Sr_{0.75}Co_2O_{5+\delta}$
32. ICP-AES: Inductively Coupled Plasma Atomic Emission Spectroscopy
33. XRD: X-ray diffraction

34. CV: Cyclic Voltammetry
35. LSV: Linear Sweep Voltammetry
36. GC: Glassy Carbon
37. RHE: Reversible Hydrogen Electrode
38. DFT: Density-Functional Theory
39. BET: Brunauer-Emmett-Teller
40. XPS: X-ray Photoelectron Spectra
41. σ: Electrical Conductivity
42. LnSC: $Ln_{0.5}Sr_{0.5}CoO_{3-\delta}$ (Ln = Pr, Nd, Sm, Gd)
43. FE-SEM: Field Emission Scanning Electron Microscope
44. EDS: Energy Dispersive Spectrometer
45. FE-TEM: Field Emission Transmission Electron Microscope
46. GNP: Glycine-Nitrate Process
47. GDC: Gadolinium doped Ceria ($Ce_{0.9}Gd_{0.1}O_{1.95}$)
48. TGA: Thermogravimetric Analysis
49. TPB: Triple Phase Boundary
50. ASR: Area Specific Resistance
51. KB: Ketjen Black
52. SPB: Super-P Black
53. NSC: $Nd_{1-x}Sr_xCoO_{3-\delta}$
54. Co-NSC: Co_3O_4 and NSC composite
55. DMF: N, N-Dimethylformamide
56. PVP: Polyvinylpyrrolidone, Mw = 1,300,000
57. $LiPF_6$: Lithium Hexafluorophosphate
58. TEGDME: Tetraethylene Glycol Dimethyl Ether
59. LiOH: Lithium Hydroxide
60. LISICON: $Li_{1+x+y}Ti_{2-x}Al_xP_{3-y}Si_yO_{12}$
61. PVdF-HFP: Poly(Vinylidene Fluoride-co-Hexafluoropropylene)
62. HAADF-TEM: High-Angle Annular Dark-Field TEM
63. BF-TEM: Bright-Field TEM
64. K-L plot: Koutechy-Levich plot
65. OCV: open-circuit voltage
66. $O_{lattice}$: Lattice Oxygen
67. O_{ad}: Adsorbed Oxygen Species
68. EV: Electrical Vehicle

69. ESS: Electrical Energy Storage Systems
70. PBSCF: $PrBa_{0.5}Sr_{0.5}Co_{2-x}Fe_xO_{5+\delta}$
71. PBSCF-NF: Mesoporous $PrBa_{0.5}Sr_{0.5}Co_{2-x}Fe_xO_{5+\delta}$ Nanofiber
72. PAN: Polyacrylonitrile
73. PTFE: Polytetrafluoroethylene
74. HR-TEM: High-Resolution TEM
75. EELS: Electron Energy-Loss Spectroscopy
76. PBSCF-P: Bulk $PrBa_{0.5}Sr_{0.5}Co_{2-x}Fe_xO_{5+\delta}$ Powder

Chapter I. Introduction

1.1 Motivation Statements

As growing global energy demand requires, the importance of development of advanced energy conversion systems is also increasing due to their environment-friendly process, low cost and high-energy density. Solid oxide fuel cell (SOFC) and metal-air battery (MAB) are clean and sustainable energy conversion devices compared with fossil fuel energy devices.[1-3] Especially, to alternate fossil fuel energy devices, it is necessary to improve their electrical performances and energy efficiency. To secure the high electrical performances, noble metal catalysts (Pt, IrO_2, RuO_2, etc.) are commonly used because of their high catalytic activity. However, noble metal-based catalysts interfere with large-scale applications due to their rarity and high cost. To overcome the problem, it is necessary to develop new bifunctional catalysts, which composed of non-precious elements, for oxygen reduction and oxygen evolution reactions (ORR and OER).[4-7] In recent years, it has actively researched and developed that inexpensive electrode catalyst using a transition metal as a raw material.[8-15] Among the transition metal-based materials, particularly, perovskite-type structures have shown synergistic catalytic activities with high efficiency for both ORR and OER.[16-18] The perovskite oxides composed of rare earth or alkali metal at the A-site and transition metal at the B-site, and they have been applicable as a electrocatalyst for advanced energy conversion systems.[19-25]

This manuscript concentrates on to figure out the relationships between controlling factors (electrical conductivity, surface area, microstructural morphology, A-site dopant, and B-site dopant) and catalytic properties of perovskite oxides. Furthermore, this manuscript introduces newly developed perovskite oxide catalysts for SOFC and MAB.

1.1 Kinetics and mechanism of the ORR and OER

The ideal ORR and OER in an alkaline solution involve a four-electron transfer pathway described by equation (1.1.1).

$$O_2 + 4e^- + 2\,H_2O \rightleftarrows 4\,OH^- \qquad (n = 4) \qquad (1.1.1)$$

In contrast, a two-electron transfer pathway is partly responsible for the ORR current; does not complete a turnover of the ORR but generates peroxide as an intermediate product. [6–11]

$$O_2 + 2e^- + 2\,H_2O \rightarrow HO_2^- + OH^- \qquad (n = 2) \qquad (1.1.2)$$

Number of electron transfer (n):

The disk currents (I_d) result from both 4e and 2e ORR processes. Hydrogen peroxide (HO_2^-) is produced only from the 2e ORR process, which is detected on the ring electrode (I_r) by re-oxidizing the hydrogen peroxide. Therefore, both n and the amounts of peroxide production (HO_2^- %) are determined by comparing the values of I_d and I_r at the same moment via the following equations;

$$n = 4 \times \frac{I_d}{I_d + I_r/N} \qquad (1.1.3)$$

$$HO_2^-(\%) = 200 \times \frac{I_r/N}{I_d + I_r/N} \qquad (1.1.4)$$

where *N* is the collection efficiency as a measure of a fraction of hydrogen peroxide produced on disk electrode to be detected on ring electrode. The value of *N* for the RRDE we used was measured by using 10 mM aqueous electrolyte of potassium ferricyanide ($K_3[Fe(CN)_6]$) in 0.1M KOH in a three electrode configuration (RRDE as the working electrodes, Pt wire as the counter electrode and Hg/HgO as the reference). The disk potential was swept from 0.6 V to -0.5 V at various rotating speeds while the ring potential was fixed at 0.6V. The *N* value estimated by the ratio of the limiting ring current to the limiting disk current was determined at 0.412, which was close to 0.424 that is the theoretically calculated value based on the dimension and geometry of our RRDE.

Levich equation:

Levich equation models the diffusion and solution flow conditions around the RRDE. The Levich equation is as follows;

$$i_L = 0.62\ n\ F\ A\ D_O^{2/3}\ \omega^{1/2}\ \nu^{-1/6}\ C_O^* \qquad (1.1.5)$$

where i_L is limiting current, n is overall electron transfer number, F is Faraday constant (96,487 C mol^{-1}), A is geometric area of electrodes, D is diffusion coefficient of oxygen, C is concentration of O_2 in the aqueous solution (mol L^{-1}), ν is kinematic viscosity of electrolyte (0.01 cm s^{-1}), and ω is electrode-rotation rate (rpm).

Tafel equation:

The Tafel equation is an electrochemical kinetics equation that relates the electrochemical reaction rate to the overvoltage. The Tafel equation can be stated as;

$$\eta = a + b \log i \qquad (1.1.6)$$

$$a = \ln i_o / (\alpha * n * f) \qquad (1.1.7)$$

$$b = -2.3 / (\alpha * n * f) \qquad (1.1.8)$$

$$f = F / RT \qquad (1.1.9)$$

where F is Faraday constant, η is overpotential, i is current, i_o is exchange current, n is number of electron transfer, α is transfer coefficient, R is ideal gas constant (8.314 J mol^{-1} K^{-1}), and T is absolute temperature (K).

1.2 Solid Oxide Fuel Cell (SOFC)

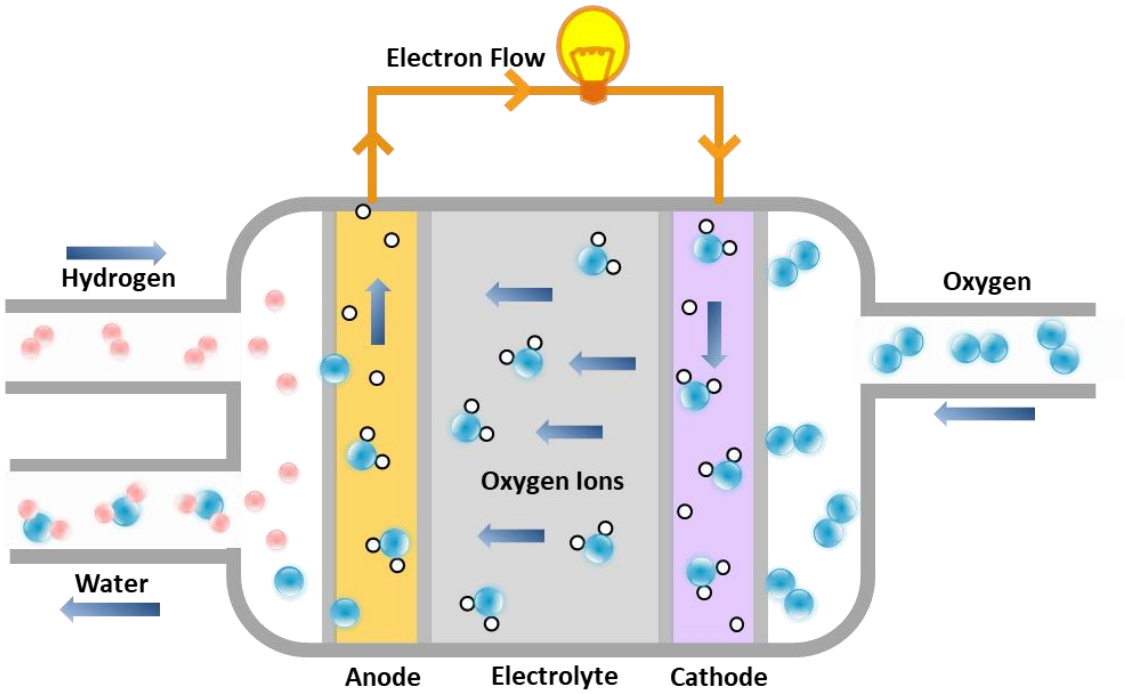

Figure 1.1 Schematic illustration of solid oxide fuel cell.

Solid oxide fuel cell (SOFC) is a kind of fuel cell which use solid oxide materials as the electrodes and electrolyte. Recently, the SOFC has been actively studied as a new generation device due to their high conversion efficiency, eco-friendliness, and fuel flexibility. As shown in the Fig. 1.1 The solid oxide electrolyte conduct oxygen ions from the cathode to the anode. The overall cell reactions of fuel cells are given in equation as follow,

Anode reaction:	$2H_2 + 2O^{2-} \rightarrow 2H_2O + 4e^-$	(1.2.1)
Cathode reaction:	$O_2 + 4e^- \rightarrow 2O^{2-}$	(1.2.2)
Overall cell reaction:	$2H_2 + O_2 \rightarrow 2H_2O$	(1.2.3)

The SOFCs are typically operated at high operating temperature (1073-1273 K), leading some problems such as high operating costs, sealing problem from thermal expansion mismatch, and the electrode, and unexpected reactions between the electrolyte and the electrode.

Therefore, recent researches of SOFC are focused on the intermediate temperature (IT) operation ranging (773-923 K). The lower operating temperature was solved the problems, however, the catalytic activities of cathode and anode materials also decreased significantly with lower temperature. Thus, the development of efficient electrode materials at intermediate temperatures is believed to be

important in improving the performance of IT-SOFC devices.[26-33] The suitable electrode material for IT-SOFCs should have high electronic conductivities, ionic conductivities, and catalytic activities. Mixed ionic and electronic conductor (MIEC) is one of candidate of electrode material for IT-SOFC which has the capability to conduct oxygen ions and electrons simultaneously are strong candidates.

To understand the ORR at the cathode of SOFC, it is important to know that ORR occurs only at electrochemical reaction site, called triple-phase boundary (TPB), where the electronic conductor, ionic conductor, and gas contact. A schematic illustration of of electrochemical reaction at TPB is shown in Fig. 1.2.

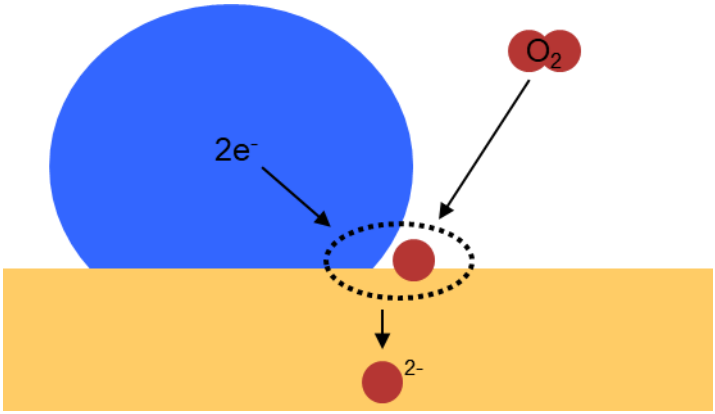

Figure 1.2 Schematic illustration of electrochemical reaction at triple-phase boundary (TPB)

However, the TPB concept is insufficient to explain mechanism of SOFC, due to another ORR-related factors such as interfacial kinetics, surface transport, and chemisorption. The electrochemical reduction operates in a series of electrochemical process resulting in the production of oxygen ions; adsorption, dissociation, surface diffusion, and charge transfer.[34] The electrochemical reduction of the oxygen molecule is expressed as;

$$O_{2,\,gas} + 2V_O^{\bullet\bullet} + 4e' \rightarrow 2O_O^x \qquad (1.2.4)$$

where, $V_O^{\bullet\bullet}$ is oxygen-vacant site and O_O^x is oxygen-ion in the regular oxygen site, in Kroger-Vink notation. As shown in the equation (1.2.4), the ORR not only requires the oxygen and electrons but also the transport ability to carry the generated oxygen ions from the reaction site to the inside of the bulk electrolyte. Furthermore, the cathode material should also have compatibility with the other cell components, and chemical and structural stability at high temperatures and in oxidizing atmosphere.

To enhance the explanation of the mechanism, Adler *et al*. reported continuum model of the ORR mechanism at porous mixed-conducting cathode.[35] This ALS model provides a mechanism whereby oxygen molecules are chemically reduced at the gas/mixed conductor interface and transported

through the mixed conductor by solid state diffusion. The chemical exchange of oxygen at the gas/mixed conductor interface was considered as non-charge transfer process. Figure 1.3 presented the summary of oxygen reduction mechanisms, which is well known as the rate-determining of the oxygen reduction at the cathodes.

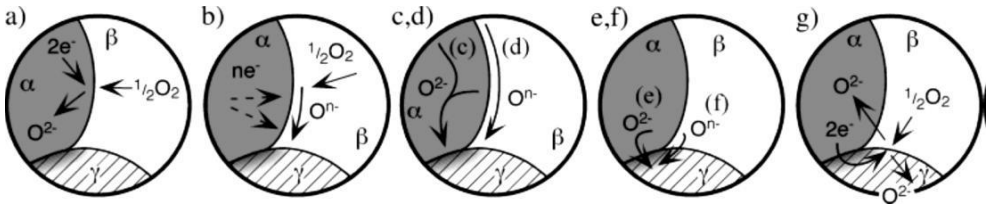

Figure 1.3 Some mechanisms thought to govern oxygen reduction in SOFC cathodes. Phases α, β, and γ refer to the electronic phase, gas phase, and ionic phase, respectively: (a) Incorporation of oxygen into the bulk of the electronic phase (if mixed conducting); (b) adsorption and/or partial reduction of oxygen on the surface of the electronic phase; (c) bulk or (d) surface transport of O^{2-} or O^{n-}, respectively, to the α/γ interface, (e) Electrochemical charge transfer of O^{2-} or (f) combinations of O^{n-} and e^{-}, respectively, across the α/γ interface, and (g) rates of one or more of these mechanisms wherein the electrolyte itself is active for generation and transport of electro-active oxygen species.[35]

1.3 Metal-Air Battery (MAB)

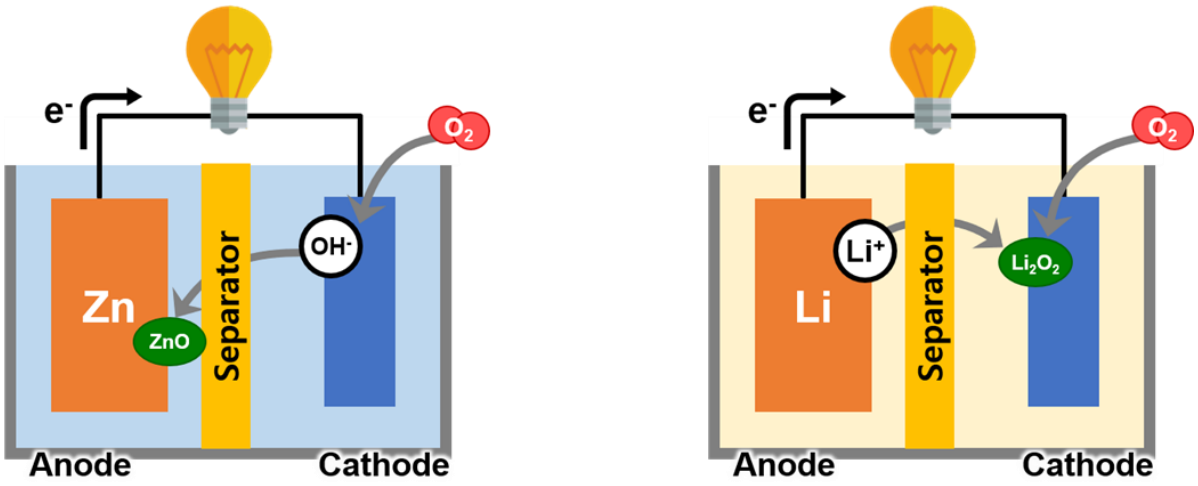

Figure 1.4 Schematic illustration of metal-air batteries.

Metal-air batteries (MABs) have been received as a next-generation energy conversion and storage device due to their high energy density. A noteworthy feature of metal-air batteries is the open-cell structure, because these batteries use oxygen gas from the air as a cathode material. Generally, metal air batteries are divided into two types depending on the electrolyte; water-based electrolyte and aprotic solvent-based electrolyte cell system (aqueous and aprotic systems). Metal-air batteries can apply various metals as anode such as Li, Na, Mg, Fe, Al, Zn, etc. Among various metals, Al, Fe, and Zn are appropriate for the aqueous system, and Li, Na, and Mg are suite for the aprotic system.[36]

Table 1.1 Characteristics of metal-air batteries.

Metal	Theoretical Specific Energy (of metal, Wh kg^{-1})	Theoretical Specific Energy (of cell, Wh kg^{-1})	Calculated Open-Circuit Voltage (V)
Li	13000	5200	2.91
Ca	4600	3000	3.12
Mg	6800	2800	2.93
Al	8100	4300	1.2
Zn	1400	1100	1.65
Fe	2000	1400	1.3

As shown in the Fig. 1.4, the Li and Zn are representative anode metals, which have different operation mechanism for each air battery systems.

For the Li-air battery, Li ions move through electrolyte when performing Li-air battery. In an aprotic electrolyte Li-air battery, it is operated through following reduction reaction at the cathode;

$Li^+ + e^- + O_2 \rightarrow LiO_2$	E^o= 3.0 V vs. Li/Li^+	(1.3.1)
$2LiO_2 \rightarrow Li_2O + O_2$	(chemical reaction)	(1.3.2)
$Li^+ + e^- + LiO_2 \rightarrow Li_2O_2$	E^o= 2.96 V vs. Li/Li^+	(1.3.3)
$2Li^+ + e^- + Li_2O_2 \rightarrow 2Li_2O$	E^o= 2.91 V vs. Li/Li^+	(1.3.4)

Therefore, the open-circuit voltage (OCV) of Li-air battery is determined by cathode reduction reaction.

On the other hand, in the case of Zn-air battery, oxygen hydroxide ions (OH^-) move through electrolyte when operating Zn-air battery. The reaction equations are notated as;

Anode:	$Zn \rightarrow Zn^{2+} + 2e^-$		(1.3.5)
	$Zn^{2+} + 4OH^- \rightarrow Zn(OH)_4^{2-}$	(E^o= −1.25 V vs. NHE)	(1.3.6)
	$Zn(OH)_4^{2-} \rightarrow ZnO + H_2O + 2OH^-$		(1.3.7)
Cathode:	$O_2 + 2H_2O + 4e^- \rightarrow 4OH^-$	(E^o= 0.4 V vs. NHE)	(1.3.8)
Overall reaction:	$2Zn + O_2 \rightarrow 2ZnO$	(E^o= +1.65 V)	(1.3.9)

Therefore, the open-circuit voltage (OCV) of Zn-air battery is determined by cathode reduction and anode oxidation reactions.

1.4 Perovskite Oxide

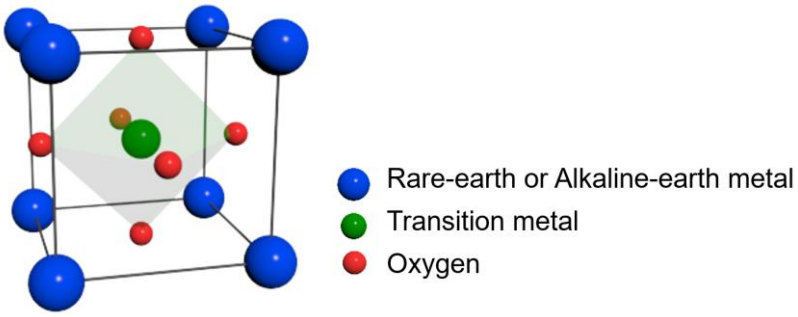

Figure 1.5 Unit cell structure of perovskite oxide.

The perovskite oxide is one kind of mixed ionic and electronic conductor (MIEC), containing rare-earth or alkaline-earth metal as A-site dopant and transition metal as B-site dopant.[27, 30] Among the various perovskite oxides, cobalt containing perovskite oxides ((A, A')CoO_3, A= lanthanides, A'= Sr, Ba, Ca, etc.) have received enormous interest due to their high electrocatalytic activity for oxygen reduction and evolution reactions.[37-39]

For SOFC devices, the high performance of perovskite oxides was explained by their high catalytic activity, high electrical conductivity, high ionic conductivity, and structural stability. The high oxygen vacancy concentration in perovskite oxides not only facilitates migration of oxygen species on the surface but also inside of bulk of the electrode material.[40] On the other hand, for MAB devices, the high performance of perovskite oxides was explained without ionic conductivity. Because, the catalytic reactions only occur on the surface of perovskite oxides in room-temperature condition. According to the previous reports, the oxygen ion diffusion coefficients was experimentally measured by means of the isotopic exchange depth profile method (IEDP). As shown in the table1.2, the $La_{0.5}Sr_{0.5}CoO_{3-\delta}$ sample has diffusion coefficient of $2.6 * 10^{-9}$ and $2.0 * 10^{-21}$ cm^2 s^{-1} at 600 and 25 °C, respectively.[41]

Table 1.2 Diffusion coefficients of $La_{0.5}Sr_{0.5}CoO_{3-\delta}$.

Composition	Temperature (°C)	Diffusion Coefficient (D^*, cm^2 s^{-1})
$La_{0.5}Sr_{0.5}CoO_{3-\delta}$	600	$2.6 * 10^{-9}$
	25	$2.0 * 10^{-21}$

* For 25 °C, D^* was extrapolated from high-temperature values

This result implies and supports that the perovskite oxides only has enough ionic diffusivity in high temperature range rather than room-temperature condition.

The perovskite oxides have flexibility in terms of doping, we can easily control the intrinsic properties of perovskites (such as electrical conductivity, ionic conductivity, and catalytic activities) with changing the dopants in A and B cations. As shown in the Fig. 1.3, the mixture of rare-earth metals (generally lanthanides) and alkaline-earth metals (such as Sr, Ca, and Ba) usually occupies A-site. While, the transition metals (such as Mn, Co, Fe, and Ni) occupies B-site with one or several mixed-valence.[42]

When Ba partially doped in A' as substitution for A-site, the unit cell structure of perovskite oxide is changed to layered perovskite oxide ($LnBaB_2O_{5+\delta}$, where Ln= La, Pr, Nd, Sm, etc., B= Co, Mn, Fe, etc.). The layered perovskite oxide has the same architecture with simple perovskite oxide (ABO_3) as 12-coordinate A-sites and 6-coordinate B-site. However, A-site cations (Ln and Ba) make an ordered structure along the C-axis described as a stacking sequence of

... CoO_2/BaO/CoO_2/LnO_x/CoO_2/BaO/CoO_2/LnO_x …

as shown in the Fig 1.6.

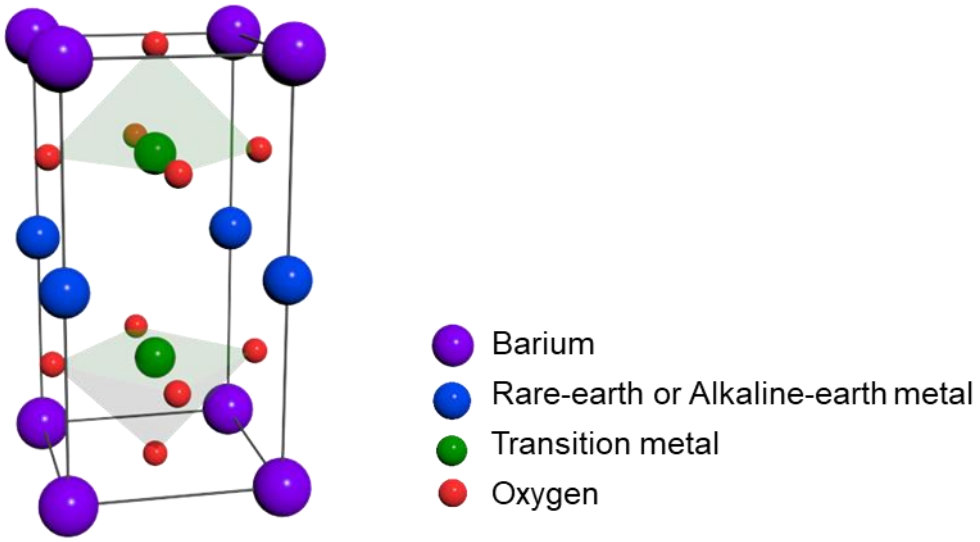

Figure 1.6 Unit cell structure of layered perovskite oxide.

The layered perovskite structure reduces the oxygen bonding strength in the [AO] layer and provides a disorder-free channel for ion motion, leading to all mobile oxygen ions are only migrated through the Ln-O plane. Moreover, the reduced oxygen bonding strength in the [AO] layer also enhances oxygen diffusivity.[32, 43] Nowadays, layered perovskite oxides have attracted interest due to their higher surface exchange coefficient and chemical diffusion compared with those of simple perovskite oxides.

References

1. R. Padbury, X. Zhang, J. Power Sources. 2011, 196, 4436-4444.

2. Z. L. Wang, D. Xu, J. J. Xu, X. B. Zhang, Chem. Soc. Rev. 2014, 43, 7746-7786.

3. Y. Jin, L. Wang, Q. Jiang, X. Du, C. Ji, X. He, Mater. Lett. 2016, 168, 166-170.

4. D. U. Lee, P. Xu, Z. P. Cano, A. G. Kashkooli, M. G. Park, Z. Chen, J. Mater. Chem. A. 2016, 4, 7107-7134.

5. J. -H. Kim, A. Ishihara, S. Mitsushima, N. Kamiya, and K. -I. Ota, Electrochim. Acta. 2007, 52, 2492–2497.

6. G. Faubert, R. Côté, D. Guay, J.P. Dodelet, G. Dénès, C. Poleunis, and P. Bertrand, Electrochim. Acta. 1998, 43, 1969–1984.

7. B. Wang, J. Power Sources. 2005, 152, 1–15.

8. Y. Liang, Y. Li, H. Wang, J. Zhou, J. Wang, T. Regier, H. Dai, Nat. Mater. 2011, 10, 780–786.

9. Y. Gorlin, T. F. Jaramillo, J. Am. Chem. Soc. 2010, 132, 13612–13614.

10. Y. Gorlin, D. Nordlund, T. F. Jaramillo, ECS Trans. 2013, 58, 735–750.

11. Q. Liu, J. Jin, J. Zhang, ACS Appl. Mater. Interfaces 2013, 5, 5002–5008.

12. X. Cao, C. Jin, F. Lu, Z. Yang, M. Shen, R. Yang, J. Electrochem. Soc. 2014, 161, H296–H300.

13. Y. Meng, W. Song, H. Huang, Z. Ren, S. Chen, S. L. Suib, J. Am. Chem. Soc. 2014, 136, 11452–11464.

14. S. Yoo, A. Jun, Y. Ju, D. Odkhuu, J. Hyodo, H. Y. Jeong, N. Park, J. Shin, T. Ishihara, G. Kim, Angew. Chemie Int. Ed. 2014, 13064–13067.

15. S. Sengodan, S. Choi, A. Jun, T. H. Shin, Y.-W. Ju, H. Y. Jeong, J. Shin, J. T. S. Irvine, G. Kim, Nat. Mater. 2014, 14, 205–209.

16. J. Suntivich, H. a Gasteiger, N. Yabuuchi, H. Nakanishi, J. B. Goodenough, Y. Shao-Horn, Nat. Chem. 2011, 3, 546–550.

17. K. J. May, C. E. Carlton, K. a. Stoerzinger, M. Risch, J. Suntivich, Y.-L. Lee, A. Grimaud, Y. Shao-Horn, J. Phys. Chem. Lett. 2012, 3, 3264–3270.

18. A. Grimaud, C. E. Carlton, M. Risch, W. T. Hong, K. J. May, Y. Shao-Horn, J. Phys. Chem. C 2013, 117, 25926–25932.

19. Y. Zhu, W. Zhou, Z. G. Chen, Y. Chen, C. Su, M. O. Tade, Z. Shao, Angew. Chem. Int. Ed. 2015, 54, 3897−3901.

20. J. Suntivich, K. J. May, H. A. Gasteiger, J. B. Goodenough, Y. Shao-Horn, Science. 2011, 334, 1383−1385.

21. A. Grimaud, K. J. May, C. E. Carlton, Y. L. Lee, M. Risch, W. T. Hong, J. Zhou, Y. Shao-Horn, Nat. Commun. 2013, 4, 2439.

22. D. G. Lee, O. Gwon, H. S. Park, S. H. Kim, J. Yang, S. K. Kwak, G. Kim, H. K. Song, Angew.

Chem. Int. Ed. 2015, 54, 15730−15733.

23. O. Gwon, C. Kim, O. Kwon, H. Y. Jeong, H. K. Park, J. Shin, Y. W. Ju, G. Kim, J. Electrochem. Soc. 2016, 163, A1893−A1897.

24. C. Hwang, O. Gwon, H. Jo, K. M. Ok, G. Kim, ChemElectroChem. 2017, 4, 468−471.

25. D. Chen, C. Chen, Z. M. Baiyee, Z. Shao, F. Ciucci, Chem. Rev. 2015, 115, 9869−9921.

26. Z. Shao, S. M. Haile, J. Ahn, P. D. Ronney, Z. Zhan, S. A. Barnett, Nature. 2005, 435, 795–798.

27. A. J. Jacobson, Chem. Mater. 2010, 22, 660–674.

28. B. C. H. Steele, A. Heinzel, Nature. 2001, 414, 345–352.

29. S. Park, J. M. Vohs, R. J. Gorte, Nature. 2000, 404, 265–267.

30. S. Choi, J. Shin, G. Kim, J. Power Sources. 2012, 201, 10–17.

31. T. Hibino, A. Hashimoto, T. Inoue, J. -I. Tokuno, S. -I. Yoshida, M. Sano, Science. 2000, 288, 2031–2033.

32. S. Choi, S. Yoo, J. Kim, S. Park, A. Jun, S. Sengodan, J. Kim, J. Shin, H. Y. Jeong, Y. Choi, G. Kim, Sci. Rep. 2013, 3, 2426.

33. T. V. Aksenova, L. Y. Gavrilova, A. A. Yaremchenko, V. A. Cherepanov, V. V. Kharton, Mater. Res. Bull. 2010, 45, 1288–1292.

34. C. K. Dyer, P. T. Moseley, Z. Ogumi, D. A. J. Rand, B. Scrosati, Encyclopedia of electrochemical power sources. Newnes, 2013.

35. H. Rickert, Electrochemistry of solids Springer Berlin. New York, Heidelberg, 1982.

36. J. -S. Lee, S. T. Kim, R. Cao, N. -S. Choi, M. Liu, K. T. Lee, J. Cho, Adv. Energy Mater. 2010, 1, 34-50.

37. J. A. Kilner, M. Burriel, Annu. Rev. Mater. Res. 2014, 44, 365-393.

38. B. Liu, X. Chen, Y. Dong, S. S. Mao, M. Cheng, Adv. Energy. Mater. 2011, 1, 343-346.

39. C. Xia, W. Rauch, F. Chen, M. Liu, Solid State Ion. 2002, 149, 11-19.

40. J. H. Kim, A. Manthiram, J. Electrochem. Soc. 2008, 155, 4, B385-B390.

41. R. A. De. Souza, J. A. Kilner, Solid State Ion. 1998, 106, 175–187.

42. A. A. Taskin, A. N. Lavrov, Y. Ando, Appl. Phys. Lett., 2005, 86, 090910-090913.

43. A. A. Taskin, A. N. Lavrov, Y. Ando, Prog. Solid State Chem. 2007, 35, 481-490.

Chapter II. Conductivity-Dependent Completion of Oxygen Reduction on Oxide Catalysts

Angewandte Chemie International Edition: Dong-Gyu Lee,[†] Ohhun Gwon,[†] Han-Saem Park, Su Hwan Kim, Juchan Yang, Sang KyuKwak, Guntae Kim,[*] and Hyun-Kon Song[*]: Conductivity-Dependent Completion of Oxygen Reduction on Oxide Catalysts. Angew. Chem. 2015. 127. 15956-15959.

2.1 Introduction

Electron conduction to electroactive sites is one of the necessary requirements for electrochemical reactions on electrodes in which the electroactive sites were immobilized. The statement sounds evident when considering a counter-extreme case that an active site embedded in an insulating matrix would not work for electrochemical reactions. Introducing conducting materials, such as carbon particles, to electrodes has proved helpful as a support for electrocatalysts in fuel cells (for example, platinum supported by carbon, or Pt/C), dye-sensitized solar cells, and as a conducting agent for lithium ion battery electrodes.[1-12] It should be carefully considered which factors determining reaction rates or currents are affected by the electron pathway development increasing electron conduction throughout electrodes. Increasing the number of electroactive sites (as an extensive property) connected to the electric pathways is probably the primary reason for improvements in reaction rate.[13, 14] Decreases in ohmic loss leading to macroscopic potential drop is the second reason.[15, 16] On the other hand, it is not clear whether the electron conduction affects intrinsic or intensive parameters characterizing electron transfer reactions. Rather, it is difficult to imagine that the standard rate constant (k_o in $k = k_o \exp(-\alpha nF\eta/RT)$ from the Butler-Volmer equation, and not the exchange current (i_o)and the number of electron transfer (n) on each active site change with more conductive environments.[17] In this work, we demonstrate that the intrinsic parameters of electron transfer varies by tuning electron conduction. The intrinsic and intensive parameters of interest here, which are independent of the number of active sites, are the number of electrons transferred for the overall process ($n_{overall}$)and rate-determining step (n_{RDS})

2.2 Experimental

2.2.1 Material Preparation

Perovskite oxide catalysts (BSCFO, LSCO and NBSCO) were synthesized by sol-gel method. Stoichiometric amounts of precursors ($Nd(NO_3)_3 \cdot 6H_2O$, $Ba(NO_3)_2$, $Sr(NO_3)_2$, $Co(NO_3)_2 \cdot 6H_2O$, $Fe(NO_3)_3 \cdot 9H_2O$ and $La(NO_3)_3 \cdot 6H_2O$) were dissolved in distilled water with proper amount of Pluronic F-127. All chemicals were used as received from Aldrich. The solution was dried in the oven at 100 ºC for one day. The precursor gel was heated up to 300 ºC in air. Fine powders obtained during the combustion were calcined at 600 ºC for 4 h and then annealed in air at 950 ºC for 4 h. For measuring intrinsic electrical conductivity, the powder was pressed into pellets at 5 MPa and sintered in air at 1100 ºC for 12 h instead of the thermal treatment at 950 ºC for 4 h to achieve a relative density higher than 95%. There were no significant differences of crystallographic structures and oxygen non-stoichiometry between the powder samples annealed at 950 ºC and the pellet samples sintered at 1100 ºC. The value of δ of the as-synthesized NBSCO ($NdBa_{0.25}Sr_{0.75}Co_2O_{5+\delta}$ with $\delta = 0.9$) was tuned from 0.9 to 0.93 by thermal treatment at 800 ºC for 4hr in oxygen atmosphere.

2.2.2 Physicochemical Characterization

The elemental compositions of perovskite materials were characterized by inductively coupled plasma atomic emission spectroscopy (ICP-AES). Their oxygen non-stoichiometry (δ) was measured by iodometric titration. The crystallographic structures of materials were characterized at a scan rate of 0.6 ° min^{-1} with the 2θ range of 20 ° to 60 ° by X-ray diffraction (XRD; Rigaku diffractometer D/MAZX 2500V/PC with Cu Kα radiation). Electrical conductivities were measured in air by a four-point probe configuration. Ag wires as probes were connected to samples by Ag paste. The current/voltage was controlled/measured by a potentiostat (BioLogic VMP3) in a temperature range of 25 to 700 ºC.

2.2.3 Electrode Preparation

Catalyst inks were prepared by dispersing a catalyst and a conducting agent in 0.45 ml of ethanol, 0.45 ml of isopropyl alcohol and 0.1 ml of 5 wt. % nafion solution (Sigma-Aldrich 274704). The total amount of the catalyst and the conducting agent was fixed at 20 mg. Carbon black (C; Akzo Nobel Ketjenblack 600JD) was used as the conducting agent at 0, 5, 20 and 50 wt. %. 5 ul of the catalyst ink was dropped on the disk compartment of ring-disk electrodes. Loading density of the composite of catalyst and conducting agent was fixed at 0.8 mg cm^{-2}. For comparison, 20 wt. % platinum nanoparticles supported by carbon black (Pt/C; Premetek P10A200) was used as a control.

2.2.4 Electrochemical Characterization

Cyclic and linear sweep voltammograms (CVs and LSVs) were obtained on disk and ring electrodes simultaneously by a bipotentiostat (iviumstat, Ivium Technologies). Ring-disk electrodes (RRDE) of glassy carbon disk and platinum ring was used as the working electrode (disk area = 0.1256 cm^2) while a platinum wire and a Hg/HgO electrode were used as the counter and reference electrodes respectively. The RRDEs were rotated at various controlled speeds (1600 rpm unless otherwise indicated) by a RRDE controller (ALS RRDE-3A). An aqueous solution of 0.1M KOH was used as the electrolyte. ORR polarization curves were obtained on the disk electrode from a cathodic sweep from +0.1 V to -0.7 V (vs. Hg/HgO) at 10 mV s^{-1} after five cycles of CVs. The electrolyte was saturated by oxygen for ORR while it was purged by nitrogen to measure background currents. +0.4 V was applied to the ring electrode to estimate the amount of peroxide generated from the disk electrode. The polarization curves were selected at the 5th scan of voltammetry after confirming that the voltammograms did not significantly change during the initial ten cycles. The ORR stability of the perovskite oxide catalysts used in this work were guaranteed by the long-term cycle tests. The values of potential were converted from versus Hg/HgO to versus the reversible hydrogen electrode (RHE) by: Hg/HgO + 0.929 V = RHE. For the correction, the potential difference between Hg/HgO and RHE was measured in a cell where platinum wires were used as the working and counter electrodes in a hydrogen-saturated aqueous electrolyte of 0.1 M KOH with Hg/HgO as the reference electrodes. The open circuit potential was read at -0.929 V vs. Hg/HgO from LSV at 1 mV s^{-1}.

2.2.5 Simulation Models

Cambridge Serial Total Energy Package (CASTEP) is used to calculate NBSCO ($NdBa_{0.25}Sr_{0.75}Co_2O_6$), PBSCO ($PrBa_{0.25}Sr_{0.75}Co_2O_6$), NBCO ($NdBaCo_2O_6$) and BSCFO ($Ba_{0.5}Sr_{0.5}Co_{0.8}Fe_{0.2}O_3$) spin-polarized electronic properties in this study. The cell size of 2×2×2 is used for NBSCO, PBSCO and NBCO.[18] The cell symmetry of NBSCO, PBSCO and NBCO is P4/MMM. Generalized-gradient approximation (GGA) with Perdew, Burke and Ernzerhof (PBE) functional and ultrasoft pseudopotential are used.[19-21] The Broyden–Flecher–Goldfarb–Shanno (BFGS) algorithm is used for the geometry optimization.[22] NBSCO and PBSCO are optimized with fixed lattice parameter and NBCO is optimized with unfixed lattice parameter with 500GPa of compressibility since NBCO was made by changing Sr atom to Ba atom in NBSCO. For geometry optimization, convergence thresholds for the maximum energy change were set to be 1×10^{-5} eV/atom (for fixed lattice) and 5×10^{-5} eV/atom (for unfixed lattice). Convergence thresholds for maximum force, stress, and displacement were set to be 0.03 eV/Å, 0.05 GPa, and 0.001 Å, respectively. The energy cutoff was set to be 500 eV for the fixed lattice parameter and 400 eV for optimizing lattice parameter. Convergence tolerance for the single atomic energy was set to be and 1×10^{-5} eV/atom. The sampling of the Brillouin Zone was

done with the Monkhorst-Pack scheme and for the integration, the number of k points of 2×2×2 were used.[9, 23] For BSCFO, the perovskite unit cell was used with the mixed atom method and its symmetry was PM3M. Lattice parameters were fixed, and other calculation method were same as fixed lattice system except for k points set (i.e. 4×4×4).

2.3 Results and Discussions

The oxygen reduction reaction (ORR) was selected as a model system because its $n_{overall}$, which is determined by peroxide formation, varies between 2 and 4. The values are determined by configuration of oxygen adsorption depending on the nature of catalyst active sites: 4e for bidentate adsorption versus 2e for end-on (monodentate) configuration on platinum catalysts.[24-29]

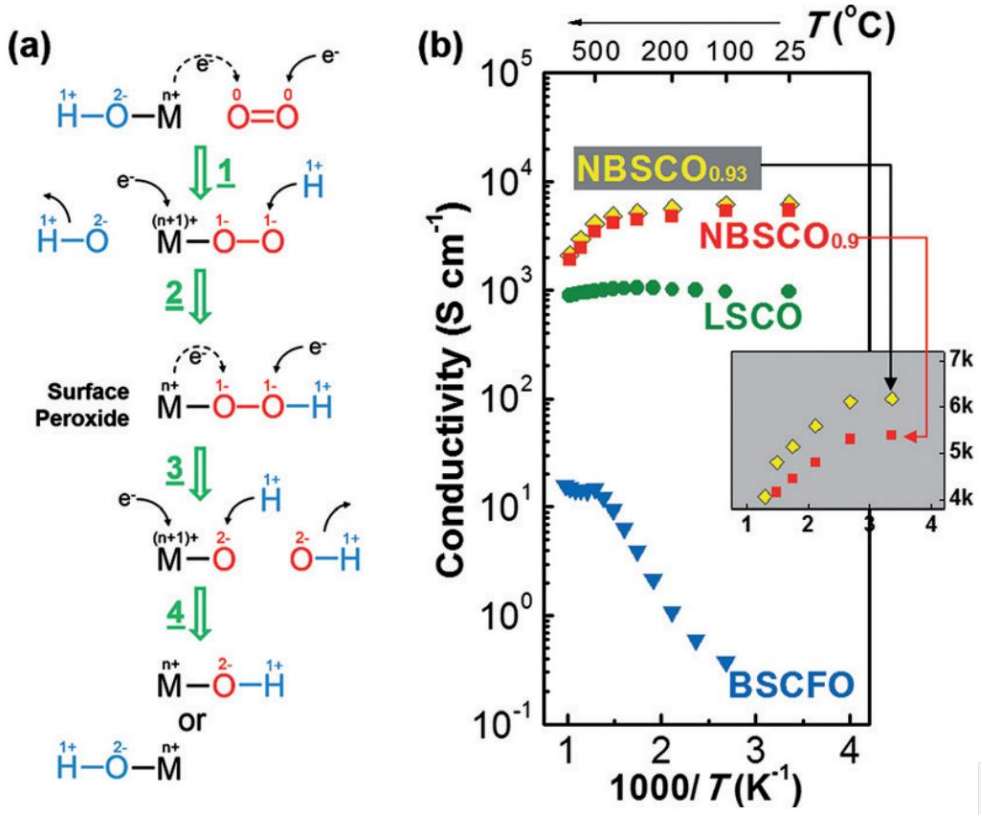

Figure 2.1 (a) Four one-electron elementary steps constituting ORR on metal active sites (M) of metal oxide catalysts. Solid and dashed arrows with e^- indicate the directions of external and internal electron transfer from potentiostats and the metal active site, respectively. Blue- and red-colored elements come from electrolyte (0.1m KOH) and dissolved oxygen, respectively. Oxidation numbers were indicated on top of the corresponding atoms. (b) Electrical conductivities (σ) of perovskite oxide catalysts in Arrhenius plots. Inset: Linear scale conductivity comparison between $NBSCO_{0.9}$ and $NBSCO_{0.93}$ for clarity.

ORR, especially by oxide catalysts, consists of four one-electron (1e) elementary steps in series with four surface species on active sites along a turnover track: $-OH^- \rightarrow -OO_2^- \rightarrow -OOH^- \rightarrow -O_2^- \rightarrow -OH^-$ (Fig. 2.1(a)).[24, 30, 31] Dioxygen molecules sit on metal atoms (M) of metal oxide catalysts in the monodentate configuration. The bond breakage of O–O of the surface peroxide (the 2e transfer

product formed after the second step in Fig. 2.1(a)) at step 3 is the step determining whether the overall reaction proceeds through a 2e or 4e electron transfer. A 4e transfer would be more encouraged if the peroxide intermediate were able to stay on the active sites (M) long enough to go forward to the next species before desorption, or if the rate of the steps after the peroxide formation (steps 3 and 4) were faster than that of the previous steps (steps 1 and 2).

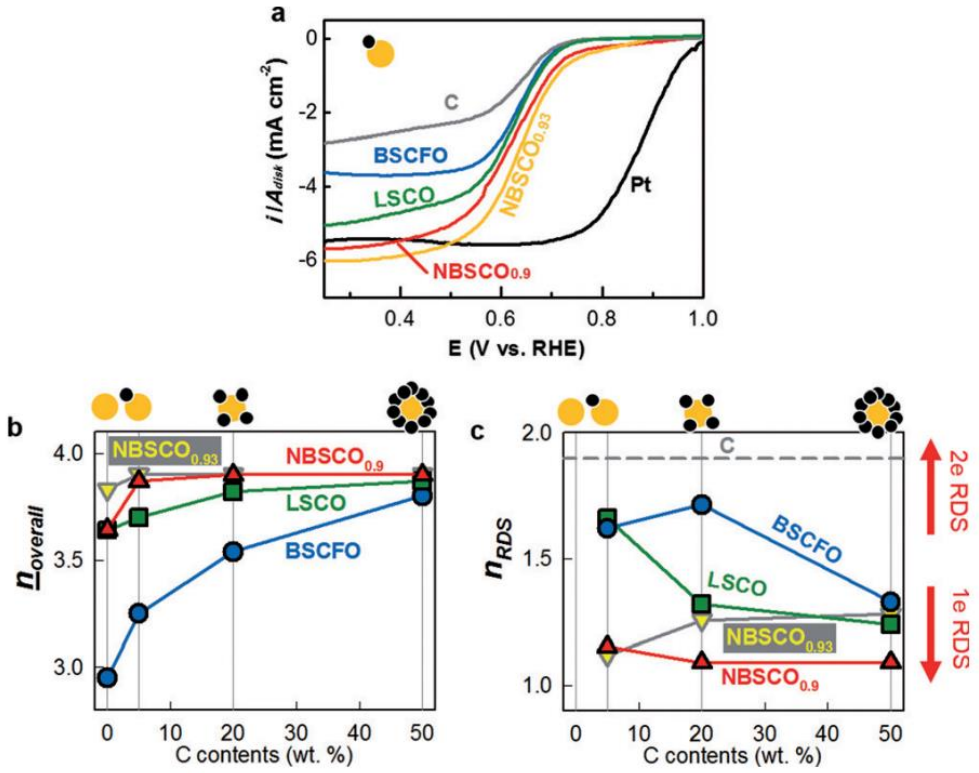

Figure 2.2 (a) Voltammograms of disk current of ORR in 0.1M KOH at cathodic scan (10 mV s^{-1}) on 1600 rpm. 5 wt.% carbon was used for BSCFO, LSCO, and NBSCO (Loading density, L=0.8 mg total cm^{-2} with total=oxide+carbon). 80 wt.% carbon was used with Pt (L=0.4 mg total cm^{-2}). (b) Number of electrons transferred for overall processes ($n_{overall}$). The values of $n_{overall}$ were calculated from currents on disk and ring electrodes along cathodic scan at the same rpm used in (a) during ORR. The average values ($n_{overall}$) were calculated by averaging $n_{overall}$ values at 0.33 V and 0.53 V. (c) Number of electrons transferred for the rate-determining step (n_{RDS}). n_{RDS} values were calculated from Tafel slopes (b) by using the relationship: b = 60 mV $dec^{-1}/(n_{RDS}\ \alpha)$, where the transfer coefficient (α) was assumed to be 0.5. A single catalyst particle (yellow circle) surrounded by multiple carbon black (black circles) represents carbon compositions on the top of (b) and (c).

Perovskite oxides, recently highlighted as catalysts for oxygen reduction and evolution, are potential materials for investigating the conductivity dependency of intrinsic parameters of ORR because of possible variation of their conductivities.[30-44] To investigate the conductivity dependency of $n_{overall}$ and

n_{RDS}, four different perovskite oxide catalysts with different electron conductivities were prepared: $Ba_{0.5}Sr_{0.5}Co_{0.8}Fe_{0.2}O_3$ (BSCFO) at less than 0.4 S cm^{-1} as its room-temperature electron conductivity (σ_{RM}); $La_{0.8}Sr_{0.2}CoO_{0.79}$ (LSCO) at 1000 S cm^{-1}; $NdBa_{0.25}Sr_{0.75}Co_2O_{5+\delta}$ with δ = 0.9 and 0.93 ($NBSCO_{0.9}$ and $NBSCO_{0.93}$) at 5400 and 6200 S cm^{-1}, respectively (Fig. 2.1(b)). BSCFO and LSCO are simple cubic perovskites (ABO_3; A = alkaline and/or rare earth metals, B = transition metals) while NBSCOs are double perovskites having alternative layers of different A site elements (Ba/Sr and Nd). Metallic conduction of the highly conductive NBSCO is explained by their narrow direct band gaps (E_{gap}) between valence bands (VB) extended above Fermi level (E_F) and conduction bands (CB).[45] On the contrary, the poorly conductive counterpart BSCFO showed indirect band gaps characteristic of semi-metals with wide direct band gaps.

The degree of ORR completion, indicated by $n_{overall}$, is an important parameter to describe the ORR as a series of reactions. The overall current relevant to ORR, which is measured on the disk compartment of rotating ring–disk electrodes (RRDEs), does not result only from the complete reduction of oxygen to hydroxide ions through a four-electron (4e; $n_{overall}$ = 4) transfer pathway ($O_2 + 2H_2O + 4e^- \rightarrow 4OH^-$).[46] A two-electron (2e; $n_{overall}$ = 2) transfer pathway ($O_2 + H_2O + 2e^- \rightarrow HO_2^- + OH^-$) is partly responsible for the ORR current, not completing a turnover of ORR but generating peroxide as an intermediate product. The intermediate HO_2^- was detected by ring electrodes oxidizing the peroxide to oxygen at + 0.4 V so that $n_{overall}$ was calculated by comparing between the currents of the disk and ring electrodes (Fig. 2.2(a)). Interestingly, the $n_{overall}$ values (or $n_{overall}$ as their average) were estimated to be higher on more conductive catalyst layers (Fig. 2.2(b)). We controlled the electric conduction through internal and external pathways by using catalysts of different conductivities and increasing carbon contents in electrodes. At a fixed carbon content (for example, 5 wt.%), 4e ORR processes were encouraged by more conductive internal electric pathways resulting from higher conductivities of catalysts: $n_{overall}$ was estimated at 3.9 for the most conductive NBSCO0.93 versus at 3.25 for the least conductive BSCFO. However, the difference of $n_{overall}$ between catalysts became smaller as the carbon contents increased (Fig. 2.2(b)). Higher carbon content resulted in increasing numbers of external electric pathways with shorter electron travelling length, with $n_{overall}$ approaching 4. With 50 wt.% carbon, therefore, there were no significant differences of $n_{overall}$ between catalysts.

The conductivity-dependent contribution of 4e or 2e processes to the overall currents on the perovskite oxide catalysts could be understood from the viewpoint of effective potential localized nearby active sites. The values of $n_{overall}$ (for instance, $n_{overall}$ is the average value of the $n_{overall}$ between 0.33 V and 0.53 V) depended on overpotential (η; Fig. 2.3(a)): higher η (or the more negative potential) resulted in larger $n_{overall}$. Even if the overpotential dependency trend was consistent over all samples, the critical overpotential (η_c) at which the $n_{overall}$ began to decrease dramatically shifted in the

direction to higher η (or more negative potential) from 0.65 V to 0.52 V with decreasing carbon contents in the most resistive BSCFO. However, more conductive catalysts (LSCO and NBSCO) showed no significant change in η_c with carbon contents except for 0 wt.% C. This indicates that more resistive situations caused by resistive catalysts and/or small carbon contents have reduced ohmic potential and require a higher overpotential to complete the 4e reaction.

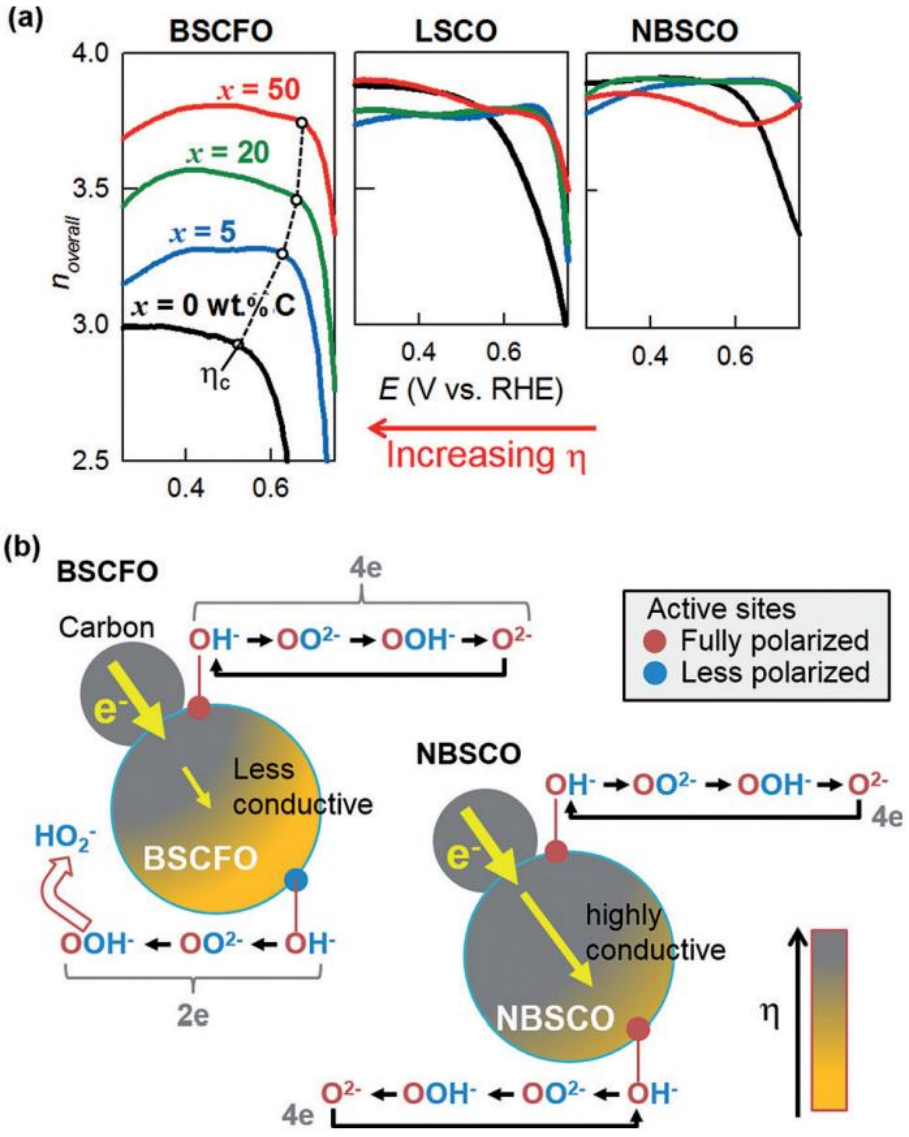

Figure 2.3 The effects of local potential distribution near the active sites on $n_{overall}$. (a) Potential dependency of $n_{overall}$. The critical overpotentials (η_c) at which the $n_{overall}$ dramatically decreases were indicated. (b) BSCFO and NBSCO as representative examples of less versus more conductive catalysts, respectively. Overpotential (η) gradients decrease with distance away from the contact point with carbon through the body of the catalyst.

Based on the overpotential dependency of $n_{overall}$, the catalytically active sites of low-conductivity perovskite catalysts (such as BSCFO) can be schematically categorized into fully and less polarized sites (Fig. 2.3(b)). Both sites benefit from the kinetic gain by the catalytic activation energy reduction. The fully polarized sites, experiencing high η and completing the 4e pathway, are physical points where the electric pathways provided by carbon meet the catalyst surface with the chemical species, including O_2. They are found near the contact points between carbon black and catalyst. The less polarized sites on the BSCFO surface, without contact to external electric pathways or far from the contact points between carbon and catalyst, experience small η for ORR in the catalyst side-space charge region near the electrolyte–catalyst interface owing to the resistive electron pathways throughout BSCFO. Therefore, peroxide ions are significantly produced from the less polarized sites before completing the overall 4e turnover, probably because the small h causes the rate of the steps after the peroxide formation (steps 3 and 4) to be kinetically slow (Fig. 2.1(a)). The surface peroxide is desorbed kinetically when its stay on an active site is longer than its possible retention time. This is supported by the observation that higher carbon contents of BSCFO-based electrodes increased $n_{overall}$ from 3.25 with 5 wt.% carbon to 3.8 with 50 wt.% carbon (Fig. 2.2(a)). On the other hand, all active sites of our highly conductive NBSCO have h values high enough to promote ORR efficiently along the 4e pathway with high $n_{overall}$ values, even at low carbon contents. Insignificant changes in $n_{overall}$ value with increasing carbon contents supports the idea that electrons are supplied to the surface efficiently through the NBSCO, even without external electron pathways (Fig. 2.2(a)).

As well as using $n_{overall}$ as a measure of ORR completion, n_{RDS} provides information on the electron transfer number, not for the overall ORR process but specifically for RDS.[47-50] The values of n_{RDS} are calculated from Tafel equation: $\eta = a + b \log i$ where $a = \ln i_o/(\alpha n_{RDS} f)$ and $b = -2.3/(\alpha n_{RDS} f)$ with $f = F/RT$. The ORR was assumed to be symmetric ($a = 0.5$) to obtain n_{RDS}.[51] Interestingly, n_{RDS} changed with electrode conductance, depending on catalyst conductivities as well as carbon content (Fig. 2.2(c)). The most conductive double perovskites ($NBSCO_{0.9}$ and $NBSCO_{0.93}$) showed small values of n_{RDS} values less than 1.5 for all of the carbon contents tested from 5 wt.% to 50 wt.%. In the medium-conductivity perovskite LSCO, on the other hand, its RDS at the lowest carbon content (5 wt.%) was identified more as 2e transfer, and the n_{RDS} changed from 2e to 1e around 20 wt.% carbon. In the least conductive BSCFO, the n_{RDS} transition was observed at higher carbon contents from 50 wt.%. That is to, the more conductive catalyst layers are, the closer to 1e process the RDS is.

Based on the results for $n_{overall}$ and n_{RDS}, therefore, 1e transfer RDS appears to be responsible for 4e ORR. This conclusion is in agreement with the ohmic polarization scenario, as discussed above. One or both of elementary steps of 1 and 4 (Fig. 2.1(a)), each from steps before and after peroxide formation, were known to be highly possible RDS.[30, 31] In low-conductivity catalysts with poorly conductive environments, both of them are thought to be RDSs because n_{RDS} was estimated at 2. The

latter RDS at step 4 would play a crucial role of peroxide generation by delaying forward conversion of surface peroxide to the next surface species. However, there is a single RDS (n_{RDS} = 1) with no RDS after the peroxide formation (that is to say, RDS at 1; and n_{RDS} = 1) in highly conductive catalysts and even in poorly conductive catalysts surrounded by highly conductive environments so that most of the oxygen is completely reduced through the 4e process.

2.4 Conclusion

In summary, we described the conductivity-dependency of the number of electrons transferred for ORR and its RDS. Whether electric conduction throughout electrodes is improved internally by using high-conductivity catalysts, or externally by adding conducting agents such as carbon black, completion of ORR by 4e transfer was promoted in more conductive situations by a one-step 1e RDS before surface peroxide formation. To our knowledge, this is the first observation showing that intensive and intrinsic properties of electrochemical reactions possibly depend on electric conduction that have been easily thought to affect extensive properties such as the effective amount of electroactive sites. Therefore, electric conductivities of electrocatalysts should be more seriously considered to obtain higher energy densities in electrocatalysis-based energy devices such as fuel cells and metal-air batteries.

References

1. L. Cao, F. Scheiba, C. Roth, F. Schweiger, C. Cremers, U. Stimming, H. Fuess, L. Q. Chen, W. T. Zhu, X. P. Qiu, Angew. Chem. Int. Ed. 2006, 45, 5315 – 5319; Angew. Chem. 2006, 118, 5441 – 5445.

2. A. Ermete, Appl. Catal. B 2009, 88, 1 – 24.

3. R. Kou, Y. Y. Shao, D. H. Wang, M. H. Engelhard, J. H. Kwak, J. Wang, V. V. Viswanathan, C. M. Wang, Y. H. Lin, Y. Wang, I. A. Aksay, J. Liu, Electrochem. Commun. 2009, 11, 954 – 957.

4. S. J. Guo, S. J. Dong, E. K. Wang, ACS Nano 2010, 4, 547 – 555.

5. Y. Y. Liang, Y. G. Li, H. L. Wang, J. G. Zhou, J. Wang, T. Regier, H. J. Dai, Nat. Mater. 2011, 10, 780 – 786.

6. C. V. Rao, A. L. M. Reddy, Y. Ishikawa, P. M. Ajayan, Carbon 2011, 49, 931 – 936.

7. Y. J. Li, Y. J. Li, E. B. Zhu, T. McLouth, C. Y. Chiu, X. Q. Huang, Y. Huang, J. Am. Chem. Soc. 2012, 134, 12326 –12329.

8. E. B. Bi, H. Chen, X. D. Yang, W. Q. Peng, M. Gratzel, L. Y. Han, Energy Environ. Sci. 2014, 7, 2637 – 2641.

9. S. Flandrois, B. Simon, Carbon 1999, 37, 165 – 180.

10. T. Mennola, M. Mikkola, M. Noponen, T. Hottinen, P. Lund, J. Power Sources 2002, 112, 261 – 272.

11. W. M. Zhang, X. L. Wu, J. S. Hu, Y. G. Guo, L. J. Wan, Adv. Funct. Mater. 2008, 18, 3941 –3946.

12. L. F. Cui, Y. Yang, C. M. Hsu, Y. Cui, Nano Lett. 2009, 9, 3370 – 3374.

13. M. Breysse, J. Veron, B. Claudel, H. Latreill, M. Guenin, J. Catal. 1972, 27, 275 – 280.

14. K. A. Stoerzinger, W. Lî, C. Li, Ariando, T. Venkatesan, Y. Shao-Horn, J. Phys. Chem. Lett. 2015, 6, 1435 – 1440.

15. E. Passalacqua, F. Lufrano, G. Squadrito, A. Patti, L. Giorgi, Electrochim. Acta 2001, 46, 799 – 805.

16. D. van der Vliet, D. S. Strmcnik, C. Wang, V. R. Stamenkovic, N. M. Markovic, M. T. M. Koper, J. Electroanal. Chem. 2010, 647, 29 – 34.

17. E. Fabbri, R. Mohamed, P. Levecque, O. Conrad, R. Kçtz, T. J. Schmidt, ACS Catal. 2014, 4, 1061 – 1070.

18. M. D. Segall, J. D. L. Philip, M. J. Probert, C. J. Pickard, P. J. Hasnip, S. J. Clark, M. C. Payne, J. Phys.: Condens. Matter 2002, 14, 2717.

19. J. P. Perdew, K. Burke, M. Ernzerhof, Phys. Rev. Lett. 1996, 77, 3865-3868.

20. J. P. Perdew, A. Zunger, Phys. Rev. B 1981, 23, 5048-5079.

21. A. Seidl, A. Görling, P. Vogl, J. A. Majewski, M. Levy, Phys. Rev. B 1996, 53, 3764-3774.

22. C. G. Broyden, J. Inst. Math. Appl. 1970, 6, 76-90.

23. H. J. Monkhorst, J. D. Pack, Phys. Rev. B 1976, 13, 5188-5192.

24. J. B. Goodenough, B. L. Cushing in Handbook of Fuel Cells (Eds.: W. Vielstich, H. A. Gasteiger, H. Yokokawa), Wiley, Hoboken, 2010.

25. N. M. Marković, T. J. Schmidt, V. Stamenkovic, P. N. Ross, Fuel Cells 2001, 1, 105 – 116.

26. N. M. Marković, P. N. Ross, Surf. Sci. Rep. 2002, 45, 121 – 229.

27. N. M. Marković, H. A. Gasteiger, N. Philip, J. Phys. Chem. 1996, 100, 6715 – 6721.

28. V. Komanicky, H. Iddir, K. C. Chang, A. Menzel, G. Karapetrov, D. Hennessy, P. Zapol, H. You, J. Am. Chem. Soc. 2009, 131, 5732 – 5733.

29. M. S. El-Deab, T. Ohsaka, Angew. Chem. Int. Ed. 2006, 45, 5963 – 5966; Angew. Chem. 2006, 118, 6109 – 6112.

30. J. Suntivich, K. J. May, H. A. Gasteiger, J. B. Goodenough, Y. Shao-Horn, Science 2011, 334, 1383 – 1385.

31. J. Suntivich, H. A. Gasteiger, N. Yabuuchi, H. Nakanishi, J. B. Goodenough, Y. Shao-Horn, Nat. Chem. 2011, 3, 546 – 550.

32. M. Risch, K. A. Stoerzinger, S. Maruyama, W. T. Hong, I. Takeuchi, Y. Shao-Horn, J. Am. Chem. Soc. 2014, 136, 5229 – 5232.

33. T. Takeguchi, T. Yamanaka, H. Takahashi, H. Watanabe, T. Kuroki, H. Nakanishi, Y. Orikasa, Y. Uchimoto, H. Takano, N. Ohguri, M. Matsuda, T. Murota, K. Uosaki, W. Ueda, J. Am. Chem. Soc. 2013, 135, 11125 – 11130.

34. J.-J. Xu, D. Xu, Z.-L. Wang, H.-G. Wang, L.-L. Zhang, X.-B. Zhang, Angew. Chem. Int. Ed. 2013, 52, 3887 – 3890; Angew. Chem. 2013, 125, 3979 – 3982.

35. Y. L. Zhao, L. Xu, L. Q. Mai, C. H. Han, Q. Y. An, X. Xu, X. Liu, Q. J. Zhang, Proc. Natl. Acad. Sci. USA 2012, 109, 19569 – 19574.

36. J.-I. Jung, H. Y. Jeong, J.-S. Lee, M. G. Kim, J. Cho, Angew. Chem. Int. Ed. 2014, 53, 4582 – 4586; Angew. Chem. 2014, 126, 4670 – 4674.

37. A. Grimaud, K. J. May, C. E. Carlton, Y.-L. Lee, M. Risch, W. T. Hong, J. Zhou, Y. Shao-Horn, Nat. Commun. 2013, 4, 2439.

38. J. Kim, X. Yin, K. C. Tsao, S. H. Fang, H. Yang, J. Am. Chem. Soc. 2014, 136, 14646 – 14649.

39. Y. L. Zhu, W. Zhou, Z. G. Chen, Y. B. Chen, C. Su, M. O. Tade, Z. P. Shao, Angew. Chem. 2015, 127, 3969 – 3973.

40. W. Zhou, J. Sunarso, J. Phys. Chem. Lett. 2013, 4, 2982 – 2988.

41. Y. Zhu, C. Su, X. Xu, W. Zhou, R. Ran, Z. Shao, Chem. Eur. J. 2014, 20, 15533 – 15542.

42. R. Liu, F. Liang, W. Zhou, Y. Yang, Z. Zhu, Nano Energy 2015, 12, 115 – 122.

43. Y. Zhu, W. Zhou, Y. Chen, J. Yu, X. Xu, C. Su, M. O. Tad¦, Z. Shao, Chem. Mater. 2015, 27, 3048 – 3054.

44. W. Zhou, M. Zhao, F. Liang, S. C. Smith, Z. Zhu, Mater. Horiz. 2015, 2, 495 – 501.

45. X. Blase, E. Bustarret, C. Chapelier, T. Klein, C. Marcenat, Nat. Mater. 2009, 8, 375 – 382.

46. S. M. Park, S. Ho, S. Aruliah, M. F. Weber, C. A. Ward, R. D. Venter, S. Srinivasan, J. Electrochem. Soc. 1986, 133, 1641 – 1649.

47. A. Parthasarathy, S. Srinivasan, A. J. Appleby, C. R. Martin, J. Electrochem. Soc. 1992, 139, 2856 – 2862.

48. U. A. Paulus, T. J. Schmidt, H. A. Gasteiger, R. J. Behm, J. Electroanal. Chem. 2001, 495, 134 – 145.

49. L. Zhang, K. Lee, J. J. Zhang, Electrochim. Acta 2007, 52, 3088 – 3094.

50. V. M. Voinovic, B. D. Sepa, Electrochim. Acta 1981, 26, 781 – 793.

51. C. Song, J. Zhang in PEM Fuel Cell Electrocatalysts and Catalyst Layers (Ed.: J. Zhang), Springer, London, 2008, pp. 89 – 134.

Chapter III. Major role of surface area in perovskite electrocatalysts for alkaline systems

ChemElectroChem: Chahwan Hwang,[†] Ohhun Gwon,[†] Hongil Jo, Kang Min Ok,[*] and Guntae Kim[*]: Major Role of Surface Area in Perovskite Electrocatalysts for Alkaline Systems. ChemElectroChem. 2017. 4. 468-471. Copyright Wiley-VCH Verlag GmbH & Co. KGaA. Reproduced with permission.

3.1 Introduction

Development of highly efficient, eco-friendly, and low-cost energy systems, such as water splitting, electrolysis cells, fuel cells, and metal−air batteries, is an important ongoing research topic for energy conversion and storage industry. To realize efficient energy conversion and storage applications, it is necessary to improve the catalytic activity for ORR and OER.[1-11]

In general, precious metals and related oxides such as Pt, IrO_2, and RuO_2 have been used as catalysts based on their high catalytic activities. However, the usage of precious catalysts for commercial application is very limited due to their high cost and limited reserves.[12, 13] Recently, the development of inexpensive and superior performing electro-catalysts based on transition-metal oxide materials such as cobalt containing oxides has received enormous attention.[5, 14-20] Oxides containing cobalt cations, particularly perovskite-type structures, have shown synergistic catalytic activities with high efficiency for both ORR and OER.[21-23] In general, the formula for oxide perovskites can be written as $A_{1-x}A'_xB_{1-y}B'_yO_{3\pm\delta}$. Larger 12-coordinate A cations and smaller 6-coordinate B cations can be relatively easily substituted by various metal cations, which often results in an oxygen non-stoichiometry such as oxygen excess or deficiency.[24, 25] The structural variations arising from the defects enable catalytic reactions including both oxidation and reduction.[26, 27] In particular, lanthanide-based perovskites have shown remarkable performance as high temperature catalysts in solid oxide fuel cell devices and as gas-solid phase heterogeneous catalysts (CO oxidation or methane oxidation).[28-30] The partial substitution of the A-site cations with different valence elements such as alkaline-earth metal cations in the lanthanide-based perovskites may induce oxygen non-stoichiometry or bond distortions, which can increase the oxygen mobility or electrical conductivity. The structural defects and/or variations of electronic structure influence the catalytic activity in the electrochemical devices.[31, 32] Gradual substitution of divalent Sr^{2+} cation for Ln^{3+} in the A-site not only facilitates the electronic structure transition of Ln-based perovskite from semiconductor to metal but also varies the catalytic activity.[33-36] In fact, a substitution of a specific amount of Ln^{3+} for Sr^{2+} ($0.3 < x < 0.7$) resulted in the highest electrical conductivity among the $Ln_xSr_{1-x}BO_{3-\delta}$ series.[37, 38] According to the recent report, higher electrical conductivity of the metallic perovskite plays a key role in the electrocatalytic effect.[39] On the other hand, the catalytic activity of heterogeneous catalysts such as solid-liquid phase or solid-gas phase catalysts mainly depends on the properties of the constituent

transition metals and the number of active sites on the catalysts. For instance, in a non-aqueous Li-air battery, larger specific surface area of the cathode catalyst is crucial to increase the electric current density in the OER process.[40-42] A large degree of initial adsorption compensates the slow conversion rate for hydroxyl species to oxygen on the metal site.[43] Therefore, the surface area along with various particle sizes must be considered when evaluating and comparing the catalytic activity of heterogeneous catalysts. At the same time, the heterogeneous catalysts should have porosity and smaller particle size to attain high surface area for reasonable performance. Although it is known that the significant catalytic features strongly depend on the surface area, the synthesis of well-defined nano-structured Ln-based perovskites has through conventional solid state reactions proven extremely difficult, and this is attributable to the high crystallization temperatures.

Herein, we report a facile synthesis of well-defined $Ln_{0.5}Sr_{0.5}CoO_{3-\delta}$ (Ln = Pr, Nd, Sm, Gd; LnSC) nanoparticles with high surface area using a fast and cost-effective simple batch type co-precipitation method. We also present the electrochemical catalytic activities of the materials by varying the corresponding Ln cations and surface areas.

3.2 Experimental

3.2.1 Material Preparation

$Ln_xSr_{1-x}CoO_{3-\delta}$ (Ln = Pr, Nd, Sm, and Gd) nano-crystallites were prepared through a co-precipitation method. A stoichiometric amount of $Ln(CH_3CO_2)_3 \cdot xH_2O$, $Sr(CH_3CO_2)_2$, $Co(CH_3CO_2)_2 \cdot 4H_2O$ (Ln : Sr : Co = 3 : 3 : 6 of mmol) were completely dissolved in 40 mL of distilled water. After that, 160 mL of ethanol was added to the solution. To precipitate the metal cations, 30 mL of $(NH_4)_2CO_3$ aqueous solution (10 wt.%) was slowly added by a syringe pump to the solution with stirring at 700 rpm. The flow rate of the syringe pump was kept at 0.5 mL min-1. After injection, the reaction mixture was stirred further for 30 min. The precipitates were collected by centrifugation at 5000 rpm for 3 min. The precipitates were washed thoroughly with deionized water and acetone to remove the residual ammonium acetate by-product. The reaction products were dried under vacuum overnight. The dried products were calcined at varied temperatures for 6 h. Finally, the calcined compounds were finely ground with mortars and pestles.

3.2.2 Structural Analysis

Powder X-ray diffraction patterns were obtained on a Bruker D8-Advance diffractometer (Cu Kα radiation) with 40 kV and 40 mA. The samples were scanned in the 2θ range of 20 to 50 o with a step size of 0.02 o and a step time of 0.4 s. Particle images and chemical composition were collected using a field emission scanning electron microscope (FE-SEM, SIGMA/Carl Zeiss) equipped with an energy dispersive spectrometer (EDS, Thermo NORAN System 7) and a field emission transmission electron microscope (FE-TEM, FEI Tecnai G2 F30, 200 kV). The Brunauer-Emmett-Teller (BET) measurements were carried out using a Quantachrome NOVA 1200e surface area analyzer using N_2 at 77 K. The oxidation states of the cobalt and oxygen in the samples were measured by X-ray photoelectron spectroscopy (Thermo Fisher Scientific, ESCALAB 250XI).

3.2.3 Electrochemical Analysis

LnSC inks were prepared by dispersing a 20 mg of nanoparticles in 0.45 mL of ethanol, 0.45 mL of isopropyl alcohol, and 0.1 mL of 5 wt.% nafion solution without any conducting materials. Loading density of the composite of nanoparticles and conducting agent was fixed at 0.8 mg cm^{-2}. Cyclic and linear sweep voltammetries (CVs and LSVs) were measured on disk and ring electrodes simultaneously by a computer-controlled potentiostat (Biologic VMP3) with 1600 rpm controlled by a rotating disk electrode system (Biologic RRDE-3A). A platinum wire and an Hg/HgO electrode were used as the counter and reference electrodes, respectively. An aqueous solution of 0.1M KOH was used as the electrolyte. ORR polarization curves were obtained on the disk electrode from a cathodic sweep from 0.1 V to -0.9 V (vs. Hg/HgO) at 10 mV s^{-1} after several cycles of CVs. 0.4 V was applied

to the ring electrode to estimate the amount of peroxide generated from the disk electrode. The anodic sweeps from 0.35V to 0.9V (vs. Hg/HgO) were presented as OER polarization curves. The other conditions were the same as those for the ORR polarization curves.

3.3 Results and Discussions

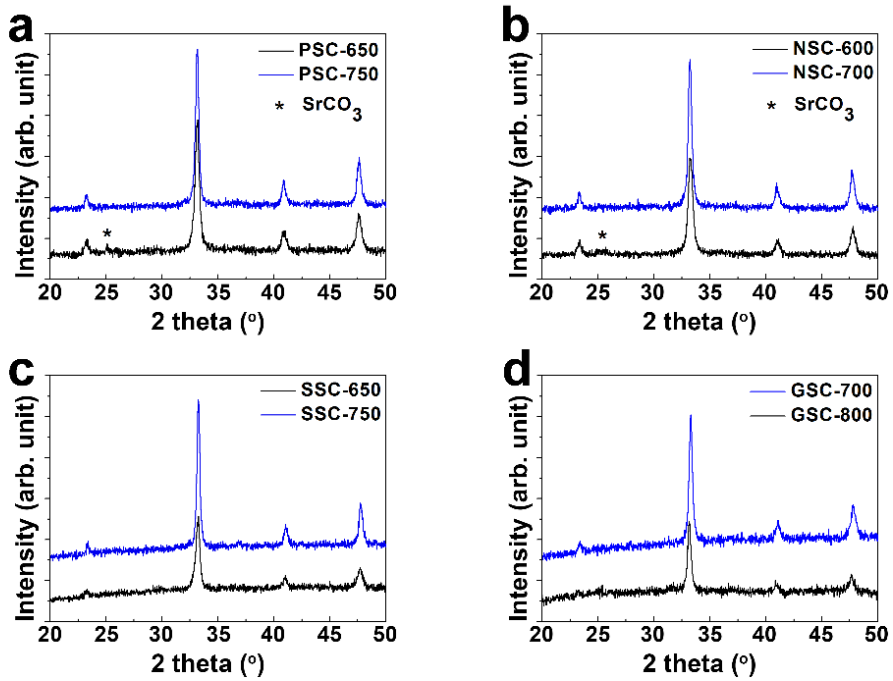

Figure 3.1 Powder X-ray diffraction patterns of the cubic perovskite nano-crystallites prepared at different temperatures. (a) PSC calcined at 650 and 750 °C, (b) NSC calcined at 600 and 700 °C, (c) SSC calcined at 650 and 750 °C, and (d) GSC calcined at 700 and 800 °C. While the patterns in black are taken from the nanoparticles obtained at their minimum crystallization temperatures for each lanthanide ion, those in blue are taken from nano-crystallites calcined at 100 °C higher temperatures.

Figure 3.1 shows the XRD patterns of LnSC samples prepared at different calcination temperatures ranging from 600 to 800 °C. The XRD patterns indicate that phase pure LnSC nano-crystallites with simple cubic perovskite structures were successfully synthesized.

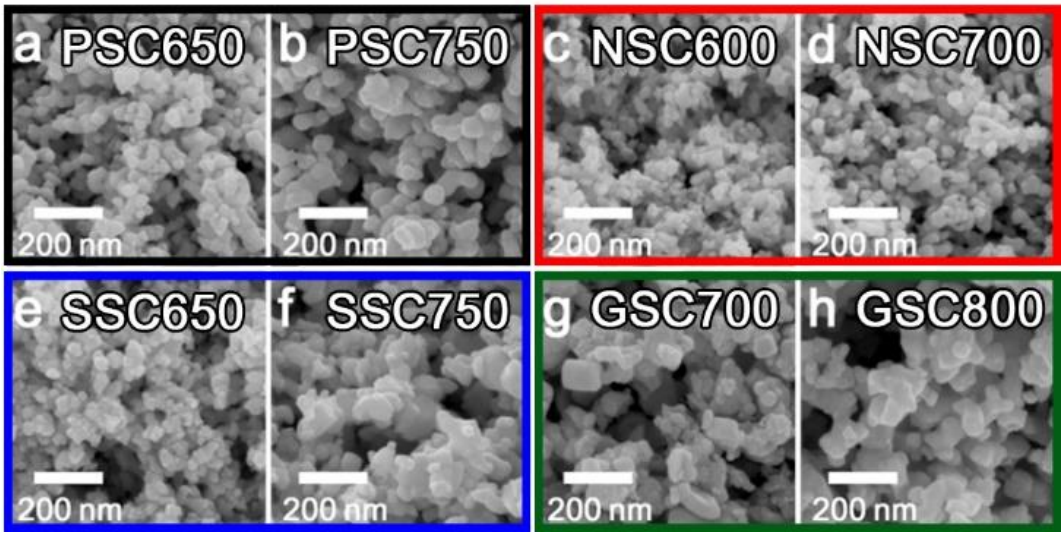

Figure 3.2 FE-SEM images of the (a) PSC-650, (b) PSC-750, (c) NSC-600, (d) NSC-700, (e) SSC-650, (f) SSC-750, (g) GSC-700, and (h) GSC-800. Note the size of each nano-crystallite increases as the calcination temperatures increases.

Table 3.1 Summary of average particle sizes, calculated crystallite sizes, surface areas, and oxidation states of synthesized LnSCs nano-crystallites.

	Calcination Temp. (^oC)	Avg. Particle size (nm)	Crystallite size (nm)	Surface area ($m^2\ g^{-1}$)	Ox. State	
					Co^{3+}	Co^{4+}
PSC	650	32.6	23.9	33.12	47.80	52.20
	750	50.9	31.8	25.78		
NSC	600	22.6	21.0	30.21	48.70	51.30
	700	32.9	31.1	25.90		
SSC	650	33.1	25.7	30.86	47.60	52.40
	750	52.1	34.3	16.79		
GSC	700	65.4	29.4	23.31	48.10	51.90
	800	84.6	36.3	11.69		

The FE-SEM images clearly reveal that the synthesized LnSCs materials are well-defined nano-sized crystallites (Fig. 3.2). As seen in Fig. 3.2, the sizes of the nano-crystallites increase as the calcination temperatures increase. Interestingly, while the nano-crystallites of PSC and NSC prepared at lower temperatures reveal a narrow size distribution ranging from 20 to 40 nm, those of SSC and GSC exhibit a somewhat broad size distribution of 25-80 nm. The average crystallite sizes obtained by both a FE-SEM image analysis and the Scherrer equation are tabulated in Table 3.1 along with the surface areas for all the LnSCs. As can be seen in Table 3.1, the specific surface areas of all the materials prepared at lower calcination temperatures are larger than those obtained from higher calcination temperatures, which is consistent with the difference in particle sizes. GSC-700 and NSC-700 reveal very similar small crystallite sizes of 29.4 and 31.1 nm, respectively. Interestingly, however, the

average particle size of GSC-700 (65.4 nm) is much larger than that of NSC-700 (32.9 nm). The observed difference in average particle sizes for the crystallites may be caused by the different sintering effect for the highly aggregated primary particles.

As seen in Table 3.1, the BET surface areas for the nanoparticles prepared at lower calcination temperatures are larger than those of the nanoparticles calcined at higher temperatures. As we will discuss in greater detail later, the smaller LnSC nano-crystallites with larger surface areas exhibit better electrochemical catalytic performance because the large surface area can provide many catalytic active sites in the electrochemical reactions.

Table 3.2 Atomic percentages and atomic ratio of calcined LnSCs.

	Atom %			Atomic ratio		
	Ln (Pr, Nd, Sm, Gd)	Sr	Co	Ln (Pr, Nd, Sm, Gd)	Sr	Co
PSC	21.32	22.11	56.57	1	1.0	2.7
NSC	24.54	24.00	51.46	1	1.0	2.1
SSC	23.95	26.53	49.52	1	1.1	2.1
GSC	25.32	26.83	47.85	1	1.1	1.9

The atomic composition of synthesized LnSC nano-crystallites was determined by EDS data (Table 3.2), where the lanthanide elements were normalized to confirm the stoichiometry. EDS for PSC, NSC, SSC, and GSC reveal approximate Ln:Sr:Co ratios of 1:1:2, respectively. The stoichiometric $Ln_{0.5}Sr_{0.5}CoO_{3-\delta}$ is known as a high electrical conductor, and therefore the synthesized LnSC nanoparticles are expected to be electrochemical catalysts without conducting materials such as carbon black or carbon nanotubes.

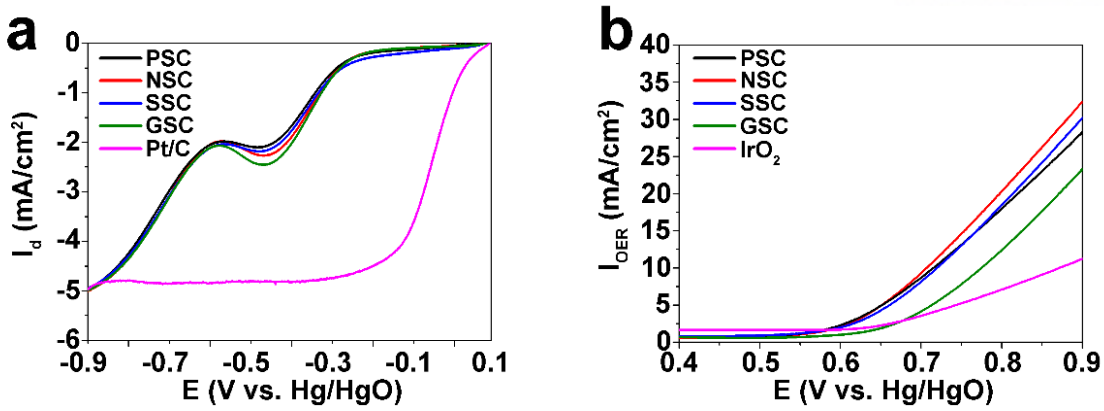

Figure 3.3 Disc current of (a) ORR and (b) OER measured by LSV with 10 mV s^{-1} scan rate at 1600 rpm.

Rotating ring-disk electrode (RRDE) measurement with 1 mg cm^{-2} of LnSCs is used to verify the catalytic pathways and to reveal the kinetics of lanthanides for the ORR and OER catalytic activities in 0.1 M KOH (Fig. 3.3). Interestingly, the catalytic activities of the measured samples that have similar surface area (~30 m^2 g^{-1}) were independent of the various lanthanides in the A-site. The ORR onset potentials of all prepared LnSCs at -0.15 mA cm^{-2} (Fig. 3.3(a)) were -0.2 V (vs Hg/HgO) and their limiting currents in the ORR condition were -5.0 mA cm^{-2} at -0.9 V (vs Hg/HgO).

The potential is stretched to 0.9 V (vs Hg/HgO) in a water oxidation system and the electrocatalytic oxygen evolution reaction (OER) is evaluated. The LnSC catalysts afforded current density of 10 mA cm^{-2} at a small overpotential of ~0.72 V and the OER onset potentials were 0.6 V (vs Hg/HgO) at 2.0 mA cm^{-2} (Fig. 3.3(b)).

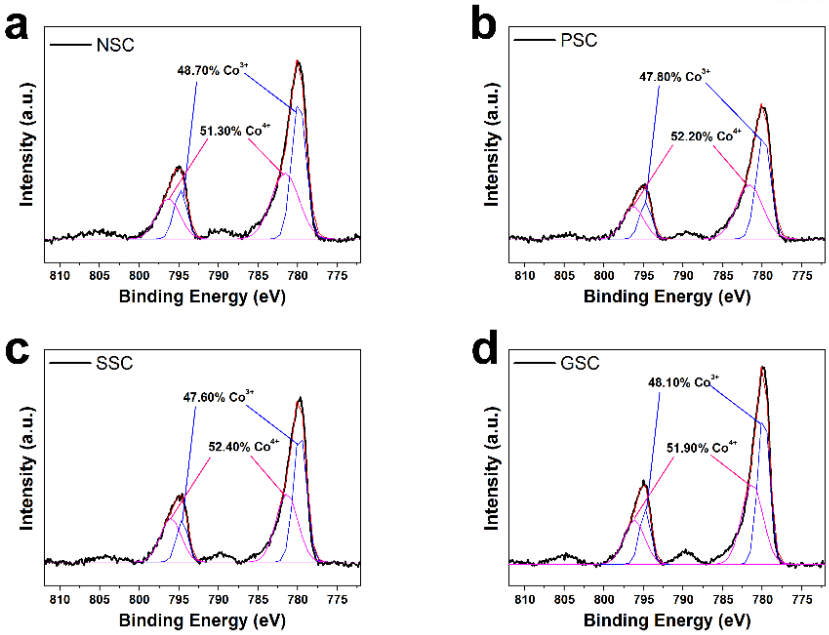

Figure 3.4 Cobalt 2P XPS spectra of (a) NSC, (b) PSC, (c) SSC, and (d) GSC.

Oxidation state of the transition metal is an important factor to explain the catalytic activities for ORR and OER. Therefore, the oxidation states of the cobalt also can serve as evidence to explain the effect of A-site lanthanides for ORR and OER in the LnSC catalysts. X-ray photoelectron spectroscopy (XPS) measurement is carried out to characterize the states of cobalt in LnSC catalysts, and the results are shown in Fig. 3.4 and Table 3.1.

The XPS results of the LnSCs show that the main peaks are located at binding energy of about 780.1 eV (at Co $2p_{3/2}$) and 796.6 eV (at Co $2p_{1/2}$) for the Co 2p spectra. The spectrum consists of Co^{3+} (blue line) and Co^{4+} (pink line), which can be distinguished by Gaussian fitting. According to the fitting results, all the samples have similar cobalt ion ratios. Consequently, as long as a similar surface area and Co oxidation state are maintained, A-site changes in the perovskite do not play catalytic roles in the alkaline media system.

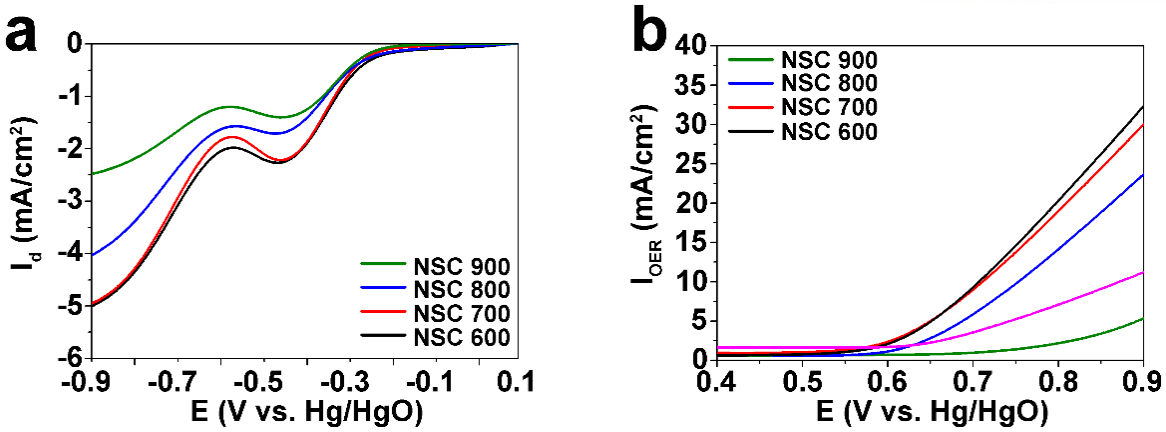

Figure 3.5 (a) Disc current of ORR and (b) disc current of oxygen evolution reaction of NSC 600, 700, 800, and 900, measured by RRDE with 10 mV s^{-1} scan rate at 1600 rpm.

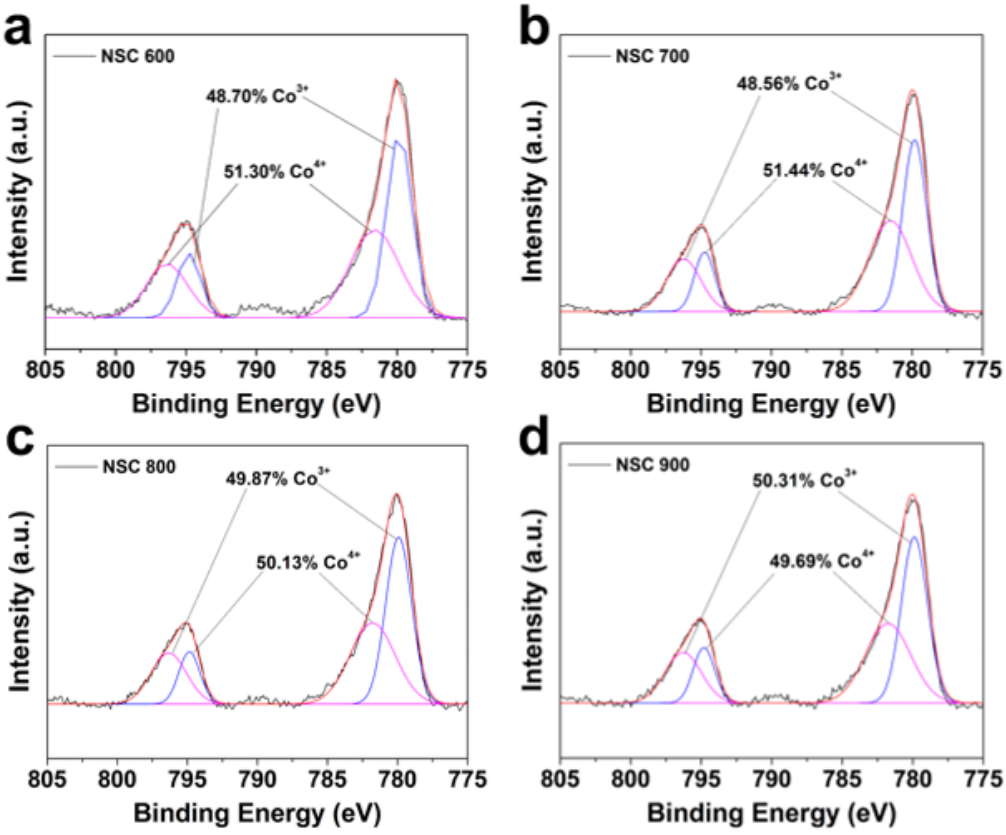

Figure 3.6 Cobalt 2P XPS spectra of (a) NSC 600, (b) NSC 700, (c) NSC 800, and (d) NSC 900.

In order to assess the surface area effect on catalytic activities, we controlled the surface area via calcination temperature variation for only the NSC catalyst. The results show that the surface area only affects the current densities, causing drastic changes (Fig. 3.5). The limiting currents of NSCs were increased from -2.5 to -5.0 mA cm^{-2} with the increase of surface area at -0.9 V (vs Hg/HgO). The

OER onset potentials meanwhile showed a similar trend with values of 0.58, 0.59, 0.63, and 0.79 V (vs Hg/HgO) at 2.0 mA cm^{-2} for the NSC 600, 700, 800, and 900. Also, the current densities of OER at -0.9 V (vs Hg/HgO) rapidly decreased with decreasing surface area. Additionally, as mentioned above, since the state of Co in NSCs prepared at various calcination temperatures could affect catalytic activities, XPS measurement was performed and the results indicate that variation of the surface area controlled by the calcination temperature does not affect the state of Co in NSCs, as shown in Fig. 3.6. Therefore, it is confirmed that the improvement of ORR and OER stems from higher surface area only.

3.4 Conclusion

In summary, the series of lanthanide-based perovskite nanoparticles were successfully synthesized using simple co-precipitation methods. All the nano-crystallites were prepared at relatively lower calcination temperatures and exhibited similar particle sizes with high surface areas. RRDE, XPS, and surface control results in this study revealed that the electrocatalytic properties (ORR and OER) of the perovskite oxide are not significantly affected by the different kinds of lanthanides in the A-site in alkaline condition. However, the surface area and particle size are factors that limit the current density. Therefore, it is important to compare the results for ORR and OER with other data in the literature, including microstructural properties such as surface area and particle size.

References

1. A. J. Bard, M. A. Fox, Acc. Chem. Res. 1995, 28, 141–145.

2. M. Winter, R. J. Brodd, Chem. Rev. 2005, 105, 1021–1021.

3. N. S. Lewis, D. G. Nocera, Proc. Natl. Acad. Sci. 2006, 103, 15729–15735.

4. A. a. Gewirth, M. S. Thorum, Inorg. Chem. 2010, 49, 3557–3566.

5. Y. Liang, Y. Li, H. Wang, J. Zhou, J. Wang, T. Regier, H. Dai, Nat. Mater. 2011, 10, 780–786.

6. J. Wang, H. Zhong, Y. Qin, X. Zhang, Angew. Chemie Int. Ed. 2013, 125, 5356–5361.

7. H. Zhong, J. Wang, Y. Zhang, W. Xu, W. Xing, D. Xu, Y. Zhang, X. Zhang, Angew. Chemie Int. Ed. 2014, 53, 14235–14239.

8. J. Wang, K. Li, H. Zhong, D. Xu, Z. Wang, Z. Jiang, Z. Wu, X. Zhang, Angew. Chemie Int. Ed. 2015, 54, 10530–10534.

9. H. Zhong, J. Wang, F. Meng, X. Zhang, Angew. Chemie Int. Ed. 2016, 55, 9937–9941.

10. J. Wang, H. Zhong, Z. Wang, F. Meng, X. Zhang, ACS Nano 2016, 10, 2342–2348.

11. O. Gwon, C. Kim, O. Kwon, H. Y. Jeong, H.-K. Park, J. Shin, Y.-W. Ju, G. Kim, J. Electrochem. Soc. 2016, 163, A1893–A1897.

12. B. Wang, J. Power Sources 2005, 152, 1–15.

13. J.-H. Kim, A. Ishihara, S. Mitsushima, N. Kamiya, K.-I. Ota, Electrochim. Acta 2007, 52, 2492–2497.

14. Y. Gorlin, T. F. Jaramillo, J. Am. Chem. Soc. 2010, 132, 13612–13614.

15. Y. Gorlin, D. Nordlund, T. F. Jaramillo, ECS Trans. 2013, 58, 735–750.

16. Q. Liu, J. Jin, J. Zhang, ACS Appl. Mater. Interfaces 2013, 5, 5002–5008.

17. X. Cao, C. Jin, F. Lu, Z. Yang, M. Shen, R. Yang, J. Electrochem. Soc. 2014, 161, H296–H300.

18. Y. Meng, W. Song, H. Huang, Z. Ren, S. Chen, S. L. Suib, J. Am. Chem. Soc. 2014, 136, 11452–11464.

19. S. Yoo, A. Jun, Y. Ju, D. Odkhuu, J. Hyodo, H. Y. Jeong, N. Park, J. Shin, T. Ishihara, G. Kim, Angew. Chemie Int. Ed. 2014, 13064–13067.

20. S. Sengodan, S. Choi, A. Jun, T. H. Shin, Y.-W. Ju, H. Y. Jeong, J. Shin, J. T. S. Irvine, G. Kim, Nat. Mater. 2014, 14, 205–209.

21. J. Suntivich, H. a Gasteiger, N. Yabuuchi, H. Nakanishi, J. B. Goodenough, Y. Shao-Horn, Nat. Chem. 2011, 3, 546–550.

22. K. J. May, C. E. Carlton, K. a. Stoerzinger, M. Risch, J. Suntivich, Y.-L. Lee, A. Grimaud, Y. Shao-Horn, J. Phys. Chem. Lett. 2012, 3, 3264–3270.

23. A. Grimaud, C. E. Carlton, M. Risch, W. T. Hong, K. J. May, Y. Shao-Horn, J. Phys. Chem. C 2013, 117, 25926–25932.

24. T. NITADORI, J. Catal. 1986, 98, 221–228.

25. J. T. Mefford, W. G. Hardin, S. Dai, K. P. Johnston, K. J. Stevenson, Nat. Mater. 2014, 13, 726–732.

26. K. T. Lee, A. Manthiram, J. Electrochem. Soc. 2006, 153, A794-A798.

27. J. Suntivich, H. a Gasteiger, N. Yabuuchi, H. Nakanishi, J. B. Goodenough, Y. Shao-Horn, Nat. Chem. 2011, 3, 546–550.

28. S. Gupta, W. Kellogg, H. Xu, X. Liu, J. Cho, G. Wu, Chem. An Asian J. 2016, 11, 10–21.

29. M. M. Natile, E. Ugel, C. Maccato, A. Glisenti, Appl. Catal. B Environ. 2007, 72, 351–362.

30. P. H. T. Ngamou, N. Bahlawane, Chem. Mater. 2010, 22, 4158–4165.

31. A. Vojvodic, J. K. Norskov, Science. 2011, 334, 1355–1356.

32. D. N. Mueller, M. L. Machala, H. Bluhm, W. C. Chueh, Nat. Commun. 2015, 6, 6097.

33. J. Tulloch, S. W. Donne, J. Power Sources 2009, 188, 359–366.

34. E. J. Crumlin, S.-J. Ahn, D. Lee, E. Mutoro, M. D. Biegalski, H. M. Christen, Y. Shao-Horn, J. Electrochem. Soc. 2012, 159, F219–F225.

35. S. Park, S. Choi, J. Shin, G. Kim, J. Power Sources 2012, 210, 172–177.

36. O. Gwon, S. Yoo, J. Shin, G. Kim, Int. J. Hydrogen Energy 2014, 39, 20806–20811.

37. A. Mineshige, M. Inaba, T. Yao, Z. Ogumi, J. Solid State Chem. 1996, 121, 423–429.

38. K. T. Lee, A. Manthiram, J. Electrochem. Soc. 2005, 152, A197.

39. D.-G. Lee, O. Gwon, H.-S. Park, S. H. Kim, J. Yang, S. K. Kwak, G. Kim, H.-K. Song, Angew. Chemie Int. Ed. 2015, 54, 15730–15733.

40. Y. Wang, J. Ren, Y. Wang, F. Zhang, X. Liu, Y. Guo, G. Lu, J. Phys. Chem. C 2008, 112, 15293–15298.

41. Y. Zhao, L. Xu, L. Mai, C. Han, Q. An, X. Xu, X. Liu, Q. Zhang, Proc. Natl. Acad. Sci. U. S. A. 2012, 109, 19569–19574.

42. J. J. Xu, D. Xu, Z. L. Wang, H. G. Wang, L. L. Zhang, X. B. Zhang, Angew. Chemie Int. Ed. 2013, 52, 3887–3890.

43. S. Malkhandi, B. Yang, A. K. Manohar, A. Manivannan, G. K. S. Prakash, S. R. Narayanan, J. Phys. Chem. Lett. 2012, 3, 967–972.

Chapter IV. Enhancing Bifunctional Electrocatalytic Activities via Metal d-Band-Center-Lift in $Sm_{0.5}Sr_{0.5}CoO_{3-\delta}$ Perovskites

Ohhun Gwon,[†] Keunsu Choi,[†] Hansol Lee, Chanseok Kim, Jun Hee Lee,[*] and Guntae Kim[*]: This research will be published..

4.1 Introduction

In the development of energy conversion and storage systems such as metal-air batteries, water splitting, and solar synthetic reactors, the efficiency, cost, and environmental impact must be considered. In the interests of efficiency, the development of a catalyst key to improving catalytic activity for the oxygen reduction and oxygen evolution reactions (ORR and OER), while bifunctionality in both reactions is also necessary for various rechargeable applications.[1-5]

To date, various precious metal catalysts based on platinum, ruthenium oxide, and iridium oxide have been commonly employed due to their high catalytic activities. However, despite these high catalytic activities, the application of such precious metal catalysts in large-scale applications has been limited because of their high costs and rarity.[4, 5] In this regard, the discovery and design of non-precious bifunctional catalysts will be of direct benefit for efficient energy conversion and storage systems.[6-9] Recently, transition metal oxide materials such as cobalt, nickel, and copper-based oxides have received significant attention because of their bifunctional possibilities, low cost, and high catalytic activities.[10, 11] Among the various transition metal oxide materials reported to date, perovskite oxides ($ABO_{3-\delta}$; where A is a lanthanide or a rare earth element, B is a transition metal, and δ is an oxygen vacancy) were reported to be exceptional electrocatalysts because of their bifunctional catalytic activities, excellent cyclic stabilities, and high conductivities.[12-14]

To predict the OER activity of a transition metal oxide, the e_g occupancy has been proposed as a suitable descriptor, as in the case of the d-band theory for the ORR activity.[6, 15-17] Recent studies have also proposed a more general descriptor for the OER activity of a transition metal oxide, namely the difference between the metal d-band center and the oxygen p-band center (ΔE_{d-p}).[18-20]

Thus, we herein report our investigation into the correlation between band structures and ORR/OER catalytic activities by controlling the oxygen vacancies present in perovskite oxide catalysts. Among the various transition metals employed in the B-sites of perovskite oxides, the early transition metals (Cr, V, and Mn) exhibit higher M_d values compared to the O_p values, while the late transition metals (Co, Ni, and Cu) have lower M_d values.[21] To improve both the ORR and OER activities simultaneously, modification of the electronic structure is required, including bringing M_d (of the late transition metal) closer to the Fermi level (E_f) for a higher ORR activity, and reducing ΔE_{d-p} to enhance the OER activity. It is therefore expected that the M_d of the late transition metal, which can be increased by oxygen vacancies, will decrease the gap to E_f while reducing the gap to O_p, thereby

simultaneously improving both the ORR and OER activities.

In this research, $Sm_{0.5}Sr_{0.5}CoO_{3-\delta}$ (SSC; δ = 0.0, 0.1, and 0.2) perovskite oxide is selected, as its oxygen vacancies are easily controlled experimentally.[22] In addition, the half-doping of Sm and Sr at the A site should ensure a sufficient electron conductivity and facilitate artificial control of the oxygen vacancies. Using the oxygen vacancy-controlled SSC samples, analysis of the structural and electrochemical properties will be carried out. Furthermore, density functional theory (DFT) calculations will be employed to confirm that oxygen vacancies enhance the ORR activity by lifting the M_d close to E_f while improving the OER activity by reducing the gap between the M_d and the O_p values.

4.2 Experimental

4.2.1 Material Preparation

Pechini method was adopted to prepare $Sm_{0.5}Sr_{0.5}CoO_{3-\delta}$ (SSC) powders. Precursor solution was prepared with $Sm(NO_3)_3 \cdot 6H_2O$ (99.9%, metal basis, Sigma-Aldrich), $Sr(NO_3)_2$ (99+%, , Sigma-Aldrich), and $Co(NO_3)_2 \cdot 6H_2O$ (98+%, , Sigma-Aldrich) in distilled water with an appropriate amount of citric acid. The solutions were heated to 300 ºC in air, followed by combustion to form fine powders that were calcined at 600 ºC for 4 h and sintered in air at 950 ºC for 4 h.

To control the oxygen vacancy, the sintered sample was annealed at 800 ºC for 1 h and the sample quenched to 25 ºC (room temperature) or -196 ºC (liquid nitrogen).

The oxygen contents were determined by iodometric titration. First, an acid solution (12 wt.% HCl) is prepared, and an inert gas (N_2) is purged with the prepared acid solution. Then, excess KI (≥ 99.99% trace metals basis, Sigma-Aldrich) and sample were dissolved in the purged acid solution. Finally, the solution was titrated with sodium thiosulfate solution (0.05 M $Na_2S_2O_3 \cdot 5H_2O$, Sigma-Aldrich).

4.2.2 Material Analysis

The crystallographic structures of the materials were characterized by X-ray diffraction (XRD; D8 Advance, Bruker diffractometer with Cu Kα radiation) at a scan rate of 0.6 º min^{-1} with a 2θ range of 20 º to 60 º. Scanning electron microscopy (SEM, Nanonova 230, FEI) was used to capture their morphologies. The Brunauer–Emmett–Teller (BET, BELSORP-max, MicrotracBEL Corp.) measurement was carried out for the surface area of SSC using N_2 at 77 K. The particle size distribution of SSC was measured with a laser scattering particle size distribution analyzer (LA-920, Horiba).

4.2.3 Electrochemical Characterization

X-ray photoelectron spectroscopy (XPS) analyses were performed on ESCALAB 250XI from Thermo Fisher Scientific with a monochromated Al-Kα (ultraviolet He1, He2) X-ray source. The base pressure inside the spectrometer during analysis was 1 x 10^{-10} mmHg.

Catalyst inks were prepared by dispersing 20 mg of catalyst in 0.45 ml of ethanol, 0.45 ml of isopropyl alcohol, and 0.1 ml of 5 wt. % Nafion solution (Sigma-Aldrich 274704). The loading density of the catalyst was fixed at 0.8 mg cm^{-2} (disk electrode area = 0.1256 cm^2).

Linear sweep voltammetry (LSV) was measured on disk and ring electrodes simultaneously by a computer-controlled potentiostat (Biologic, VMP3) at 1600 rpm controlled by a rotating disk electrode system (Biologic, RRDE-3A). A platinum wire electrode and an Hg/HgO electrode (Hg/HgO vs. NHE is 0.140 V (NaOH, 1 M)) were used as the counter and reference electrodes, respectively. An aqueous solution of 0.1 M KOH was used as the electrolyte. ORR polarization curves

were obtained on the disk electrode from a cathodic sweep from 0.1 V to -0.9 V (vs. Hg/HgO) at 10 mV s^{-1} after several cycles of CVs. Voltage of 0.4 V was applied to the ring electrode to estimate the amount of peroxide generated from the disk electrode. The anodic sweeps from 0.35 V to 0.9 V (vs. Hg/HgO) were presented as OER polarization curves. The other conditions were the same as those applied for the ORR polarization curves.

4.2.4 DFT Calculations

We carried out density functional theory (DFT) calculations by using Vienna Ab-initio Simulation Package (VASP). The exchange-correlation functional was described by the Perdew-Burke-Ernzerhof (PBE) functional with the Generalized Gradient Approximation (GGA) method.[23-25] The Hubbard U (U_{eff} = 3.5 eV) correction was applied to the Co 3d electrons and pseudopotentials generated under a projector-augmented plane-wave method scheme.[26] We used 2×2×2 perovskite supercells for bulk calculation and 3×3×3 k-points were sampled based on the Monkhorst-Pack method.[27] We determined band centers, O 2p-band and metal 3d-band, by taking the weighted mean energy for both occupied and unoccupied states in the projected density of states. We used nine layered slabs with √2×√2 surfaces for slab calculations with 6×6×1 k-points. The four bottom layers of the slab were fixed at the optimized bulk lattice constant, while the top five layers and adsorbents were fully relaxed. The dipole correction was considered in all the slab calculations.[28] The convergence criteria for the optimization of structure were set to 0.02 eV $Å^{-1}$. We used the Bader charge analysis to identify the number of electrons in each atom.[29]

4.3 Results and Discussions

The $Sm_{0.5}Sr_{0.5}CoO_3$ (SSC30, δ = 0) perovskite oxide was initially synthesized using the conventional Pechini method and sintered at 950 °C for 4 h. To control the number of oxygen vacancies, SSC30 was subsequently annealed at 800 °C for 1 h then quenched to 25 °C (room temperature) or −196 °C (liquid nitrogen) to give either $Sm_{0.5}Sr_{0.5}CoO_{2.9}$ (SSC29, δ = 0.1) or $Sm_{0.5}Sr_{0.5}CoO_{2.8}$ (SSC28, δ = 0.2), respectively. The annealing temperature was selected to prevent any changes in the geometries of the SSC, which may affect the catalytic performance.[10, 12, 13] Iodometric titrations were performed to measure the number of oxygen vacancies (δ).

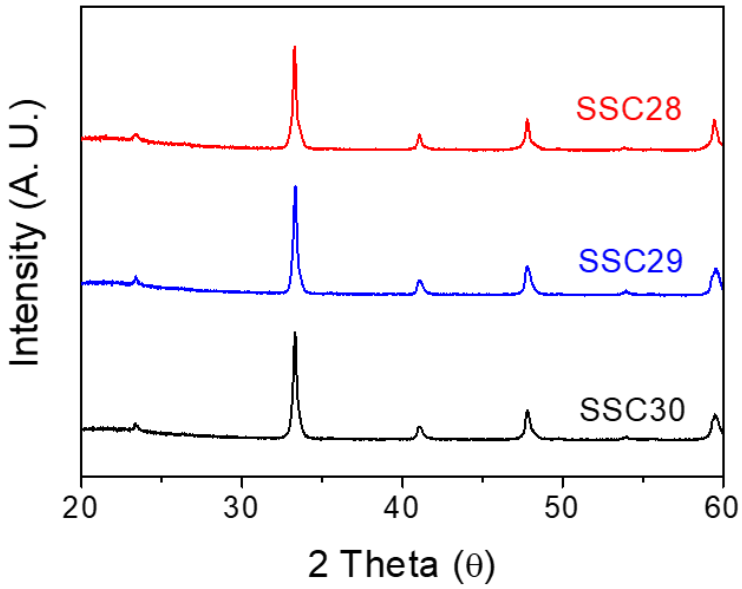

Figure 4.1 XRD of SSC30, SSC29, and SSC28.

The crystal space groups, particle sizes, and surface areas of the SSC samples were then determined. More specifically, X-ray diffraction (XRD) was performed to confirm the crystal structures, and indicated that both samples were typical cubic perovskite structures (Fig. 4.1). Scanning electron microscopy (SEM) images were recorded to examine the microstructures, where a relatively constant particle size of ~2.5 μm (Fig. 4.2 and 4.3) indicated an insensitivity to the number of oxygen defects. The prepared SSC samples also exhibited similar surface areas (i.e., 1.75, 1.81, and 1.74 $m^2\ g^{-1}$ for δ = 0.0, 0.1, and 0.2, respectively, Fig. 4.4). These results indicated that the SSC samples were well-controlled, while confirming that the oxygen vacancies did not drastically alter the crystal space group, particle size, or surface area.

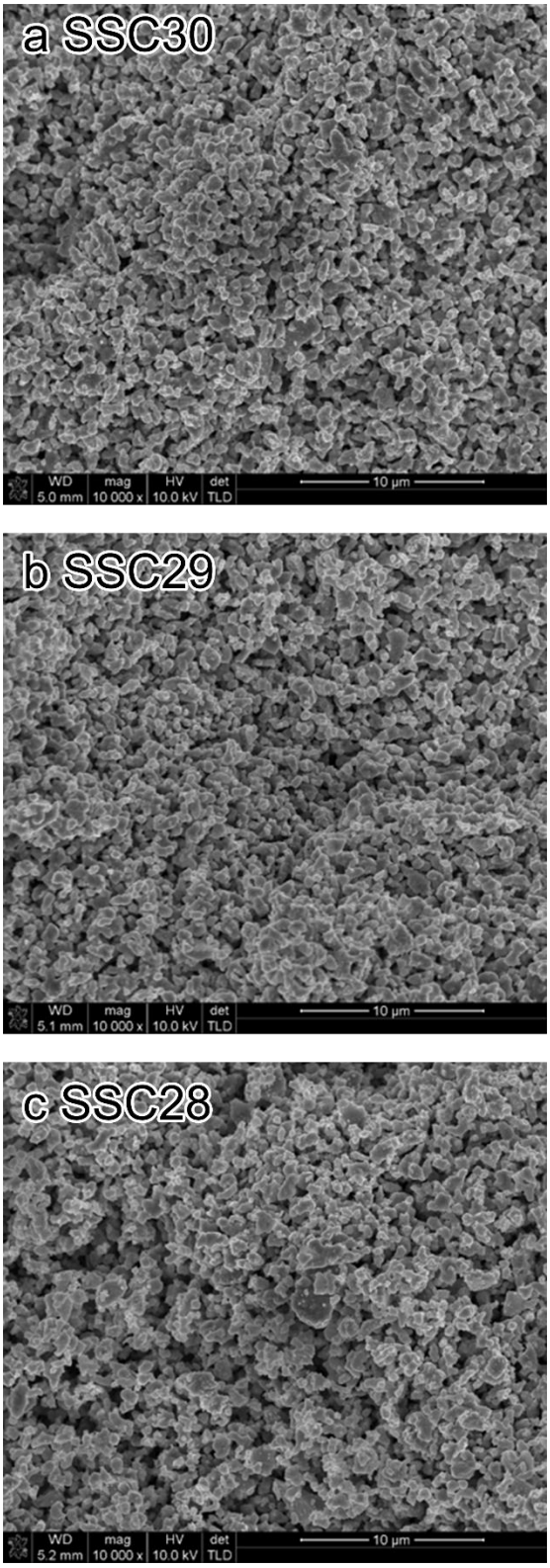

Figure 4.2 SEM images of (a) SSC30, (b) SSC29, and (c) SSC28.

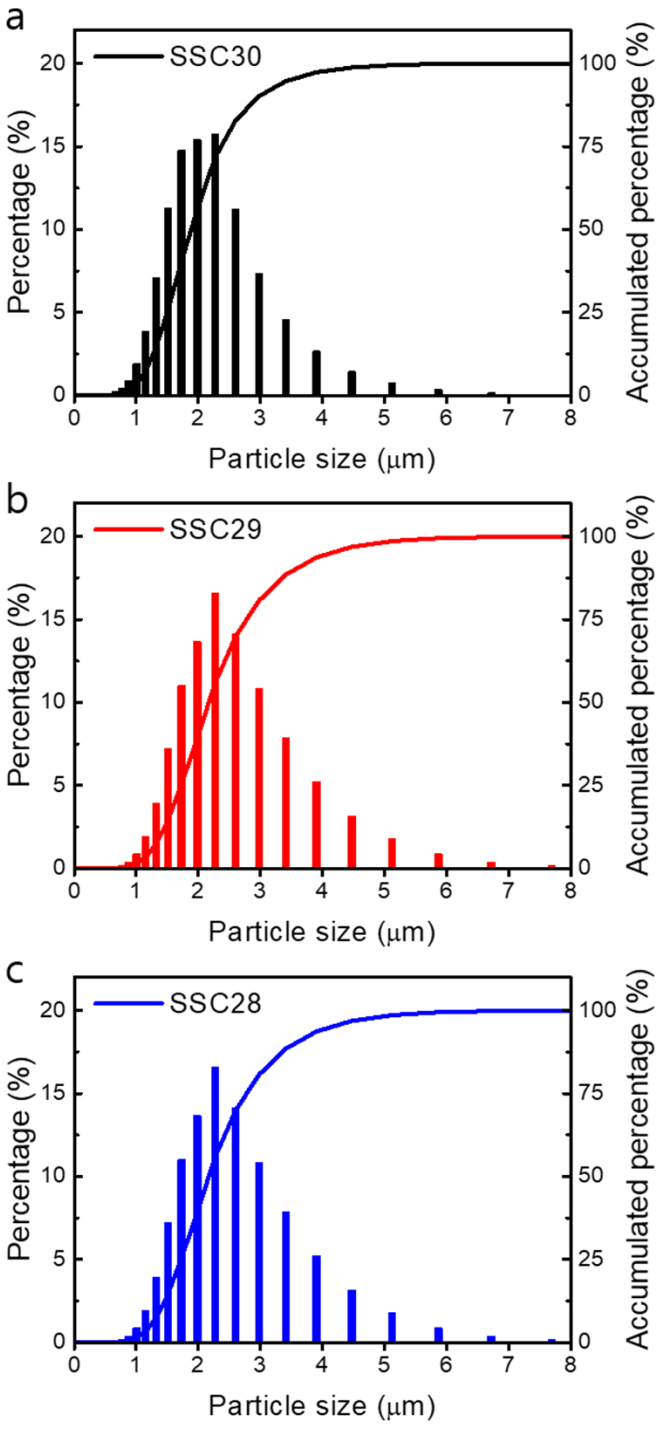

Figure 4.3 Particle size distribution of (a) SSC30, (b) SSC29, and (c) SSC28.

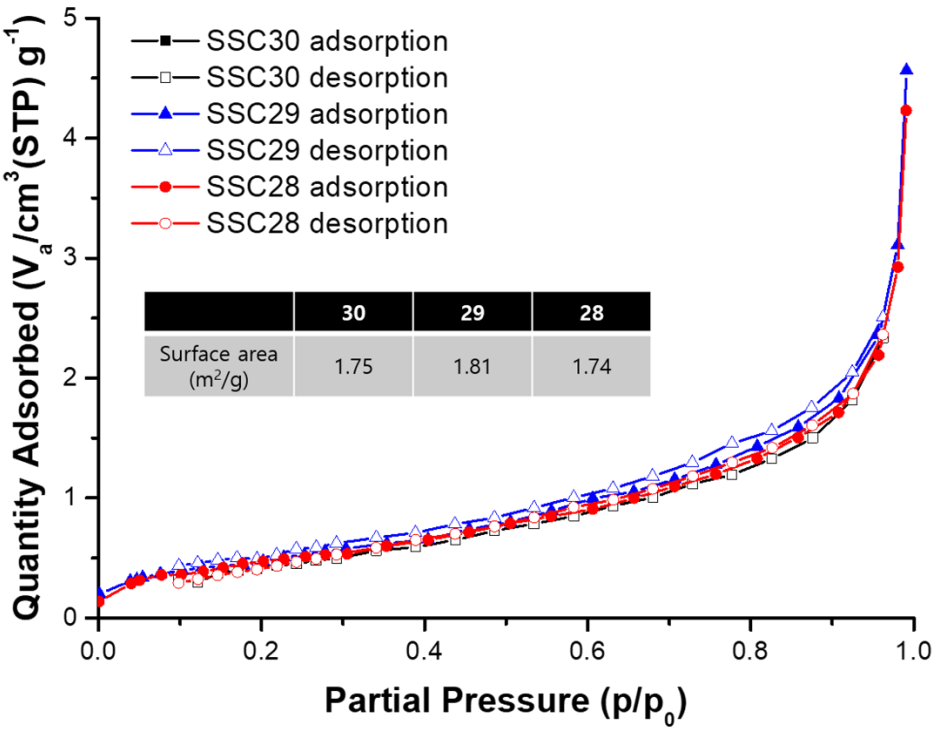

Figure 4.4 N_2 adsorption–desorption isotherms of SSC30, SSC29, and SSC28. The surface area of each samples is 1.75, 1.81 and 1.74 m^2 g^{-1}, respectively.

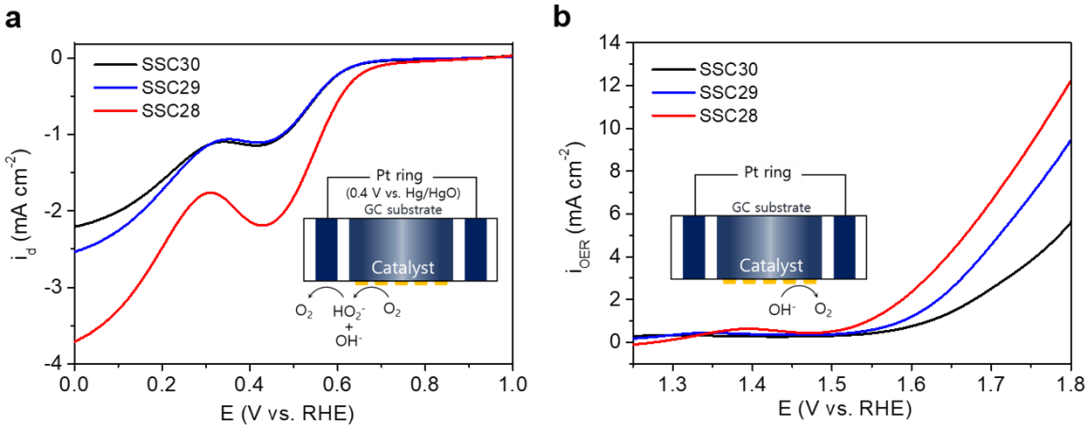

Figure 4.5 (a) ORR and (b) OER activity of the $Sm_{0.5}Sr_{0.5}CoO_{3-\delta}$ (δ = 0.0, 0.1, and 0.2) in O_2-saturated 0.1 M KOH at a scan rate of 10 mV s^{-1} and a rotation rate of 1,600 rpm.

Rotating ring-disk electrode (RRDE) measurements were then carried out to check the ORR and OER catalytic activities of the various SSC samples (Fig. 4.5). The ORR onset potential of the SSC varied from −0.26 to −0.2 V (vs Hg/HgO) at −0.1 mA cm^{-2} upon decreasing the SSC oxygen content (Fig.

4.5(a)). Moreover, SSC28 exhibited a superior current density to the samples with higher oxygen contents. In addition, from the disc and ring currents of the SSC samples, additional ORR catalytic information could be calculated, including the electron transfer number (n) and the percentage yield of peroxide species (HO_2^-), as shown in Fig. 4.6.

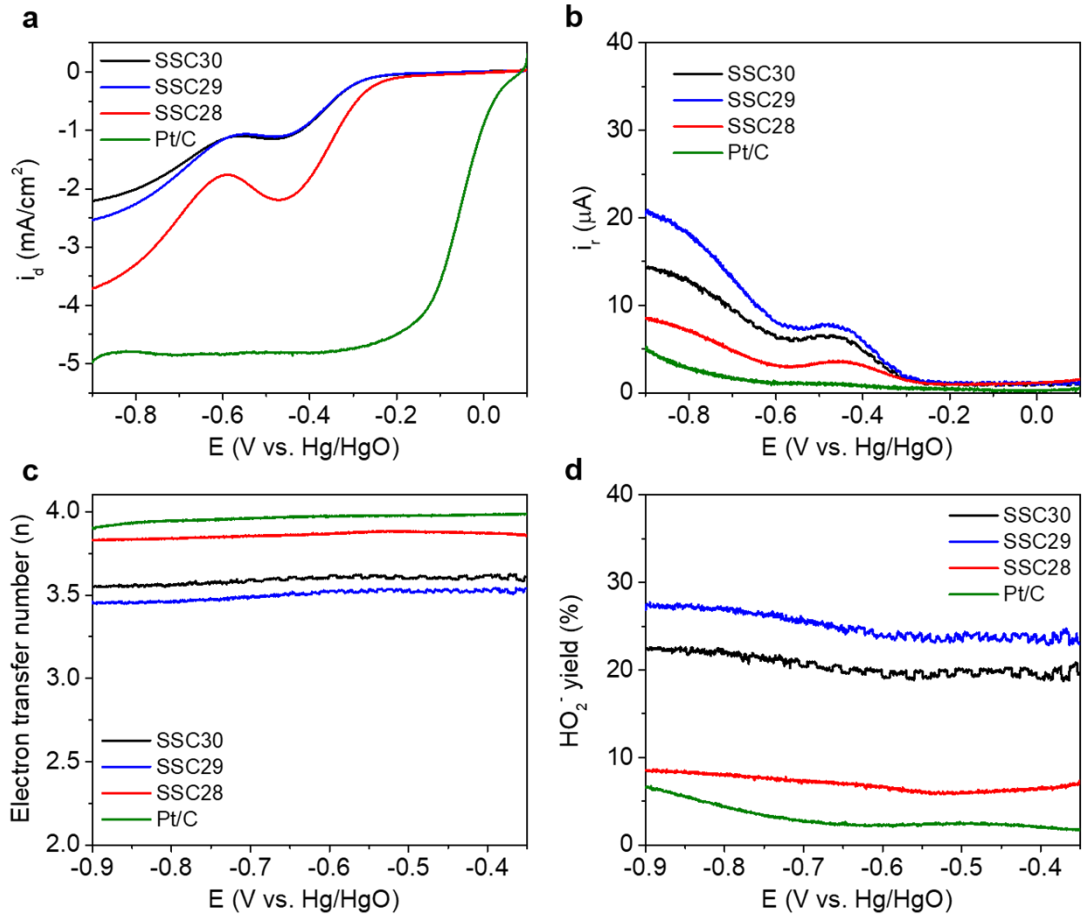

Figure 4.6 (a) Disc current, (b) ring current, (c) electrons transfer number, and (d) peroxide yield of ORR are measured by a RRDE test. The test is operated in O_2-saturated 0.1 M KOH at 10 mV s^{-1} scan rate and 1,600 rpm rotation rate from 0.1 V to -0.9 V.

Thus, n (as shown in 4.6(c)), was calculated using equation (1),

$$n = 4 \times \frac{I_d}{I_d + I_r/N} \qquad (1)$$

where I_d, I_r, and N are disc current, ring current, and experimental collection efficiency, respectively. The experimentally determined collection efficiency (N) was 0.41. The electron transfer numbers of SSC30, SSC29, and SSC28 were 3.55, 3.45, and 3.83, respectively. As the oxygen vacancy number increased from 0 to 0.2, the electron transfer number also increased close to the ideal ORR (4 electron transfer).

The yield of peroxide species (HO_2^-) during the ORR process was calculated as follows:

$$HO_2^-(\%) = 200 \times \frac{I_r/N}{I_d + I_r/N} \qquad (2)$$

More specifically, the calculated HO_2^- yields for the SSC samples decreased from approximately 25 to 9% upon increasing the number of oxygen vacancies.

In addition, the OER onset potential of the SSC decreased from 0.72 to 0.64 V (vs Hg/HgO) at 1 mA cm^{-2} with a decrease in the SSC oxygen content (Fig. 4.5(b)), and the current density of SSC28 increased compared to the other samples. Overall, well-controlled oxygen vacancies were found to simultaneously improve the OER and ORR performances.

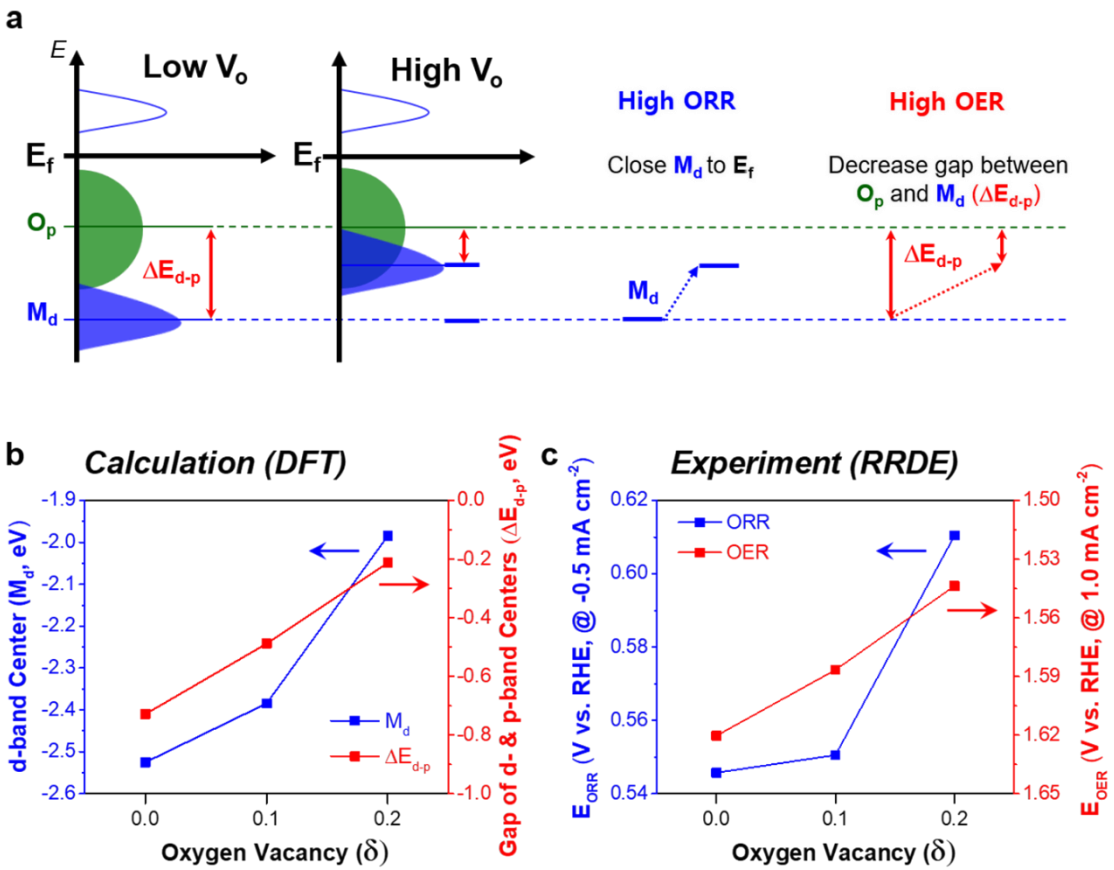

Figure 4.7 (a) Schematic rigid band diagrams of the late transition metal oxide. (b) Variation in the M_d energy levels and the energy level differences between M_d and O_p (ΔE_{d-p}) with the number of oxygen defects in the SSC. All band centers are relative to the Fermi level. (c) The ORR and OER experimental overpotentials of the SSC at −0.5 and 1.0 mA cm^{-2}, respectively.

DFT calculations were then performed to account for the improvements in the ORR and OER activities. As shown in previous studies, the key parameters for describing the band structures of correlated electronic materials are the Hubbard intra-d-orbital electron-electron Coulomb interaction

(U_{dd}) and the gap of band energy ($\Delta E_{d-p} = M_d - O_p$, where M_d and O_p are the d-band and p-band centers, respectively).[30, 31] Furthermore, in terms of the electronic structure and coordination properties, M_d and O_p are highly correlated with the ORR and OER activities. Thus, to achieve simultaneously efficient ORR and OER activities, it is necessary to bring the M_d energy level close to the Fermi level and decrease the gap between M_d and O_p, respectively.

The energy gaps of the SSC samples were calculated to be −0.73, −0.49, and −0.21 eV for SSC30, SSC29, and SSC28, respectively, which are smaller gaps than that of cobaltite U_{dd} (~3.5 eV).[32] According to the DFT calculations, the presence of oxygen vacancies reduces the energy gap between M_d and O_p by bringing M_d close to the Fermi level (E_f), as shown in Fig. 4.7(b). It is expected that the ORR and OER activities of SSC are simultaneously improved by the reduced ΔE_{d-p} and the raised M_d energy level. The onset potentials of the ORR and the OER were also measured experimentally at −0.5 and 1.0 mA cm^{-2}, respectively, to compare the intrinsic activities of the SSC samples, and both activities were found to concurrently improve as the number of oxygen vacancies increased (Fig. 4.7(c)). A comparison of the calculated (Fig. 4.7(b)) and experimental data (Fig. 4.7(c)) shows a similar increasing trend for the ORR (nonlinear) and the OER (linear) activities in accordance with the oxygen vacancies, indicating the strong couplings of the ORR to M_d and of the OER to ΔE_{d-p}, both of which were controlled by the oxygen vacancies.

To understand the ORR improvement in more detail, the shift in M_d was also investigated through DFT calculations. Indeed, the DFT results were in agreement with the XPS measurements for the distribution of Co^{4+}, Co^{3+}, and Co^{2+} ions with the oxygen vacancies (Fig. 4.8(a) and 4.8(b)), and measurement of the cobalt bonding states in the SSC samples by X-ray photoelectron spectroscopy (XPS) showed that the main peaks are located at binding energies of 780.1 eV (Co $2p_{3/2}$) and 796.6 eV (Co $2p_{1/2}$) (Fig. 4.9). Through Gaussian fitting, the distribution of Co^{3+} and $Co^{4+/2+}$ in the SSC samples could be distinguished. Furthermore, the valence state distributions and the M_d energy levels of the cobalt ions in the theoretical SSC unit cells (3.000, 2.875, and 2.750 represent the number of oxygen atoms in the unit cells) were calculated.[32]

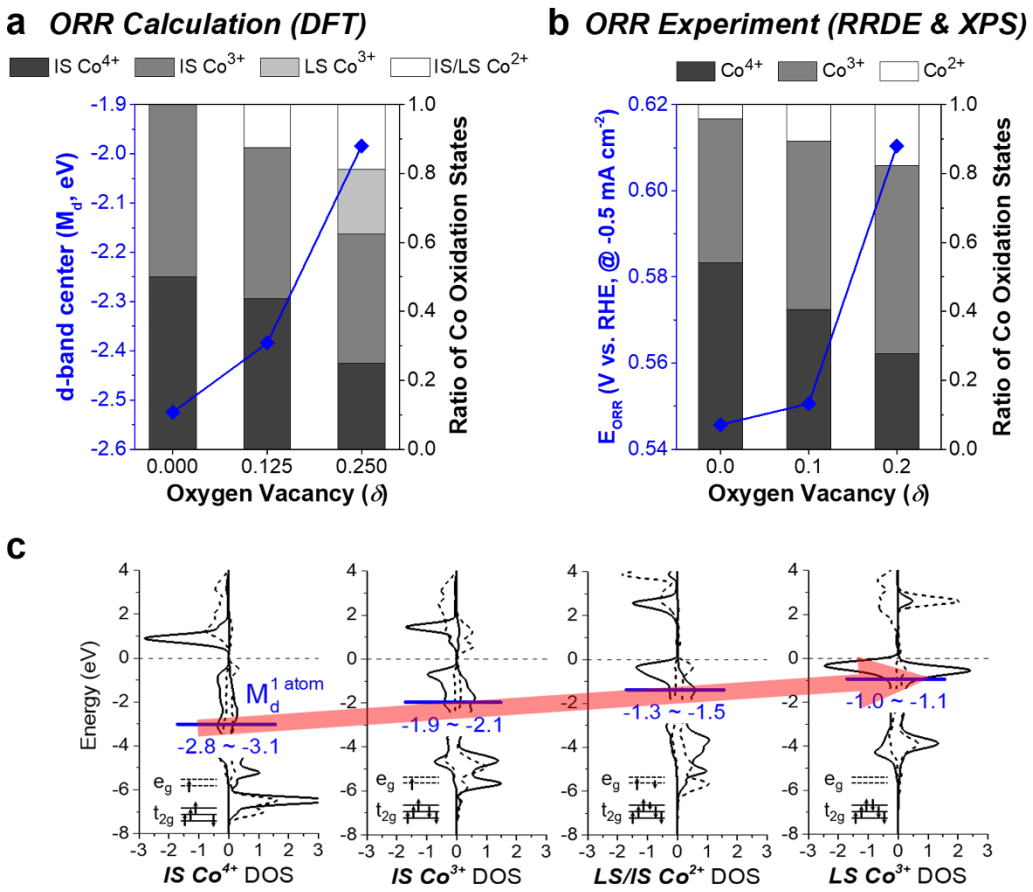

Figure 4.8 (a) Theoretical ratio of Co ions according to the number of oxygen defects. (b) Experimental ratio of Co ions according to the number of oxygen vacancies measured by XPS (Fig. 4.9). (c) From left to right, intermediate spin states (IS) of Co^{4+}, IS of Co^{3+}, crossover of Co^{2+} between intermediate- and low-spin states (IS/LS), and LS of Co^{3+}. Positive values indicate majority spin states while negative values indicate minority spin states. The black dashed line represents the e_g orbital and the black solid line represents the t_{2g} orbital of the Co 3d orbital. The blue solid line indicates the calculated d-band center (M_d) position. The dashed horizontal line appears at the Fermi level, with occupied states at negative energies and unoccupied states at positive energies.

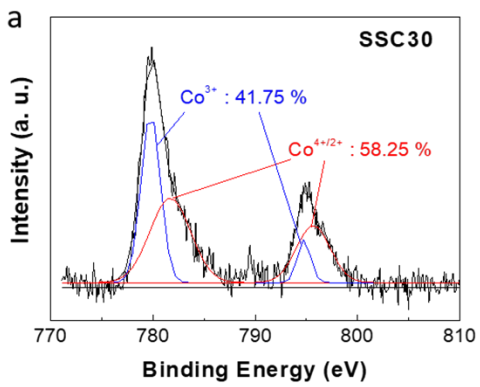

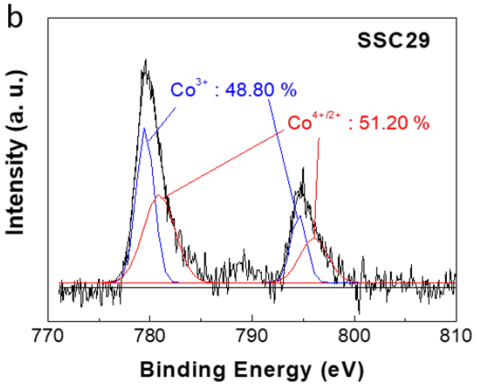

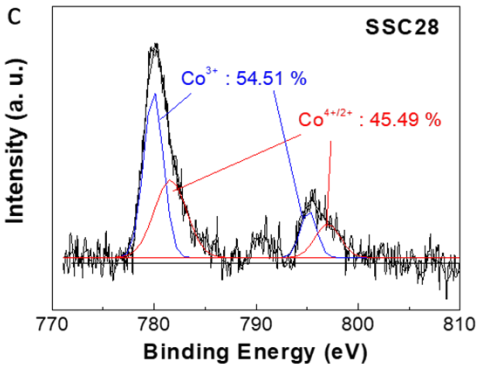

δ	Co^{2+}	Co^{3+}	Co^{4+}
0.0	4.13 %	41.75 %	54.13 %
0.1	10.60 %	48.80 %	40.60 %
0.2	17.75 %	54.51 %	27.75 %

Figure 4.9 XPS measurements of (a) SSC30, (b) SSC29, and (c) SSC28.

The calculated average M_d values of SSC3.000, SSC2.875, and SSC2.750 were −2.53, −2.38, and −1.98 eV, respectively (Fig. 4.8(a)). In the absence of oxygen vacancies (SSC3.000), IS Co^{4+} (S = 3/2) and IS Co^{3+} (S = 1) are equally mixed. In the SSC with one vacancy out of 24 oxygens (SSC2.875), Co ions doped with electrons generated by the vacancy changed from IS Co^{3+} (S = 1) to IS/LS Co^{2+} (IS: S = 3/2, LS: S = 1/2). As a result, the average M_d of SSC2.875 (−2.38 eV) increased slightly from the M_d of SSC3.000 (−2.53 eV). In the SSC with two oxygen vacancies (SSC2.750), additional electrons changed IS Co^{4+} (S = 3/2) and IS Co^{3+} (S = 1) to LS Co^{3+} (S = 0) and IS/LS Co^{2+} (IS: S = 3/2, LS: S = 1/2). The average M_d of SSC2.750 (−1.98 eV) increased significantly compared to those of SSC2.875 (−2.38 eV) and SSC3.000 (−2.53 eV), as the Md value increased due to the reduction of Co with its spin crossover from IS to LS.

To understand the M_d enhancement caused by the presence of oxygen vacancies, we examined the density of states (DOS) for the Co ions of different oxidation states (Fig. 4.8(c)). The energy level of Co^{3+} is higher than that of Co^{4+} because Co^{3+} has a lower effective nuclear charge due to the presence of an additional electron. Among the Co^{3+} ions, LS Co^{3+} has a significantly higher M_d (−1.01 eV) than IS Co^{3+} (−2.15 eV) as local volume expansion of the oxygen vacancy sites compresses the adjacent octahedra where the strengthened crystal field results in spin crossover from IS Co^{3+} to LS Co^{3+}.

According to the theoretical and experimental results, Co^{4+} ions are gradually replaced by the less oxidized Co ions upon increasing the number of oxygen vacancies. At the same time, M_d increases nonlinearly from −2.53 to −1.98 eV as the number of vacancies increases. This increase in M_d is consistent with the experimental nonlinear trend of the ORR performance improvement in the RRDE measurement (blue lines in Fig. 4.8(a) and (b)). These remarkable quantitative and qualitative consistencies between the theoretical and experimental results support the conclusion that the M_d shift is related to the oxidation state and the spin state of Co.

Late transition metal oxide materials tend to exhibit high OER activities due to the slightly negative ΔE_{d-p}, but the ORR activity remains insufficient due to the large gap between the Fermi energy and M_d. From this band structure point of view, bringing M_d close to both the Fermi level and to O_p should result in efficient ORR and OER activities.[13, 14] Late transition metal oxide materials should therefore be suitable for improving the bifunctionality due to the lower value of M_d compared to O_p (Fig. 4.7(a)), and the generation of oxygen vacancies lifts M_d close to both the Fermi level and O_p, simultaneously.[21]

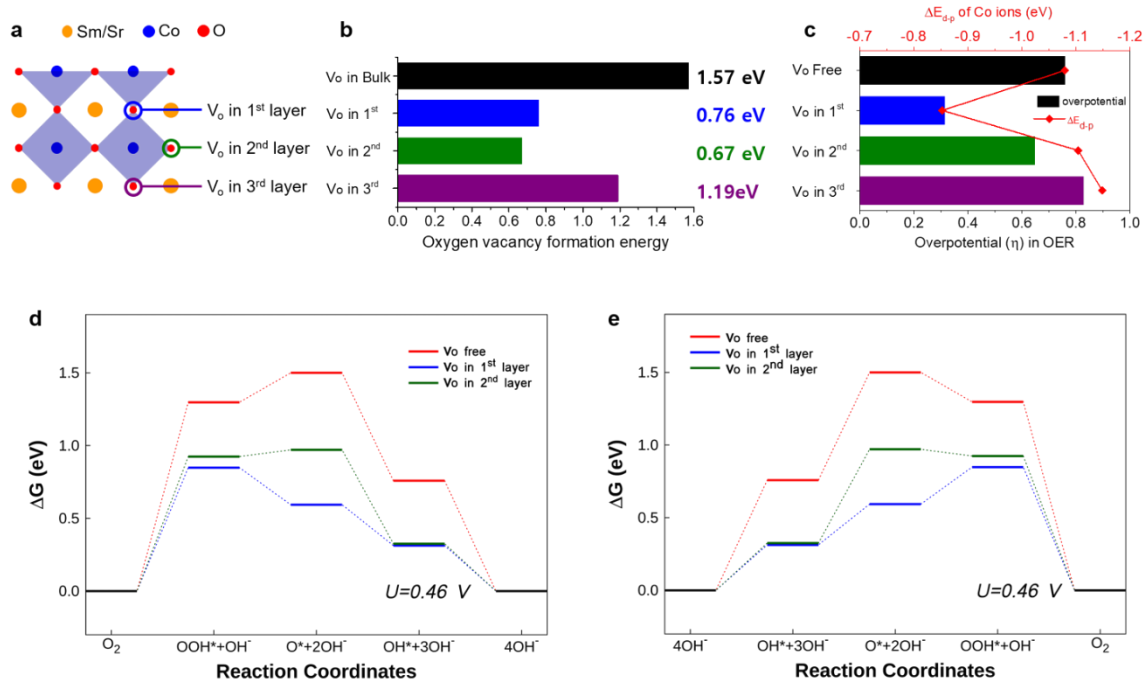

Figure 4.10 (a) The illustration shows the position of oxygen vacancies (V_O) for the various vacancy configurations. The blue, green, and purple circles represent the positions of oxygen vacancies in the 1st, 2nd, and 3rd layers, respectively. (b) Formation energies of oxygen vacancies for the bulk, 1st, 2nd, and 3rd layers. (c) The overpotential and ΔE_{d-p} values of the OER based on the oxygen vacancy position. (d) and (e) The calculated free energy profiles of the ORR and the OER on the (001) surface of SSC under equilibrium potential in alkaline media.

As catalytic reactions take place on the catalyst surface, we then investigated the effects on the catalytic activities of oxygen vacancies close to the surface. For the purpose of these calculations, we used a slab perovskite with nine layers and introduced oxygen vacancies in the 1st (V1-SSC), 2nd (V2-SSC), and 3rd (V3-SSC) layers, as shown in Fig. 4.10(a). The formation energies of these oxygen vacancies were 0.76, 0.67, and 1.19 eV, respectively, which are significantly smaller than the average formation energy of an oxygen vacancy in the bulk (P-SSC, 1.57 eV), indicating that oxygen vacancy formation is more facile close to the surface (Fig. 4.10(b)). The position of the oxygen vacancy also affects the value of ΔE_{d-p}, as V1-SSC exhibited the smallest ΔE_{d-p} among all configurations (Fig. 4.10(c)).

Finally, we calculated the free energies for the ORR and OER pathways under equilibrium potential at pH 13 (calculation details are given in the supporting information). In the ORR pathway, the overpotentials (η) of P-, V1-, and V2-SSC were 1.30, 0.85, and 0.92, respectively (Fig. 4.10(d)). The closer the oxygen vacancies are to the surface, the greater the promotion of the catalytic reaction. The first reaction step, which corresponds to the formation of OOH on the surface, acts as the rate determining step (RDS) for all configurations in the ORR (Fig. 4.10(d)). In contrast, in the OER, the RDS depends on the position of the oxygen vacancy; the second step for V2-SSC and the first step for all other samples (Fig. 4.10(e)). In the adsorbate evolution mechanism (AEM) pathway of the OER, the overpotentials of P-, V1-, and V2-SSC were 0.76, 0.31, and 0.65, respectively. The free energy profile for the lattice oxygen mediated (LOM) pathway of the OER is given in Fig. 4.11. As shown in Fig. 4.10(c), the overpotentials and ΔE_{d-p} values of the surface are highly correlated, and both results indicate that the oxygen vacancy in the 1st layer provides the greatest promotion of the OER activity.

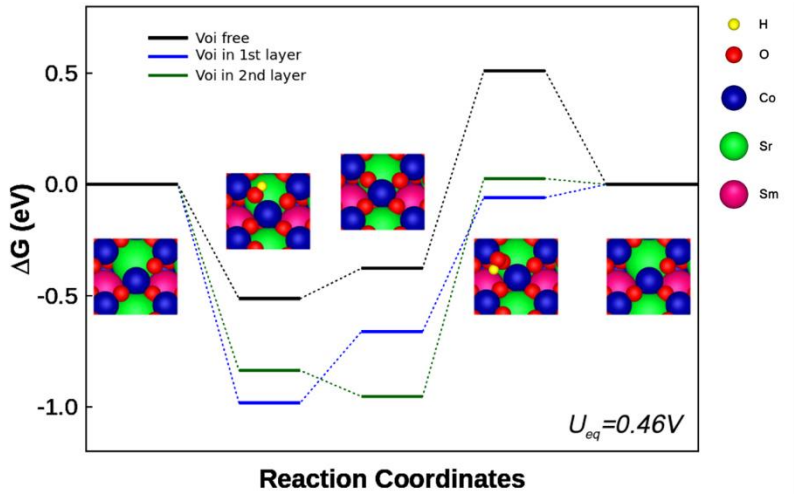

Figure 4.11. The overpotential of three configurations (Voi free, in 1st layer, and in 2nd layer) for LOM pathway are 0.89, 0.60, 0.98 eV, which are relatively high compared to that for AEM pathway. The rate-determining step in all the configurations are third reaction step. Voi represents internal oxygen vacancy existing below the surface.

4.4 Conclusion

In summary, we investigated the relationship between the bifunctionality and electronic structure of modified perovskite oxides by introducing oxygen vacancies. More specifically, cobalt-based perovskite oxides are late transition metal oxides that can be bifunctional catalysts for the ORR and the OER. The bifunctional improvement was supported by the well-matched results of both theoretical DFT calculations and experimental electrochemical measurements. As the concentration of oxygen vacancies increases without geometric changes, the ORR and OER activities of the SSC were enhanced, which was confirmed by experimental RRDE measurements. In addition, DFT calculations showed that the relative band positions of cobalt (M_d) in the SSC samples were shifted by the systematic control of oxygen vacancies, resulting in SSC28 being a bifunctional catalyst. In conclusion, the corresponding electronic structure changes of Co state upon the variation of oxygen vacancies play a key role to determine ORR and OER properties. In this regard, we suggest that late transition metal oxides, in which the M_d level is located below the O_p level, can be utilized as efficient bifunctional catalysts by the introduction of oxygen vacancies, and we expect that this approach can accelerate the discovery and design of highly efficient, bifunctional catalysts.

References

1. A. J. Bard, M. A. Fox, Acc. Chem. Res. 1995, 28, 141.

2. M. Winter, R. J. Brodd, Chem. Rev. 2005, 105, 1021.

3. N. S. Lewis, D. G. Nocera, Proc. Natl. Acad. Sci. 2006, 103, 15729.

4. O. Gwon, C. Kim, O. Kwon, H. Y. Jeong, H. -K. Park, J. Shin, Y. -W. Ju, G. Kim, J. Electrochem. Soc. 2016, 163, A1893.

5. Y. Bu, O. Gwon, G. Nam, H. Jang, S. Kim, Q. Zhong, J. Cho, G. Kim, ACS Nano. 2017, 11, 11594.

6. J. Suntivich, K. J. May, H. A. Gasteiger, J. B. Goodenough, Y. Shao-Horn, Science. 2011, 334, 1383.

7. J. Suntivich, H. A. Gasteiger, N. Yabuuchi, H. Nakanishi, J. B. Goodenough, Y. Shao-Horn, Nat. Chem. 2011, 3, 546.

8. M. Armand, J. M. Tarascon, Nature. 2008, 451, 652.

9. Y. C. Lu, Z. Xu, H. A. Gasteiger, S. Chen, K. Hamad-Schifferli, Y. Shao-Horn, J. Am. Chem. Soc. 2010, 132, 12170.

10. C. Hwang, O. Gwon, H. Jo, K. M. Ok, G. Kim, ChemElectroChem. 2017, 4, 468.

11. Y. Liang, Y. Li, H. Wang, J. Zhou, J. Wang, T. Regier, H. Dai, Nat. Mater. 2011, 10, 780.

12. D. -G. Lee, O. Gwon, H. -S. Park, S. H. Kim, J. Yang, S. K. Kwak, G. Kim, H. -K. Song, Angew. Chem. Int. Ed. 2015, 54, 15730.

13. S. Gupta, W. Kellogg, H. Xu, X. Liu, J. Cho, G. Wu, Chem. Asian J. 2016, 11, 10.

14. A. Grimaud, K. J. May, C. E. Carlton, Y. -L. Lee, M. Risch, W. T. Hong, J. Zhou, Y. Shao-Horn, Nat. Commun. 2013, 4, 2439.

15. B. Hammer, J. K. Nørskov, Adv. Catal. 2000, 45, 71.

16. J. -I. Jung, H. Y. Jeong, J. -S. Lee, M. G. Kim, J. Cho, Angew. Chem. Int. Ed. 2014, 53, 4582.

17. J. R. Petrie, V. R. Cooper, J. W. Freeland, T. L. Meyer, Z. Zhang, D. A. Lutterman, H. N. Lee, J. Amer. Chem. Soc. 2016, 138, 2488.

18. X. Cheng, E. Fabbri, M. Nachtegaal, I. E. Castelli, M. E. Kazzi, R. Haumont, N. Marzari, T. J. Schmidt, Chem. Mater. 2015, 27, 7662.

19. J. T. Mefford, X. Rong, A. M. Abakumov, W. G. Hardin, S. Dai, A. M. Kolpak, K. P. Johnston, K. J. Stevens, Nat. Commun. 2016, 7, 11053.

20. A. Grimaud, O. Diaz-Morales, B. Han, W. T. Hong, Y. -L. Lee, L. Giordano, K. A. Stoerzinger, M. T. M. Koper, Y. Shao-Horn, Nat. Chem. 2017, 9, 457.

21. M. Imada, A. Fujimori, Y. Tokura, Rev. Mod. Phys. 1998, 70, 1039.

22. S. Yoo, T. -H. Lim, J. Shin, G. Kim, J. Power Sources. 2013, 226, 1.

23. G. Kresse, J. Furthmüller, Phys. Rev. B. 1996, 54, 11169.

24. G. Kresse, J. Hafner, Phys. Rev. B. 1993, 47, 558.

25. J. P. Perdew, K. Burke, M. Emzerhof, Phys. Rev. Lett. 1996, 77, 3865.

26. P. E. Blöchl, Phys. Rev. B. 1994, 50, 17953.

27. H. J. Monkhorst, J. D. Pack, Phys. Rev. B. 1976, 13, 5188.

28. G. Makov, M. C. Payne, Phys. Rev. B. 1995, 51, 4014.

29. M. Yu, D. R. Trinkle, J. Chem. Phys. 2011, 134, 064111.

30. N. F. Mott, R. Peierls, Proc. Phys. Soc. 1937, 49, 72.

31. N. F. Mott, Proc. Phys. Soc. 1949, 62, 416.

32. A. M. Ritzmann, M. Pavone, A. B. Muñoz-García, J. A. Keith, E. A. Carter, J. Mater. Chem. A. 2014, 2, 8060.

Chapter V. Optimization of $La_xSr_{1-x}CoO_{3-\delta}$ perovskite cathodes for intermediate temperature solid oxide fuel cells through the analysis of crystal structure and electrical properties

5.1 Introduction

Solid oxide fuel cells (SOFCs) have been explored as a new power generation device on the strengths of their high conversion efficiency, low emissions, and excellent fuel flexibility. The requirement for high operating temperature (1073-1273 K) of conventional SOFCs, however, leads to notable problems such as high operating costs and unintended reactions between the electrolyte and the electrode. The focus of recent research on SOFC technology has shifted towards intermediate temperature (IT) operation ranging from 773 to 973 K. The reduction of operating temperature, on the other hand, leads to a significant decrease in cathode activity. Therefore, the development of efficient cathode materials for intermediate temperature is considered an important avenue of research for IT-SOFC applications.[1-8]

A suitable cathode material for IT-SOFCs should have high oxide ionic and electronic conductivities and high catalytic activity for the oxygen reduction reaction as well as a thermal expansion coefficient that is compatible with the electrolyte. Mixed ionic and electronic conductors (MIECs) containing Mn, Fe, Co, and/or Ni with the capability to conduct oxygen ions and electrons simultaneously are strong candidates for IT-SOFC cathodes. Among those various MIEC oxides, perovskite oxides continue to dominate research on SOFC cathodes, and there has been increasing interest in Co-containing oxides due to their high electronic and oxide ion conductivity.[9-13]

Among the Co-containing oxides, $SrCoO_{3-\delta}$ is an important parent compound that can be further developed into many functional materials. The high oxygen vacancy concentration in $SrCoO_{3-\delta}$ is useful for oxygen ionic conduction and the oxygen reduction reaction (ORR) on the cathode interface. However, $SrCoO_{3-\delta}$ is changed from a cubic to hexagonal phase with a 2H-$BaNiO_3$-type structure below about 1173 K.[14] These structural instabilities thus limit this material in terms of further SOFC applications.

It is therefore necessary to inhibit the phase transition at the SOFC operating temperature to stabilize the perovskite phase in $SrCoO_{3-\delta}$ oxides by adding various dopants.[15, 16] Recently, in this regard, lanthanide doped strontium cobalt oxides, $Ln_xSr_{1-x}CoO_{3-\delta}$ (Ln = La, Pr, Nd, Sm, and Gd), have been extensively investigated on the basis of their good electrical conductivity and performance as IT-SOFC cathode materials. Among them, $La_xSr_{1-x}CoO_{3-\delta}$ (LSC) is commonly used as a cathode material for IT-SOFCs due to its superior electrical properties and higher catalytic activity, as well as good thermal stability at operating temperatures.[17-27] However, the aforementioned studies focused on only a few specific compositions in $La_xSr_{1-x}CoO_{3-\delta}$ oxides and sufficient data on electrochemical

performance has not been obtained to date.

We, therefore, optimized the effect of lanthanum doping through a systematic evaluation of the structural and electrochemical characteristics of a LSC cathode with regard to its application as an IT-SOFC cathode material.

In this study, we report excellent electrochemical performance under operating conditions via La doping into the A site of the potential cathode material $Sr_{1-x}CoO_{3-\delta}$. In addition, we examine the structural characteristics and electrochemical properties of $La_xSr_{1-x}CoO_{3-\delta}$ (x = 0.2, 0.3, 0.4, 0.5, 0.6 and 0.7) with respect to its application as an IT-SOFC cathode material.

5.2 Experimental

$La_xSr_{1-x}CoO_{3-\delta}$ (x = 0.2, 0.3, 0.4, 0.5, 0.6, and 0.7) cathode materials were synthesized by a Pechini method. Stoichiometric amounts of $La(NO_3)_3 \cdot 6H_2O$ (Aldrich, 99.9%, metal basis), $Sr(NO_3)_2$ (Aldrich, 99+%), $Co(NO_3)_2 \cdot 6H_2O$ (Aldrich, 98+%) were dissolved in distilled water with proper amount of citric acid. Glycine-nitrate process (GNP) can produce fine particle size produce gadolinium doped ceria (GDC, $Ce_{0.9}Gd_{0.1}O_{1.95}$) powder and NiO for electrodes and electrolyte. The solutions were heated up to 623 K in air and followed by combustion to form fine powders which were calcined at 873 K for 4 hours. For the measurement of electrical conductivity, the powders were pressed into pellets at 5 MPa and sintered in air at 1423 K for 12 h (to achieve relative density > 95%).

The structure and the morphology of the $La_xSr_{1-x}CoO_{3-\delta}$ were characterized by X-ray diffraction (XRD) and scanning electron microscopy (SEM). X-Ray powder diffraction measurements (Rigaku diffractometer, Cu Ka radiation) was performed to confirm the structure with a scan rate of 0.6o min-1 and a range $20^o < 2\theta < 60^o$. A thermogravimetric analysis (TGA) was carried out using a SDT-Q600 (TA instrument, USA). The TGA experiments were carried out from room temperature to 1173 K with a heating/cooling rate of 3 K min^{-1}. The room-temperature oxygen content values were determined by iodometric titration.

Electrical conductivities of the $La_xSr_{1-x}CoO_{3-\delta}$ cathode materials were determined in air using a four-electrode measurement. All four electrodes were made of Ag wire and Ag paste. The current and voltage were controlled/measured using a potentiostat (BioLogic) in the temperature range of 373 to 873 K with an interval of 50 K.

For symmetrical cells, two Ag wires were attached to each of the two electrodes using Ag paste. Each cell was mounted on an alumina tube using a ceramic adhesive (Aremco, Ceramabond 552). Impedance spectra were recorded under OCV in a frequency range of 1 mHz to 500 kHz with ac perturbation of 14 mV in the temperature range of 773-923 K.

For the single cell tests, each cell was mounted on an alumina tube using a ceramic adhesive. Humidified (with 3 vol % H_2O) H_2 was used as the fuel at a flow rate of 100 mL min^{-1} (passing through a water bubbler at room temperature), whereas ambient air was supplied to cathode as the oxidant. Impedance spectra and I-V polarization curves were obtained with a BioLogic Potentiostat. The I-V polarization curves were recorded between 773 K and 923 K.

Symmetrical cells are used for impedance researches and they are composed of electrode/GDC/electrode. For making cathode slurry, mix the LSC samples, GDC, and binder (Heraeus V006) in 3 : 2 : 6 weight ratio. Then, screen print the cathode slurry both side of sintered pellet surfaces and sintered at 1223 K for 4h. The silver wire and silver paste was used as a current collector for the electrodes. Impedance spectra were recorded under OCV in a frequency range of 1 mHz to 500 kHz with AC perturbation of 14 mV from 773 K to 923 K.

Ni-GDC anode support single cells are used to check electrochemical performances of cathode. The $La_xSr_{1-x}CoO_{3-\delta}$ powders and GDC are blended using ball-milling process during 24 h with 6:4 weight ratio to measure cell performance. The Ni-GDC anode is manufactured by nickel oxide, GDC powder, and starch mixture (weight ratio 6 : 4 : 2) and ball-milled with ethanol during 24 h. The GDC electrolyte layer is made by drop coating process on Ni-GDC cermet anode surface. The Ni-GDC/GDC anode-electrolyte layer is sintered at 1673 K for 5 h. The $La_xSr_{1-x}CoO_{3-\delta}$ slurries are used for cathode layer painted on the GDC electrolyte, with active cathode area of 0.36 cm2. The cells are sintered at 1223 K for 4 h under an air atmosphere. Ag wires are attached to both sides of single cells, anode and cathode, using Ag paste as current collector. An alumina tube is used to set the single cell using a ceramic adhesive (Aremco, Ceramabond 553). H_2 containing 3 % H_2O is applied through water bubbler with a flow rate of 20 mL min^{-1}, while air was employed as oxidant and flowing slowly to the cathode during the single cell test. A BioLogic Potentiostat is used to measure impedance spectra and I-V curves. Impedance spectra are measured under OCV in a frequency range of 1 mHz to 500 kHz with AC perturbation of 14 mV at 873 K, and I-V polarization curves are measured between 773 to 923 K.

5.3 Results and Discussions

The XRD patterns of $La_xSr_{1-x}CoO_{3-\delta}$ (x = 0.2, 0.3, 0.4, 0.5, 0.6 and 0.7) oxides sintered at 1423 K for 4 h are shown in Fig. 5.1 to confirm their crystal structure. XRD peaks of LSC28, LSC37, and LSC46 show a cubic perovskite structure without any impurity peaks. However, the other samples show a rhombohedral structure, as seen in the inset of Fig. 5.1. On this basis, we can predict that a phase transition boundary of the $La_xSr_{1-x}CoO_{3-\delta}$ oxide exists between x = 0.4 and 0.5.[28, 29]

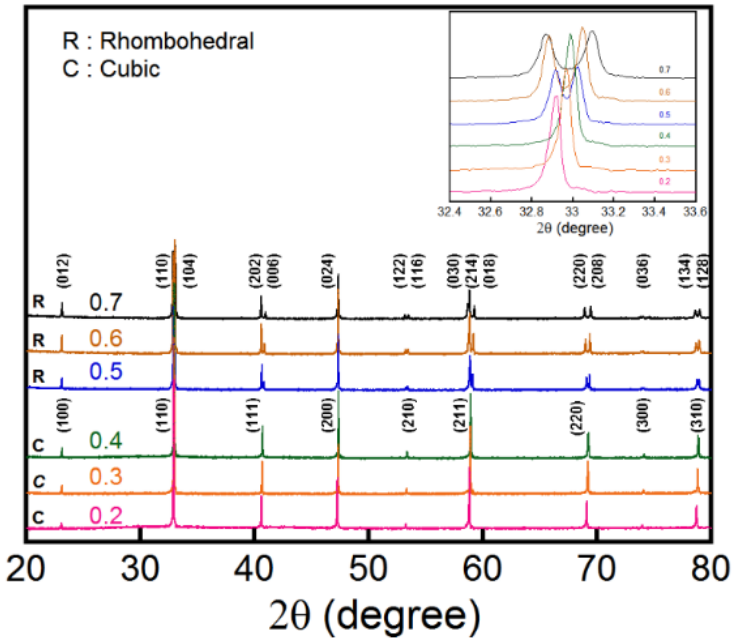

Figure 5.1 XRD pattern of $La_xSr_{1-x}CoO_{3-\delta}$ (x = 0.2, 0.3, 0.4, 0.5, 0.6, and 0.7) after sintering at 1423 K for 12 h. The inset shows the in-situ X-ray patterns of $La_xSr_{1-x}CoO_{3-\delta}$ (x = 0.2, 0.3, 0.4, 0.5, 0.6, and 0.7) in air at room temperature.

Figure 5.2 shows cross-sectional microstructure images of the $La_xSr_{1-x}CoO_{3-\delta}$ cathodes on a NiO-GDC anode support cell and the cathode morphology captured by SEM. The electrode microstructure captured by SEM is linked to the characteristics of the surface, the TPB area, the volume fraction of chemical phases present, and electron transport: these properties affect the fuel cell performance through the reaction kinetics, charge transport, and mass transport processes.[27, 28] The respective thickness of the electrolyte is about 15 μm, and there are no cracks or pores. The cathode layer has porous morphology that enhances oxygen diffusion and its thickness is about 15 μm as seen in Fig. 5.2(a). The $La_xSr_{1-x}CoO_{3-\delta}$ oxides have good adhesion with the GDC electrolyte, which is expected to enhance the thermal compatibility and the long-term thermal stability of the cathode/electrolyte interface. The microstructures of all $La_xSr_{1-x}CoO_{3-\delta}$ samples are similar, showing that the microstructure is apparently insensitive to lanthanum substitution.

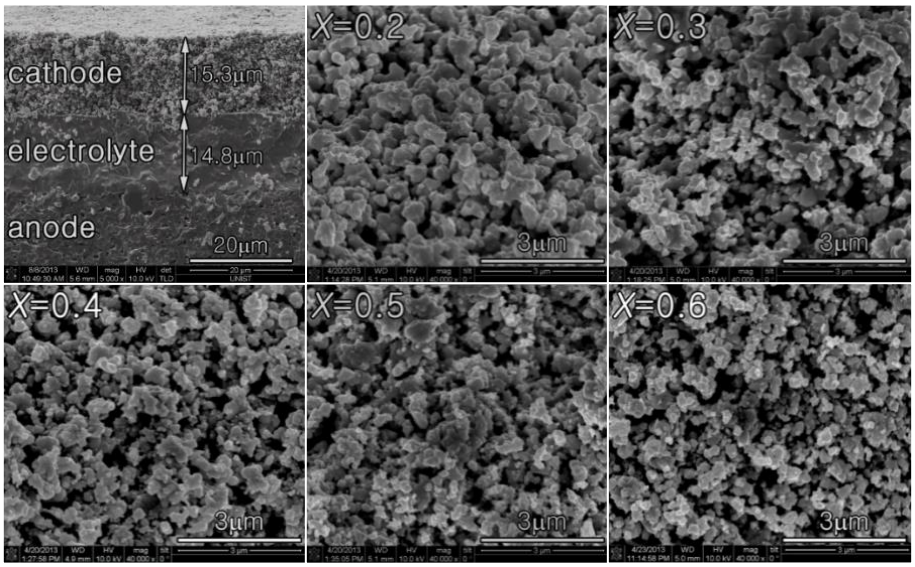

Figure 5.2 Scanning electron micrographs of the cross-sectional view with a tri-layer single cell (Ni-GDC/GDC/ $La_xSr_{1-x}CoO_{3-\delta}$-GDC) and each $La_xSr_{1-x}CoO_{3-\delta}$ oxide sample (x = 0.2, 0.3, 0.4, 0.5, and 0.6).

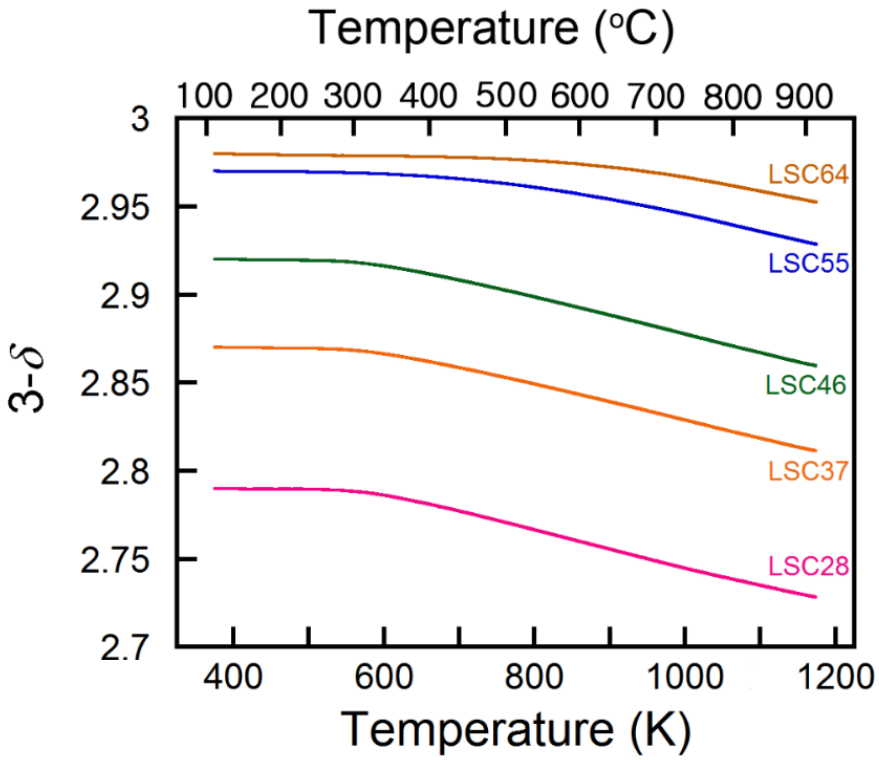

Figure 5.3 Variation of oxygen content in $La_xSr_{1-x}CoO_{3-\delta}$ (x = 0.2, 0.3, 0.4, 0.5, and 0.6) as a function of temperature in air.

Thermogravimetric analysis (TGA) data describing the weight change and oxygen-content of $La_xSr_{1-x}CoO_{3-\delta}$ oxides upon heating to 1173 K in air are shown in Fig. 5.3. Weight changes of all LSC samples started at around 573 K due to the release of lattice oxygen, with a weight loss of 0.92~2.21% from room temperature to 1173 K. Initial oxygen content determined by iodometric titration at room temperature increases with higher concentration of lanthanum.

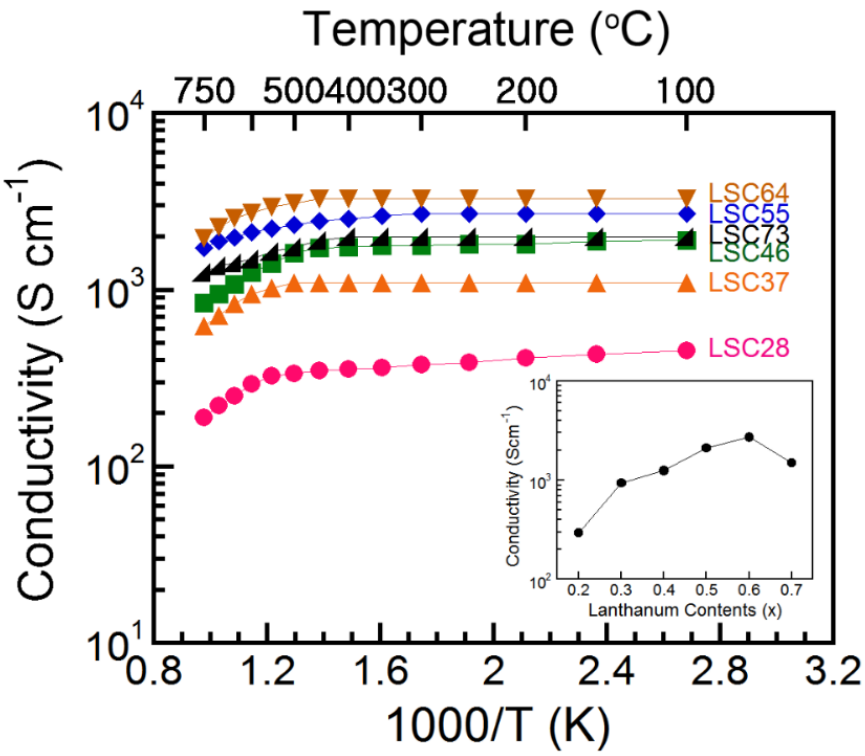

Figure 5.4 The electrical conductivity data for $La_xSr_{1-x}CoO_{3-\delta}$ (x = 0.2, 0.3, 0.4, 0.5, 0.6, and 0.7) as a function of temperature in air. The electrical conductivities of $La_xSr_{1-x}CoO_{3-\delta}$ (x = 0.2, 0.3, 0.4, 0.5, 0.6, and 0.7) are presented as a function of lanthanum content at 873 K in the inset.

The electrical conductivity of the $La_xSr_{1-x}CoO_{3-\delta}$ cathodes is presented in a temperature range of 373~1023 K in air, as seen in Fig. 5.4. Electrical conductivities decrease as temperature increases, and this is evidence that $La_xSr_{1-x}CoO_{3-\delta}$ has metallic-like behavior. The higher electrical conductivity with increasing lanthanum content can be explained by the ionic size of lanthanum. The large ionic size of lanthanum compared to other lanthanides makes higher electronic conductivity possible due to straightening of the Co-O-Co bonds to 180°, larger bandwidth, and larger covalency of the Co-O bonds.[17, 18] The amount of oxygen content in LSCs increases by La doping as shown in TGA experiment, which also affects the electrical conductivity behavior.

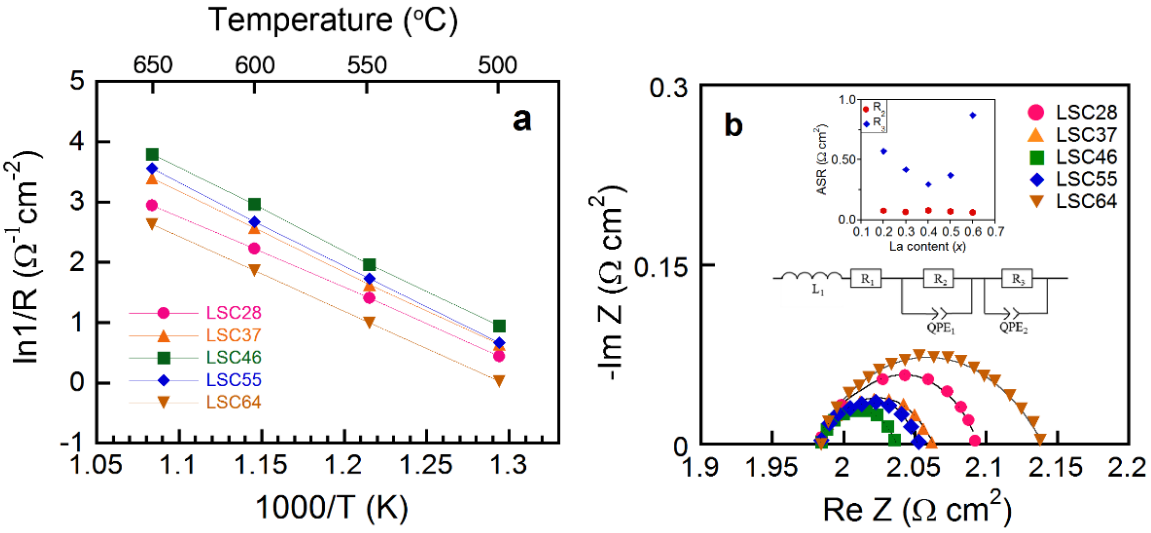

Figure 5.5 (a) Arrhenius plot of the area specific resistance for $La_xSr_{1-x}CoO_{3-\delta}$-GDC ($x$ = 0.2, 0.3, 0.4, 0.5, and 0.6) at various temperatures. (b) Impedance spectra and fitted Nyquist plots with a $La_xSr_{1-x}CoO_{3-\delta}$-GDC ($x$ = 0.2, 0.3, 0.4, 0.5, and 0.6) cathode measured under an open-circuit condition at 873 K in air. The fitting parameters (R_2 and R_3) are indicated as a function of lanthanum content in the inset of Fig. 5.5(b).

Cathode reaction includes reduction of molecular oxygen to oxygen ions, gas diffusion, surface adsorption, dissociation, charge transfer. The surface exchange and oxygen diffusion properties are key factors to understand the electrochemical properties of the cathode, as well as to suggest a direction for performance measurements. GDC enhance the electrocatalytic activity by supplying additional triple phase boundary (TPB) sites of the cathode where the electrochemical reaction occurs.[30, 31] In this regard, the impedance spectra for symmetric cells (LSC-GDC|GDC|LSC-GDC) are obtained in order to clarify electrocatalytic activity for the ORR by AC impedance spectroscopy at various temperatures in air. An Arrhenius plot of the area specific resistance (ASR) for $La_xSr_{1-x}CoO_{3-\delta}$ is shown in Fig. 5.5(a) and it shows the points of ASR scanned at every 50 K from 923 K to 773 K for the $La_xSr_{1-x}CoO_{3-\delta}$ (x = 0.2, 0.3, 0.4, 0.5, and 0.6) samples.

The ASR of LSC46-GDC shows the lowest value, 0.052 Ω cm^2 at 873 K, and this is the best value among the LSC oxides in this study. The impedance spectra for symmetric cells (LSC-GDC/GDC/LSC-GDC) by AC impedance spectroscopy with various temperatures in air are shown in Fig. 5.5(b). The impedance spectra are fitted to the equivalent circuit. The fitting parameters (R_2 and R_3) are presented as a function of La content in the inset of Fig. 5.5(b). Based on the literature, the high and intermediate frequency behavior of impedance (R_2) is related to ion and electron transfer at the electrode, electrolyte, and collector/electrode interfaces, while the low frequency behavior of

impedance, R_3, is associated with non-charge transfer, such as oxygen surface exchange and gas-phase diffusion inside and outside the electrode layer.[32-34] From these results, R_3 with an increase of La content from x = 0.2 to 0.6 shows a more considerable change than R_2 in the $La_xSr_{1-x}CoO_{3-\delta}$ cathode, mainly due to the lower oxygen diffusion rate caused by the distortion of the structure from cubic to rhombohedral.[35]

I-V curves and corresponding power density curves of $La_xSr_{1-x}CoO_{3-\delta}$ with an Ni-GDC anode supported single cell in a temperature range of 773 to 923 K using humidified H_2 (3 % H_2O) as a fuel and static ambient air as an oxidant are presented in Fig. 5.6. The crystal structure is an important factor with respect to the electrochemical performance of $La_xSr_{1-x}CoO_{3-\delta}$ oxides. The electrochemical performance of LSCs improves until x = 0.4, whereas it falls after x = 0.4, which appears to be mainly due to the structural change to rhombohedral from cubic. At $x \leq 0.5$, $La_xSr_{1-x}CoO_{3-\delta}$ retains the cubic structure; however, above x = 0.5, $La_xSr_{1-x}CoO_{3-\delta}$ oxides structures are changed to rhombohedral structures. The rhombohedral structure is a kind of distorted cubic structure, and disordered oxygen diffusion paths lead to degradation of ionic conductivities and performance.[35] The maximum power density is 1.58 W cm^{-2} for x = 0.4, and the other samples also show excellent power density: 1.40 and 1.34 W cm^{-2} for x = 0.2 and 0.6, respectively, at 873 K. The optimized maximum power density of LSC46 can be explained by a combined effect of enhanced electrical conductivity according to the lanthanum doping and high ionic conductivity originating from the ordered oxygen diffusion paths with the stable cubic perovskite structure.

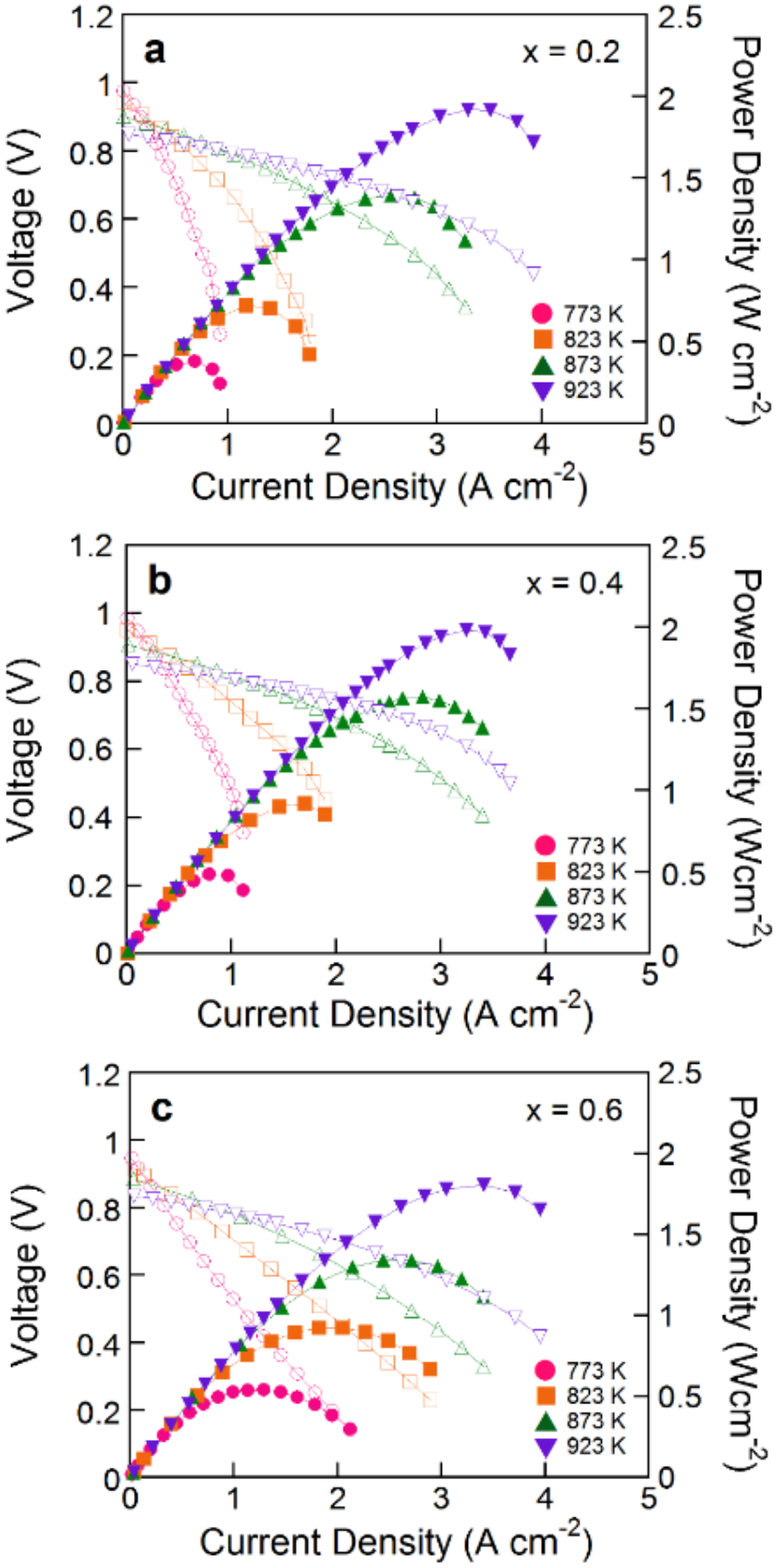

Figure 5.6 I-V curves and corresponding power density curves of single cell (Ni-GDC/GDC/$La_xSr_{1-x}CoO_{3-\delta}$-GDC ($x$ = 0.2, 0.4, and 0.6)) at various temperatures.

5.4 Conclusion

Lanthanide doped $SrCoO_{3-\delta}$ oxides, $Ln_xSr_{1-x}CoO_{3-\delta}$ (Ln = La, Pr, Nd, Sm, and Gd), have been extensively investigated on the basis of their good ionic and electronic conductivity and high performance as IT-SOFC cathode materials. However, there was no systematic study in the cell performance with regard to the amount of La so far. In this study, we systematically investigated the effects of La in $La_xSr_{1-x}CoO_{3-\delta}$ cathodes on the structure, electrical properties, and electrochemical performance.

The electrical conductivities of $La_xSr_{1-x}CoO_{3-\delta}$ in air increase according to the amount of lanthanum content because of the large ionic size of lanthanum among the lanthanides, possibly due to straightening of the Co-O-Co bonds and large bandwidth. The ASR with GDC symmetrical cells decreased with lanthanum doping in $La_xSr_{1-x}CoO_{3-\delta}$-GDC cathodes. The ASR value of LSCs after x = 0.4, however, increased, possibly due to a structural change from perovskite to a rhombohedral structure. The electrochemical performance of in $La_xSr_{1-x}CoO_{3-\delta}$-GDC cathodes was evaluated using an anode-supported cell based on a GDC electrolyte with humidified H_2 (3 % H_2O). The maximum power density was 1.58 W cm^{-2} for x = 0.4 at 873 K. The other samples also show good performance of 1.40 and 1.34 W cm^{-2} for x = 0.2 and 0.6, respectively. The maximum power density for x = 0.4 might be explained by the high electrical conductivity, fast oxygen transport in the bulk and surface, and high catalytic activity for the ORR with a cubic perovskite crystal structure. Therefore, LSC46-GDC is the most suitable cathode candidate material for IT-SOFCs in terms of electrochemical performance.

References

1. Z. Shao, S. M. Haile, J. Ahn, P. D. Ronney, Z. Zhan, S. A. Barnett, Nature. 2005, 435, 795–8.

2. A. J. Jacobson, Chem. Mater. 2010, 22, 660–74.

3. B. C. H. Steele, A. Heinzel, Nature. 2001, 414, 345–52.

4. S. Park, J. M. Vohs, R. J. Gorte, Nature. 2000, 404, 265–7.

5. S. Choi, J. Shin, G. Kim, J. Power Sources. 2012, 201, 10–7.

6. T. Hibino, A. Hashimoto, T. Inoue, J. -I. Tokuno, S. -I. Yoshida, M. Sano, Science. 2000, 288, 2031–3.

7. S. Choi, S. Yoo, J. Kim, S. Park, A. Jun, S. Sengodan, J. Kim, J. Shin, H. Y. Jeong, Y. Choi, G. Kim, Sci. Rep. 2013, 3, 2426.

8. T. V. Aksenova, L. Y. Gavrilova, A. A. Yaremchenko, V. A. Cherepanov, V. V. Kharton, Mater. Res. Bull. 2010, 45, 1288–92.

9. W. Zhou, R. Ran, Z. Shao, J. Power Sources. 2009, 192, 231–46.

10. J. Peña-Martínez, D. Marrero-López, D. Pérez-Coll, J. C. Ruiz-Morales, P. Núñez, Electrochim. Acta. 2007, 52, 2950–8.

11. J. Wan, J. B. Goodenough, J. H. Zhu, Solid State Ionics. 2007, 178, 281–6.

12. Z. Shao, S. M. Haile, Nature. 2004, 431, 170–3.

13. J. M. Ralph, C. Rossignol, R. Kumar, J. Electrochem. Soc. 2003, 150, A1518-22.

14. T. Nagai, W. Ito, T. Sakon, Solid State Ionics. 2007, 177, 3433–44.

15. P. Shen, X. Liu, H. Wang, W. Ding, J. Phys. Chem. C. 2010, 114, 22338–45.

16. Z. Yang, C. Yang, C. Jin, M. Han, F. Chen, Electrochem. Commun. 2011, 13, 882–5.

17. K. T. Lee, A. Manthiram, J. Electrochem. Soc. 2005, 152, A197-204.

18. K. T. Lee, A. Manthiram, J. Electrochem. Soc. 2006, 153, A794-8.

19. S. Yoo, T. -H. Lim, J. Shin, G. Kim, J. Power Sources. 2013, 226, 1–7.

20. Y. Guo, H. Shi, R. Ran, Z. Shao, Int. J. Hydrogen Energy. 2009, 34, 9496–504.

21. S. -W. Baek, J. Bae, Y. -S. Yoo, J. Power Sources. 2009, 193, 431–40.

22. M. Koyama, C. Wen, T. Masuyama, J. Otomo, H. Fukunaga, K. Yamada, K. Eguchi, H. Takashi, J. Electrochem. Soc. 2001, 148, A795-801.

23. Y. L. Yang, C. L. Chen, S. Y. Chen, C. W. Chu, A. J. Jacobson, J. Electrochem. Soc. 2000, 147, 4001–7.

24. S. B. Adler, J. A. Lane, B. C. H. Steele, J. Electrochem. Soc. 1996, 143, 3554–64.

25. S. Wang, J. Yoon, G. Kim, D. Huang, H. Wang, A. J. Jacobson, Chem. Mater. 2010, 22, 776–82.

26. J. M. Ralph, A. C. Schoeler, M. Krumpelt, J. Mater. Sci. 2001, 6, 1161–72.

27. R. Doshi, V. L. Richards, J. D. Carter, X. Wang, M. Krumpelt, J. Electrochem. Soc. 1999, 146, 1273–8.

28. A. N. Petrov, O. F. Kononchuk, A. V. Andreev, V. A. Cherepanov, P. Kofstad, Solid State Ionics. 1995, 80, 189-99.

29. N. M. L. N. P. Closset, R. H. E. van Doorn, H. Kruidhof, J. Boeijsma, Powder diffraction. 1996, 11, 31-4.

30. Y. Leng, S. W. Chan, Q. Liu, Int. J. Hydrogen Energy. 2008, 33, 3808–17.

31. J. Kim, W. -Y. Seo, J. Shin, M. Liu, G. Kim, J. Mater. Chem. A. 2013, 1, 515-9.

32. A. Jun, J. Kim, J. Shin, G. Kim, Int. J. Hydrogen Energy. 2012, 37, 18381–8.

33. S. Park, S. Choi, J. Shin, G. Kim, J. Power Sources. 2012, 210, 172–7.

34. S. B. Adler, X. Y. Chen, J. R. Wilson, J. Catal. 2007, 245, 91–109.

35. Y. -C. Chen, M. Yashima, T. Ohta, K. Ohoyama, S. Yamamoto, J. Phys. Chem. C. 2012, 116, 5246-54.

Chapter VI. An Efficient Oxygen Evolution Catalyst for Hybrid Lithium Air Batteries: Almond Stick Type Composite of Perovskite and Cobalt Oxide

Reprinted with permission from J. Electrochem. Soc., 163, A1893-A1897 (2016). Copyright 2016, The Electrochemical Society.

6.1 Introduction

High efficiency, eco-friendliness, and low cost are substantial factors for developing energy conversion and storage systems such as water splitting, electrolysis cells, fuel cells, metal−air batteries, and solar synthetic reactors. In order to build highly efficient energy conversion and storage devices, improved catalytic activity for oxygen reduction and evolution reactions (ORR and OER) is the most important feature.[1-5] The ideal ORR and OER in an alkaline solution involve a four-electron transfer pathway described by equation (1).

$$O_2 + 4e^- + 2\,H_2O \rightleftarrows 4\,OH^- \qquad (n = 4) \qquad (1)$$

In contrast, a two-electron transfer pathway is partly responsible for the ORR current; does not complete a turnover of the ORR but generates peroxide as an intermediate product. [6-11]

$$O_2 + 2e^- + 2\,H_2O \rightarrow HO_2^- + OH^- \qquad (n = 2) \qquad (2)$$

For a high oxygen redox, precious-metal-based materials such as platinum (Pt), iridium oxide (IrO_2), and ruthenium oxide (RuO_2) are commonly used as electro-catalysts due to their high catalytic activity. Even though these catalysts show superior electrochemical properties, their commercial application is very limited by their high cost, scarcity of resources, and the absence of bifunctional catalytic reactivity.[12-14] Additionally, the noble metal catalysts require a high conducting support material for electron path. Carbon materials, such as Ketjen Black (KB), Vulcan XC-72R, Super-P Black (SPB), etc. are normally used for the support because of their low cost, easy production, high conduction, and acceptable performance. However, their low electron transfer numbers (n) generate large amounts of HO_2^- oxidants that induce oxidation/corrosion of carbon supports, resulting in an increase of charge/discharge overpotential.[15-19] In addition, Li_2CO_3 generated from the reaction between carbon and intermediate products (Li_2O_2) during the discharge process gives rise to an increase of resistance and decay of the cycling performance of rechargeable solid-state Li–air batteries.[20] To overcome the drawbacks of both precious metals and carbon materials, it is necessary to develop a precious metal and carbon free catalyst material.

Recently, a number of groups have attempted to develop inexpensive and high-performing metal electro-catalysts based on transition-metal oxide materials, especially oxides containing cobalt.[21-25] Dai et al. showed that cobalt oxides are synergistic catalysts having high efficiency for the OER.[1] Shao-Horn et al. reported several perovskites that exhibited high performance for both ORR and OER. Among them, Co-containing perovskite oxides, such as $Nd_{1-x}Sr_xCoO_{3-\delta}$ (NSC), $La_xSr_{1-x}CoO_{3-\delta}$, and $Ba_xSr_{1-x}Co_yFe_{1-y}O_{3-\delta}$, have received attention due to their good catalytic activities for the ORR and OER, cyclic stability, and the capability of simultaneous oxygen ionic and electronic conduction.[26-31] Normally, A-site deficiency or B-site excess perovskite oxides are formed as a single phase with a solid state or combustion process when a nonstoichiometric precursor is used.[32, 33] Interestingly, however, we successfully synthesized a double phases Co_3O_4 and NSC composite via a new synthesis process rather than single phase of Co excess $Nd_{0.5}Sr_{0.5}Co_{1.1}O_{3-\delta}$ perovskite in this study. The Co_3O_4 and NSC composite (Co-NSC) is synthesized via an electrospinning process with a nonstoichiometric stock solution. The stoichiometric NSC is also synthesized and compared in order to identify the effect of the composite on microstructure and electrochemical properties. Herein, we investigate the electrochemical effect of the cobalt oxide and perovskite composite electrocatalysts fabricated via an electrospinning process compared with state-of-the-art catalysts and performed in a hybrid lithium air battery.

6.2 Experimental

6.2.1 Material Preparation

An electrospinning process was adopted to prepare NSC and Co-NSC powders. A 0.01 M NSC (Nd : Sr : Co = 1 : 1 : 2) and Co-NSC (Nd : Sr : Co = 1 : 1 : 2.2) precursor solution was prepared with $Nd(NO_3)_3 \cdot 6H_2O$ (Aldrich, 99.9%, metal basis), $Sr(NO_3)_2$ (Aldrich, 99+%), and $Co(NO_3)_2 \cdot 6H_2O$ (Aldrich, 98+%) in N,N-Dimethylformamide (DMF, 99.5%, Aldrich Chemical Co.) solvent. The precursor solution was mixed with 15 wt. % PVP (Polyvinylpyrrolidone, Mw = 1,300,000, Aldrich Chemical Co.)

A power supply (Korea Switching, Korea) with variable high voltage was used for the electrospinning process. A composite solution was placed in a 30 ml syringe with a positively charged capillary tip with a diameter of 0.5 mm. The anode of the high-voltage power supply was clamped to a syringe needle tip and the cathode was connected to a metal collector. The electrospun composite fiber was collected by attaching it to aluminium foil wrapped on a metal collector. The applied voltage was 9 kV, the distance between the syringe needle tip and collector was 11 cm, and the flow rate of the solution was 0.5 ml h^{-1}. The electrospun webs were dried by heating them at 80 ºC for 1 h in an air atmosphere and separated from the aluminium foil. After that, the dried webs were sintered at 850 ºC for 4 h in an air atmosphere. The heating rate was 2 ºC min^{-1}.

6.2.2 Crystallography Characterization

The crystallographic structures of the materials were characterized at a scan rate of 0.6 º min^{-1} with a 2θ range of 20 º to 60 º by X-ray diffraction (XRD, D8 Advance, Bruker diffractometer with Cu Kα radiation). Scanning electron microscopy (SEM, Nanonova 230, FEI) was used to capture their morphologies. Transmission electron microscopy (TEM) images were obtained using a High Resolution-TEM (JEOL, JEM-2100F).

6.2.3 Electrochemical characterization

X-ray photoelectron spectroscopy (XPS) analyses were performed on ESCALAB 250XI from Thermo Fisher Scientific with a monochromated Al-Kα (ultraviolet He1, He2) X-ray source. The base pressure inside the spectrometer during analysis was 1 x 10^{-10} mmHg.

Catalyst inks were prepared by dispersing 20mg of catalyst in 0.45 ml of ethanol, 0.45 ml of isopropyl alcohol, and 0.1 ml of 5 wt. % Nafion solution (Sigma-Aldrich 274704). The loading density of the catalyst was fixed at 0.8 mg cm^{-2} (disk electrode area = 0.1256 cm^2). For comparison, Pt/C (Alfa Aesar 35849) and IrO_2 (Alfa Aesar 43396) were used as controls.

Cyclic and linear sweep voltammetries (CVs and LSVs) were measured on disk and ring electrodes simultaneously by a computer-controlled potentiostat (Biologic, VMP3) with 1600 rpm controlled by

a rotating disk electrode system (Biologic, RRDE-3A). A platinum wire and an Hg/HgO electrode (Hg/HgO vs. NHE is 0.140 V (NaOH, 1 M)) were used as the counter and reference electrodes, respectively. An aqueous solution of 0.1M KOH was used as the electrolyte. ORR polarization curves were obtained on the disk electrode from a cathodic sweep from 0.1 V to -0.9 V (vs. Hg/HgO) at 10 mV s^{-1} after several cycles of CVs. Voltage of 0.4 V was applied to the ring electrode to estimate the amount of peroxide generated from the disk electrode. The anodic sweeps from 0.35 V to 0.9 V (vs. Hg/HgO) were presented as OER polarization curves. The other conditions were the same as those applied for the ORR polarization curves. To demonstrate the stability of OER, anodic and cathodic sweeps were repeated at 10 mV s^{-1} for 100 cycles.

6.2.4 Preparation and assembly of a hybrid Li-air battery

A lithium foil with a thickness of 0.2 mm was obtained from Honjo Metal, and disks with a diameter of 1 cm were cut for use as the anode. 1 M lithium hexafluorophosphate ($LiPF_6$, Sigma-Aldrich Co.) in tetraethylene glycol dimethyl ether (TEGDME, Sigma-Aldrich Co.) was used as an organic liquid electrolyte, and 0.1 M lithium hydroxide (LiOH, Sigma-Aldrich Co.) in pure water was used as the aqueous liquid electrolyte. The anode and cathode were separated by a $Li_{1+x+y}Ti_{2-x}Al_xP_{3-y}Si_yO_{12}$ (0.15 mm thickness, OHARA Inc., Japan) solid Li-ion conducting ceramic glass. The air electrodes were prepared by spraying the catalyst ink made with the prepared catalysts, carbon (catalyst:carbon = 4:1 wt. ratio) and PVdF-HFP binder (Sigma-Aldrich Co.) onto the gas-diffusion layer (Toray TGP-H-090). The catalyst loading density and binder content in the air electrode were 1 mg cm^{-2} (air electrode area = 0.78 cm^2) and 20 wt. %, respectively. Thus, the current density could be easily normalized with the loading density of the catalyst (0.8 mg cm^{-2}). Details of the tested hybrid Li-air battery are available on the electronic supplementary information.

6.3 Results and Discussions

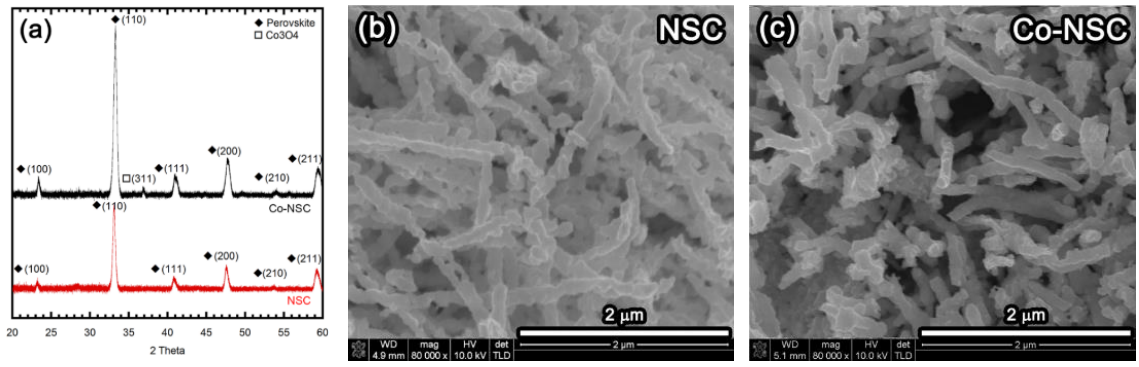

Figure 6.1 (a) X-Ray Diffraction (XRD) pattern of Co-NSC and NSC after sintering at 850 ºC for 4 h. (b), (c) Scanning electron micrographs (SEM) of NSC and Co-NSC composite.

XRD was performed to confirm the crystal structure of NSC and Co-NSC in Fig. 6.1(a), indicating that both samples show typical cubic perovskite peaks except the Co_3O_4 peak of the (311) plane at around 37º for the Co-NSC. The microstructure of each sample is similarly characterized by homogenous 150 nm thick fibers (Fig. 6.1(b) and (c)), indicating it is insensitive to the Co_3O_4 phase. Therefore, TEM was used to observe the difference in grain morphology and elements in more detail in Fig. 6.2.

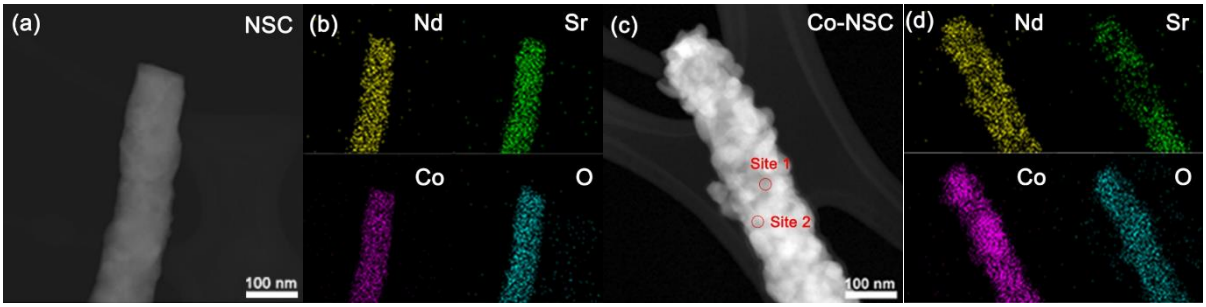

Figure 6.2 Transmission electron microscopy (TEM) analysis & Energy dispersive spectroscopy (EDS) elemental mapping of the NSC particles. High-angle annular dark-field (HAADF) TEM image obtained from the (a) NSC and (c) Co-NSC composite. Elemental mapping of Nd, Sr, Co, and O, respectively in (b) and (d).

For NSC fibers, a homogenous smooth surface and well distributed elements are seen in Fig. 6.2(a) and (b) from a high-angle annular dark-field (HAADF) TEM image. In contrast, the Co-NSC composite shows a rough surface with lumps of small grains (Fig. 6.2(c)) and bright-field TEM supports the unique microstructure more clearly (Fig. 6.3). To confirm the accurate atomic ratio of

each Co-NSC grain, marked sites 1 and 2 are identified (Fig. 6.2(c)) and details of each atomic ratio are specified in Table 6.1. According to the EDS results (Fig. 6.2(d)) and details of the atomic ratio at the marked sites, it is confirmed that the grains of the Co-NSC consist of NSC and Co_3O_4. The cobalt oxides and NSC exist separately and are uniformly distributed in the Co-NSC composite.

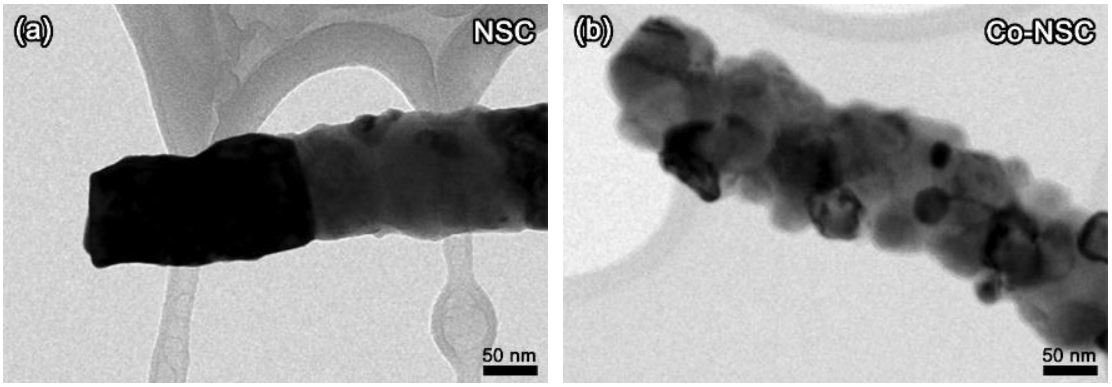

Figure 6.3 Bright-field (BF) TEM image obtained from the (a) NSC and (b) Co-NSC samples.

Table 6.1 Atomic ratio at various sites in the Co-NSC sample.

Elements	Atomic ratio (%)	
	Site 1	Site 2
Nd	12.38	3.36
Sr	7.64	0.00
Co	18.34	39.61
O	61.65	57.03
Total	100.00	100.00

Rotating ring-disk electrode (RRDE) measurements were carried out to check the ORR and OER catalytic activity of the NSC and Co-NSC composite in Fig. 6.4 and Fig. 6.5. The disc current for the ORR of the NSC and Co-NSC catalysts is shown and compared with that of a commercial Pt/C catalyst (Fig. 6.4(a)). The ORR onset potential of the NSC and Co-NSC was -0.2 V (vs Hg/HgO) at -0.1 mA cm^{-2} which is lower than that of Pt/C (0.089 V vs Hg/HgO). Interestingly, the current density of the Co-NSC composite is comparable with that of Pt/C at high voltage. For more information, ring currents of samples are shown in Fig. 6.4(b) to calculate the number of transferred electrons in Fig. 6.4(c) and the percentage of peroxide species (HO_2^-) in Fig. 6.4(d).

The number of transferred electrons (n) shown in Fig. 6.4(c) was calculated by equation (3),

$$n = 4 \times \frac{I_d}{I_d + I_r/N} \qquad (3)$$

where I_d and I_r are the disc current and ring current, respectively, with the experimentally determined collection efficiency (N) of 0.41. The calculated number of transferred electrons of the Co-NSC catalyst was about 3.9, which is close to the number of electrons involved in the ideal ORR, 4.

The percentage of peroxide species (HO_2^-) during the ORR process is shown in Fig. 6.4(d). Hydrogen peroxide yields were calculated by the following equation,

$$HO_2^-(\%) = 200 \times \frac{I_r/N}{I_d + I_r/N} \qquad (4)$$

The measured HO_2^- yields are below 9% for NSC and below 5% for Co-NSC over a potential range of -0.4 to -0.9 V.[34] To investigate the electrocatalytic activity of the catalysts for OER, LSV was performed with NSC, the Co-NSC composite and commercial IrO_2 measured in a 0.1 M KOH solution with a scan rate of 10 mV s^{-1}.

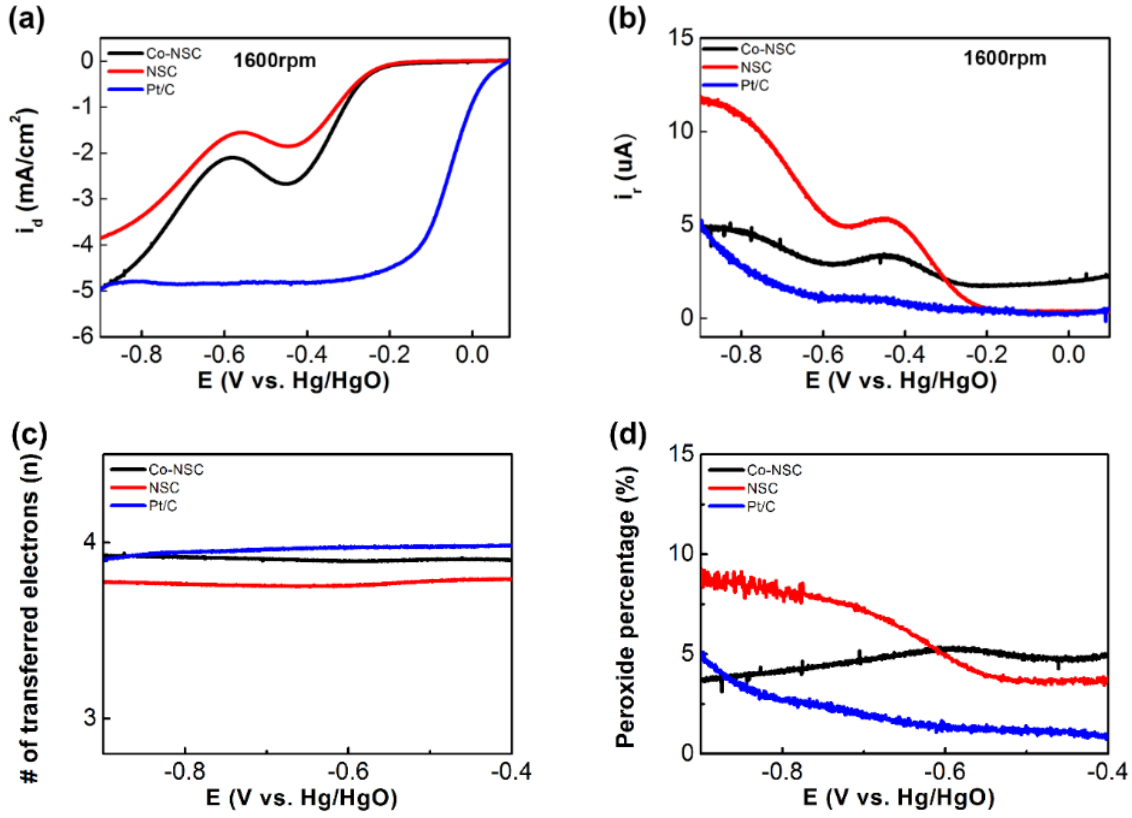

Figure 6.4 (a) Disc current, (b) ring current, (c) number of transferred electrons, and (d) peroxide percentage of ORR are measured by a RRDE test. The test is operated with a 10 mV s^{-1} scan rate from 0.1 V to -0.9 V.

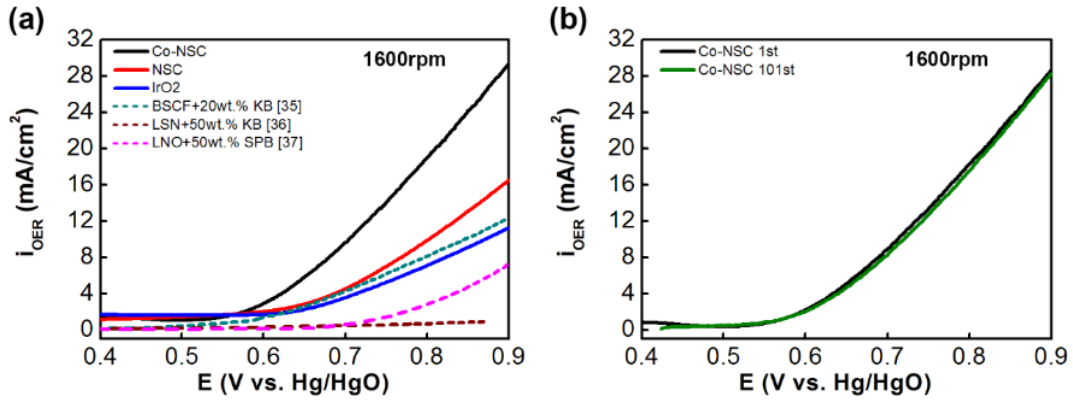

Figure 6.5 (a) Disc currents of NSC and Co-NSC are compared with BSCF35, LSN36, LNO37, and IrO_2 and (b) cyclic performances of OER are measured by a RRDE test. The test is operated with a 10 mV s^{-1} scan rate and 1600 rpm rotating rate from 0.35 V to 0.9 V.

The OER onset potential of Co-NSC (0.576 V) was better than that of the best OER catalyst to date such as $Ba_{0.5}Sr_{0.5}Co_{0.8}Fe_{0.2}O_{3-\delta}$ (BSCF, 0.629 V), $La_{1.7}Sr_{0.3}NiO_4$ (LSN, 0.629 V), $LaNiO_3$ (LNO, 0.730 V) and IrO_2 (0.636 V) at 2.0 mA cm^{-2} as shown in Fig. 6.5(a). [35-37] It is worth noting that conducting carbon agents were added into those compared catalysts for the electrode optimization. In contrast, the Co-NSC composite in this study, there is not any additional conducting agents, such as KB, and SPB, which might cause cell degradation from the formation of undesired by-products.

These RRDE results confirm the outstanding improvement of the catalytic activity is mainly attributed to the Co_3O_4 oxide with NSC perovskite. In order to assess the cyclic stability, a cyclic test was conducted with cyclic voltammetry (CV) with a 10 mV s^{-1} scan rate for 100 cycles. As shown in Fig. 6.5(b), excellent cyclic stability of the Co-NSC composite was observed.

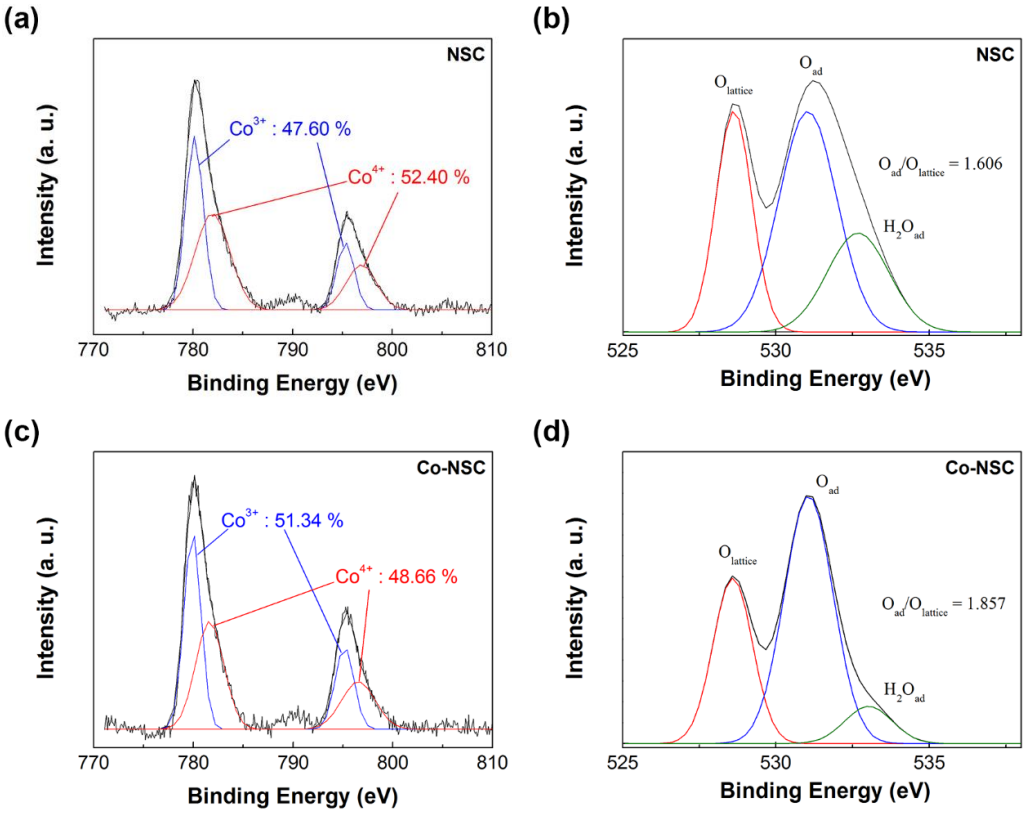

Figure 6.6 XPS spectra of (a) Cobalt 2p orbital and (b) Oxygen 1s orbital of NSC. XPS spectra of (c) Cobalt 2p orbital and (d) Oxygen 1s orbital of Co-NSC composite.

To identify the reasons for the excellent catalytic activity of Co-NSC, bonding states of the cobalt in the NSC and Co-NSC oxides were further characterized by X-ray photoelectron spectroscopy (XPS) measurements as shown in Fig. 6.6. For the Co 2p spectra of the NSC (Fig. 6.6(a)) and Co-NSC (Fig. 6.6(c)), the main peaks are located at binding energy of about 780.1 eV (at Co $2p_{3/2}$) and 796.6 eV (at Co $2p_{1/2}$). A weak satellite shoulder also appeared at 789.6 eV which indicates the existence of low spin Co(III) on the oxide surfaces.[38] The low spin Co with a binding energy of ca. 780.1 eV is attributed to octahedral Co^{3+} cations.[39] Considering the intensity of the peaks, the additional cobalt in Co-NSC causes an increase of Co^{3+} cations (from 46.93% to 51.98%). According to previous study, Co^{3+} cations at the cobalt oxide surface were related with the catalytic active sites. These Co^{3+} cations act as donor–acceptor reduction sites, with a donor electronic property with respect to O_2 and an acceptor character involved with Co_3O_4 by capturing electrons.[40] Figure 6.6(b) and (d) show the XPS spectra of the O 1s core levels obtained from the NSC and Co-NSC samples, respectively. Oxygen could exist in the NSC and Co-NSC catalysts in three forms, as reported in the literature.[41, 42] The O 1s peak at 528 eV can be assigned to lattice oxygen ($O_{lattice}$). The peak at 531.4–531.9 eV is usually related to adsorbed oxygen species (O_{ad}), including O^-, O^{2-}, and OH^-, which are believed to be

adsorbed mainly on lattice oxygen vacancy sites. The peak at around 533 eV is attributed to H_2O molecules adsorbed on the material surface. The Co-NSC possesses a high concentration of adsorbed oxygen species (O_{ad}), as indicated by the calculated $O_{ad}/O_{lattice}$ ratio (1.857) compared with that of NSC (1.606). Adsorbed oxygen species are weakly bonded to the crystal lattice and can be easily released as molecular oxygen. From the XPS analysis, it has been confirmed that the good catalytic activity of Co-NSC originated from the higher amount of Co^{3+} cations and higher $O_{ad}/O_{lattice}$ ratio.

The electrochemical performance of Co-NSC was evaluated with a hybrid Li-air battery and compared with that of Pt/C.[43-46] Figure 6.7(a) shows the first discharge-charge curves of Pt/C and Co-NSC in 0.1 M LiOH at a current density of 0.5 mA cm^{-2}. The discharge and charge voltage plateaus of Co-NSC are obtained at 2.94 and 3.96 V versus Li/Li^+, respectively (3.10 and 4.21 V versus Li/Li^+ for Pt/C). Additional discharge and charge profiles are investigated at higher current density in a range of 0.5 to 2.0 mA cm^{-2} (Fig. 6.7(b)). At 0.5 mA cm^{-2}, the discharge voltage of Co-NSC is only 0.16 V lower than that of Pt/C. However, the charge voltage of Co-NSC at 0.5 mA cm^{-2} is 0.28 V lower than that of Pt/C, which indicates lower overpotential during the charge process. Even at a higher current density of 2.0 mA cm^{-2}, the difference in the charge voltage between Co-NSC and Pt/C increases to 0.33 V. These results demonstrate that the Co-NSC catalyst is comparable to Pt/C even at the high current density region. Figure 6.7(c) presents the cycling performance of Pt/C and Co-NSC at a constant current density of 0.1 mA cm^{-2} in ambient air. Pt/C shows obvious degradation during 20 h with a substantial increase in the discharge-charge voltage gap from 1.18 V to 1.64 V. This result is consistent with the vulnerability of Pt/C during the ORR and OER process. In the case of Co-NSC, in contrast, outstanding cycling performance was obtained during 20 h with the lowest discharge-charge voltage gap (less than 1.0 V). Co-NSC is thus an efficient bifunctional catalyst with comparable performance to noble metal-based catalysts, such as Pt/C and IrO_2 for hybrid Li-air batteries.

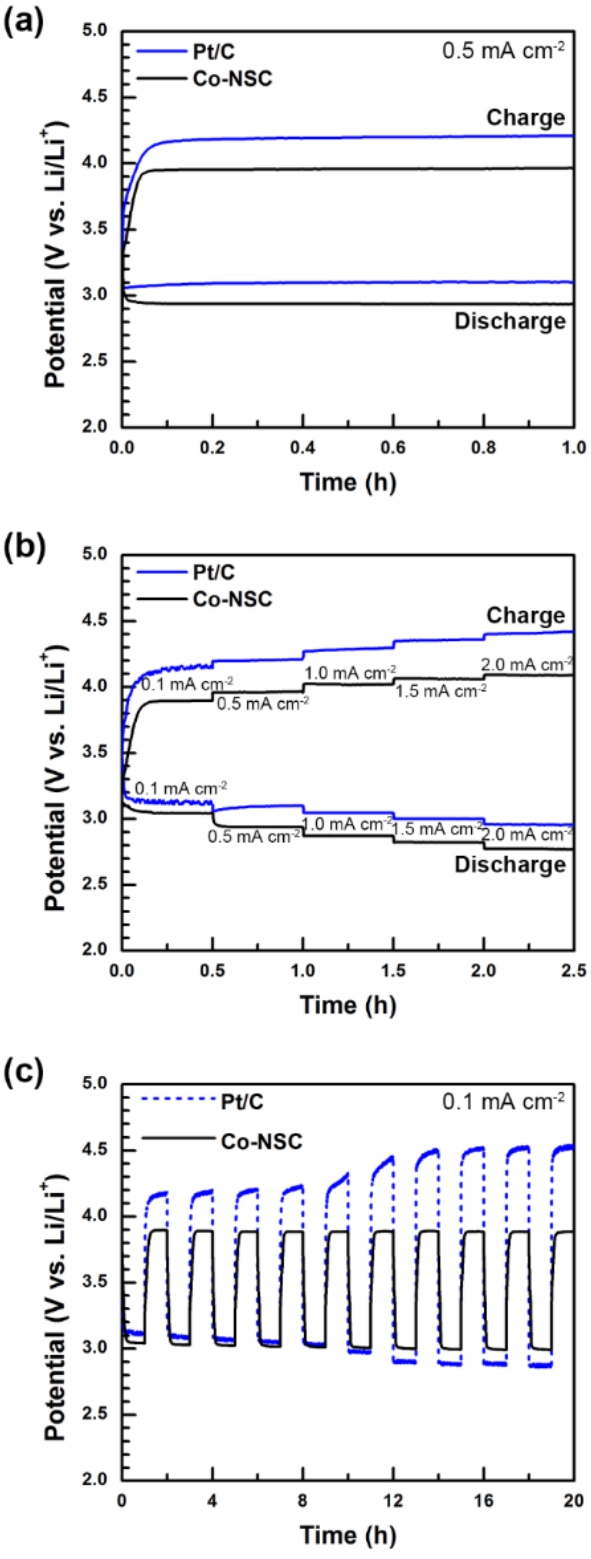

Figure 6.7 (a) Charge and discharge curves of Co-NSC and Pt/C at a current density of 0.5 mA cm^{-2}. (b) Additional discharge and charge profiles are investigated at higher current density in the range of 0.5 to 2.0 mA cm^{-2}. (c) Charge-discharge curves of Co-NSC and Pt/C at a current density of 0.1 mA cm^{-2} from 1 to 10 cycles.

6.4 Conclusion

In this study, we investigated the electrochemical characteristics of a Co-NSC composite without using a precious metal catalyst. The Co-NSC composite was synthesized by an electro-spinning method rather than a solid state or combustion process to successfully synthesize a double phase Co_3O_4 and NSC composite. The phases of the Co-NSC composite were confirmed as NSC and Co_3O_4 oxides by XRD, SEM, and TEM. The ORR onset potential and the electron transfer number of the Co-NSC composite were -0.2 V vs Hg/HgO and 3.9, respectively, and Co-NSC showed higher disc current density compared with NSC. The Co-NSC composite also has superior catalytic activity for OER to the best perovskite catalysts to date, i.e., BSCF, LSN, and LNO and the conventional IrO_2 catalyst and the composite shows remarkably good cyclic stability without significant degradation. The catalytic activity of Co-NSC is underpinned by the high concentration of Co^{3+} cations and adsorbed oxygen ratio ($O_{ad}/O_{lattice}$), which corresponds to the catalytic active sites, caused by the additional cobalt in Co-NSC. The electrochemical performance of Co-NSC and Pt/C was evaluated with a hybrid Li-air battery. The discharge and charge voltage plateaus of Co-NSC are obtained at 2.94 and 3.96 V versus Li/Li^+, respectively.

In conclusion, the high catalytic activity of Co-NSC can be explained by its unique morphology, increased Co^{3+} cations, and higher oxygen adsorption rate on the surface. Co-NSC is a suitable bifunctional catalytic cathode material that can replace precious metal-based catalysts for energy conversion and storage systems.

References

1. Y. Liang, Y. Li, H. Wang, J. Zhou, J. Wang, T. Regier, H. Dai, Nat. Mater. 2011, 10, 780–786.

2. N. S. Lewis, D. G. Nocera, Proc. Natl. Acad. Sci. 2006, 103, 15729–15735.

3. A. J. Bard, M. A. Fox, Acc. Chem. Res. 1995, 28, 141–145.

4. M. Winter, R. J. Brodd, Chem. Rev. 2005, 105, 1021–1021.

5. A. a. Gewirth, M. S. Thorum, Inorg. Chem. 2010, 49, 3557–3566.

6. H. Dau, C. Limberg, T. Reier, M. Risch, S. Roggan, P. Strasser, ChemCatChem. 2010, 2, 724–761.

7. A. Singh, L. Spiccia, Coord. Chem. Rev. 2013, 257, 2607–2622.

8. D. -G. Lee, O. Gwon, H. -S. Park, S. H. Kim, J. Yang, S. K. Kwak, G. Kim, H.-K. Song, Angew. Chemie Int. Ed. 2015, 54, 15730–15733.

9. S. -M. Park, J. Electrochem. Soc. 1986, 133, 1641.

10. M. Wiechen, M. M. Najafpour, S. I. Allakhverdiev, L. Spiccia, Energy Environ. Sci. 2014, 7, 2203.

11. M. Oezaslan, F. Hasché, P. Strasser, J. Phys. Chem. Lett. 2013, 4, 3273–3291.

12. J. -H. Kim, A. Ishihara, S. Mitsushima, N. Kamiya, K. -I. Ota, Electrochim. Acta. 2007, 52, 2492–2497.

13. G. Faubert, R. Côté, D. Guay, J. P. Dodelet, G. Dénès, C. Poleunis, P. Bertrand, Electrochim. Acta. 1998, 43, 1969–1984.

14. B. Wang, J. Power Sources. 2005, 152, 1–15.

15. H. Tang, Z. Qi, M. Ramani, J. F. Elter, J. Power Sources. 2006, 158, 1306–1312.

16. E. a. Ticianelli, J. Electrochem. Soc. 1988, 135, 2209.

17. M. S. Wilson, J. Electrochem. Soc. 1992, 139, L28.

18. D. A. Stevens, J. R. Dahn, Carbon. 2005, 43, 179–188.

19. A. Morozan, P. Jégou, S. Campidelli, S. Palacin, B. Jousselme, Chem. Commun. 2012, 48, 4627.

20. F. Li, H. Kitaura, H. Zhou, Energy Environ. Sci. 2013, 6, 2302.

21. Y. Gorlin, T. F. Jaramillo, J. Am. Chem. Soc. 2010, 132, 13612–13614.

22. Y. Gorlin, D. Nordlund, T. F. Jaramillo, ECS Trans. 2013, 58, 735–750.

23. Y. Meng, W. Song, H. Huang, Z. Ren, S. -Y. Chen, S. L. Suib, J. Am. Chem. Soc. 2014, 136, 11452–11464.

24. Q. Liu, J. Jin, J. Zhang, ACS Appl. Mater. Interfaces. 2013, 5, 5002–5008.

25. X. Cao, C. Jin, F. Lu, Z. Yang, M. Shen, R. Yang, J. Electrochem. Soc. 2014, 161, H296–H300.

26. A. Grimaud, C. E. Carlton, M. Risch, W. T. Hong, K. J. May, Y. Shao-Horn, J. Phys. Chem. C. 2013, 117, 25926–25932.

27. K. J. May, C. E. Carlton, K. A. Stoerzinger, M. Risch, J. Suntivich, Y. -L. Lee, A. Grimaud, Y. Shao-Horn, J. Phys. Chem. Lett. 2012, 3, 3264–3270.

28. J. Suntivich, H. A.Gasteiger, N. Yabuuchi, H. Nakanishi, J. B. Goodenough, Y. Shao-Horn, Nat.

Chem. 2011, 3, 546–550.

29. J. Suntivich, E. E. Perry, H. A. Gasteiger, Y. Shao-Horn, Electrocatalysis. 2013, 4, 49–55.

30. J. Suntivich, Y. Shao-Horn, ECS Trans. 2013, 58, 715–726.

31. M. Risch, K. A. Stoerzinger, S. Maruyama, W. T. Hong, I. Takeuchi, Y. Shao-Horn, J. Am. Chem. Soc. 2014, 136, 5229–5232.

32. S. Otoshi, J. Electrochem. Soc. 1991, 138, 1519.

33. S. Xu, D. Dong, Y. Wang, W. Doherty, K. Xie, Y. Wu, J. Power Sources. 2014, 246, 346–355.

34. M. Lefèvre, J. -P. Dodelet, Electrochim. Acta. 2003, 48, 2749–2760.

35. J. -I. Jung, S. Park, M. -G. Kim, J. Cho, Adv. Energy Mater. 2015, 5, 1501560.

36. K. N. Jung, J. -H. Jung, W. B. Im, S. Yoon, K. -H. Shin, J. -W. Lee, ACS Appl. Mater. Interfaces. 2013, 5, 9902–9907.

37. J. Yu, J. Sunarso, Y. Zhu, X. Xu, R. Ran, W. Zhou, Z. Shao, Chem. Eur. J. 2016, 22, 2719–2727.

38. D. C. Frost, C. A. McDowell, I. S. Woolsey, Chem. Phys. Lett. 1972, 17, 320–323.

39. G. -H. Li, L. -Z. Dai, D. -S. Lu, S. -Y. Peng, J. Solid State Chem. 1990, 89, 167–173.

40. J. Xu, P. Gao, T. S. Zhao, Energy Environ. Sci. 2012, 5, 5333.

41. F. Teng, W. Han , S. Liang , B. Gaugeu , R. Zong, Y. Zhu, J. Catal. 2007, 250, 1–11.

42. N. A. Merino, B. P. Barbero, P. Eloy, L. E. Cadús, Appl. Surf. Sci. 2006, 253, 1489–1493.

43. C. Kim, O. Gwon, I. -Y. Jeon, Y. Kim, J. Shin, Y. W. Ju, J. –B. Baek, G. Kim, J. Mater. Chem. A. 2016, 2, 975–984.

44. Y. W. Ju, S. Yoo, L. Guo, C. Kim, A. Inoishi, H. Y. Jeong, J. Shin, T. Ishihara, S. -D. Yim, G. Kim, J. Electrochem. Soc. 2015, 162, A2651–A2655.

45. Y. W. Ju, S. Yoo, C. Kim, S. Kim, I. -Y. Jeon, J. Shin, J. -B. Baek, G. Kim, Adv. Sci. 2016, 3, 1500205.

46. I. -Y. Jeon, C. Kim, G. Kim, J.-B. Baek, Carbon. 2015, 93, 465–472.

Chapter VII. A Highly Efficient and Robust Cation Ordered Perovskite Oxides as a Bi-Functional Catalyst for Rechargeable Zinc-Air Batteries

Reprinted with permission from ACS Nano, 11, 11594-11601 (2017). Copyright 2017, American Chemical Society.

7.1 Introduction

The demand for secure, clean, and renewable energy has stimulated extensive research in rechargeable metal–air batteries. Due to the intrinsic high theoretical energy density, the metal-air batteries can be potentially good candidates for next-generation electrical vehicles (EVs) and electrical energy storage systems (EES).[1-5] However, overpotential which is caused by sluggish ORR and OER kinetics of electrodes and catalysts has become one of the technical hurdle to commercialization.[6, 7] Therefore, it is extremely required to develop a bi-functional electrocatalyst having high efficiency of ORR/OER and long-term stability in order to complete rechargeable metal-air batteries. Despite precious metal related compounds, e.g., Pt, IrO_2 and RuO_2 are well known as the most efficient ORR/OER electrocatalysts, their application for large scale is limited due to high cost, scarcity and unsatisfactory durability.[8, 9] Therefore, considerable efforts have been devoted to exploring precious metal-free bi-functional electrocatalysts, such as N-doped graphene, Co_3O_4/N-doped graphene, Co_3O_4 nanowire arrays, N-doped carbon nanotube frameworks, N-P co-doped mesoporous nanocarbon foams, and metal-organic frameworks, etc.[10-12]

Recently, among the various bi-functional electrocatalysts, ABO_3 type perovskite oxides, composing of rare earth or alkali metal at the A-site and transition metal at the B-site, have been applicable as a cathode electrocatalyst.[13-18] In general, the properties of perovskite oxides can be easily controlled by partial substitution of A or B-site cations, leading to various structures, oxygen contents, and electrocatalytic properties.[19] Regarding electrocatalytic properties, some strategies have been reported to enhance the ORR/OER, such as cation doping, surface optimization, nano structuring, and employing composites.[19-22] For example, the OER of $SrCo_{0.7}Fe_{0.2}O_{3-\delta}$ was enhanced by doping niobium at the A-site, and that of $La_{0.8}Sr_{0.2}CoO_{3-\delta}$ was improved by doping iron or nickel at the B-site.[13, 20] In particular, $Ba_{0.5}Sr_{0.5}Co_{0.8}Fe_{0.2}O_{3-\delta}$ (BSCF) is a promising perovskite as the competitive candidate of electrocatalysts in the previous studies.[14, 15] However, Large amounts of H_2O_2 production and large overpotential are often observed during the ORR, a major factor in severe performance degradation.[19]

Recently, the cation ordered perovskites have been effectively used as an electrode at high temperature applications (600~900 °C) because of their high oxygen kinetics, electrical conductivity and structural stability compared with $ABO_{3-\delta}$ type perovskite oxides.[23-33] More recently, these oxides have been explored as an efficient and stable oxygen catalyst for low-temperature applications.[15, 19]

In this study, a series of $PrBa_{0.5}Sr_{0.5}Co_{2-x}Fe_xO_{5+\delta}$ (x = 0, 0.5, 1, 1.5, and 2, PBSCF) were prepared and determined the optimum Fe contents through electrochemical evaluation. To obtain nano-scale powders, electrospinning was adopted because it was known as a simple, versatile, and useful technique for making nanomaterials in large-scale preparation.[34-36] The mesoporous $PrBa_{0.5}Sr_{0.5}Co_{2-x}Fe_xO_{5+\delta}$ nanofiber (PBSCF-NF) had uniform diameter and high surface area (~20 m^2 g^{-1}). This nanofiber improved the bi-functionality of ORR/OER, especially, the OER performance was about 9 times higher than that of state-of-the-art precious metal oxide IrO_2 at overpotential of 0.3 V. Furthermore, it also demonstrated notable charge-discharge stability even at high current density (10 mA cm^{-2}) in Zn-air batteries.[37, 38]

7.2 Experimental

7.2.1 Preparation of Composite Cathode

$PrBa_{0.5}Sr_{0.5}Co_{2-x}Fe_xO_{5+\delta}$ nanofibers were fabricated by electrospinning PBSCF/ Polyacrylonitrile (PAN) solution followed by high temperature oxidation to remove the organic precursor materials. The PBSCF/PAN precursor solution consisted of $Pr(NO_3)_3 \cdot 6H_2O$, $Ba(NO_3)_2$, $Sr(NO_3)_2$, $Co(NO_3)_2 \cdot 6H_2O$, $Fe(NO_3)_3 \cdot 9H_2O$ (Sigma-Aldrich Co., 99+%), polyacrylonitrile (PAN), and N, N-dimethylformamide (DMF, Alfa Aesar Co.). In a typical procedure, the electrospinning solution was prepared by dissolving the above metal nitrates (1 mM) in DMF solvent in a molar ratio of Pr: Ba: Sr: Co: Fe = 1: 0.5: 0.5: 1.5: 0.5. The proper quantity of PAN was added into the resulting solution, followed by stirring for 12 h to ensure dissolution of all precursor materials. The as-prepared PBSCF precursor solution was loaded into a plastic syringe equipped with a 25-gauge stainless steel needle, electrically connected to a high voltage power supply. For the electrospinning experiment, the applied voltage was fixed at 15 kV and the distance of the needle to the collector was maintained at 12 cm. The syringe was held stationary as the fibers were collected on a rotating drum. The whole piece of the nanofiber precursor was peeled off and clipped onto two aluminum sheets and then heated at 900 ^oC for 2 h to achieve a pure perovskite structure, with a heating rate of 2 $^oC\ min^{-1}$.

7.2.2 Electrochemical Characterization

The microstructure was examined by scanning electron microscopy (SEM, Nova FE-SEM) and transmission electron microscopy (TEM, JEOL, JEM-2100F). The phase structure of PBSCF-F was characterized by X-ray powder diffraction (XRD, Rigaku diffractometer, Cu Kα radiation) with a scan rate of 0.1 $^o\ min^{-1}$. The program GSAS was used for the Rietveld refinement of powder pattern and lattice parameters.

A computer-controlled potentiostat (Biologic VMP3) with a RRDE-3A rotating disk electrode system was used for the electrochemical tests. An Hg/HgO (1 M NaOH filled) electrode was employed as the reference electrode and a platinum wire was used as the counter-electrode. The catalysts (physically mixing 18 mg of catalyst and 2 mg Ketjen Black (EC-600JD, KB) were first dispersed in ethanol/isopropyl alcohol solution (10 mg mL^{-1}) and Nafion (25 wt.%) stock solution (10 μL) in ethanol was added to the catalyst ink by bath sonication to prepare the catalyst ink. A total of 5 μL of well-dispersed catalyst ink was applied onto the pre-polished glassy carbon (GC) disk electrode (4 mm in diameter) for the working electrodes. IrO_2 also used to compare with other samples, and its surface area is 24.1 $m^2\ g^{-1}$.

7.2.3 Preparation of Rechargeable Zn-Air Battery

Zinc plate was used as the anode which separated by a nylon polymer membrane separator (Cell guard 3501 membrane) with the cathode and 6 M KOH electrolyte was filled between the cathode and anode, nickel mesh was used as a current collector. The only difference between the primary and rechargeable Zn-air battery was 0.2 M Zinc acetate should be added in 6M KOH as electrolyte for rechargeable one. The air cathodes were prepared by coating a mixture of PTFE binder (60 wt.% PTFE emulsion in water, Sigma-Aldrich), activated charcoal (Darco G-60A, Sigma-Aldrich) and electrocatalyst (PBSCF-NF or Pt/C+IrO_2) in a ratio of 65: 8: 27, respectively. The pristine air electrode, which could work as gas diffusion layer consists of carbon and PTFE binder, was used for comparison. An assembled full-cell was performed at several discharge and charge currents.

7.3 Results and Discussions

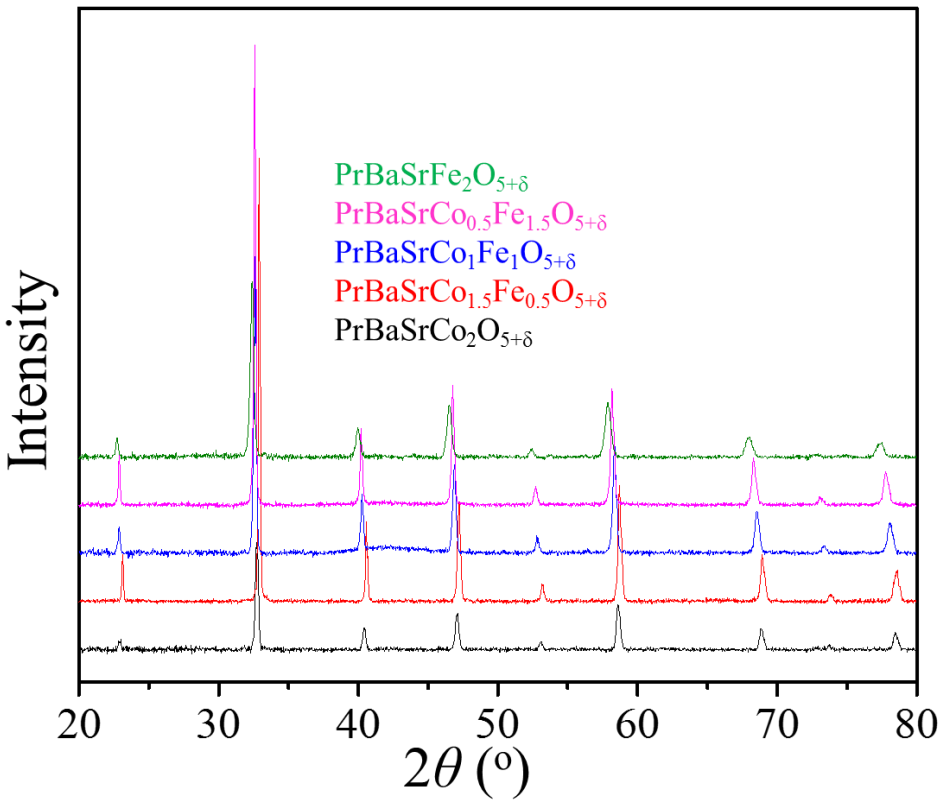

Figure 7.1 XRD of the $PrBa_{0.5}Sr_{0.5}Co_{2-x}Fe_xO_{5+\delta}$ (x = 0, 0.5, 1, 1.5, and 2) calcined at 1100 °C.

In this study, we synthesized a series of bulk $PrBa_{0.5}Sr_{0.5}Co_{2-x}Fe_xO_{5+\delta}$ (x = 0, 0.5, 1, 1.5, and 2, PBSCF-P) calcined at 1100 °C in air for 12 hours. The X-ray diffraction (XRD) was performed to determine the crystal structure of the prepared samples as shown in Fig. 7.1, showing that a single-phase crystal structure without any detectable impurities. As we reported in previous study, the lattice of PBSCF-P was expanded as small Co^{3+} (r = 0.545 Å) or Co^{4+} (r = 0.530 Å) ions were replaced by larger Fe^{3+} (r = 0.645 Å) or Fe^{4+} (r = 0.585 Å) ions.

Meanwhile, it is well known that the concentration of oxygen vacancies and the cobalt oxidation state in cation ordered perovskites inevitably affect ORR/OER activity. Because the oxygen vacancies and the cobalt oxidation state are the factors that affect the covalent bond between metal 3d and the oxygen 2p orbital. In addition, the electronegativity of the material has also been reported as one of the reasons for affecting ORR activity. The Fe, which has smaller Pauling electronegativity (1.83) than Co (1.88), doping in B-site also leads to change of the oxygen vacancies and the cobalt oxidation state. Therefore, we expected that the proper amount of Fe doping would electrochemically improve the catalytic activity during the ORR and OER process based on those reasons.[39, 40]

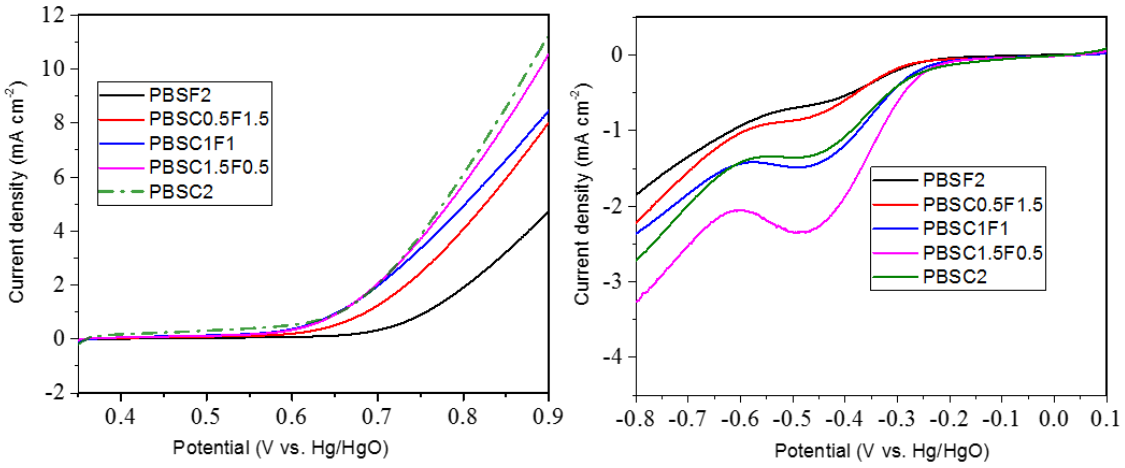

Figure 7.2 (a) OER polarization curves of $PrBa_{0.5}Sr_{0.5}Co_{2-x}Fe_xO_{5+\delta}$ (x = 0, 0.5, 1, 1.5, and 2), respectively, in O_2-saturated 0.1 M KOH at a rotation rate of 1600 rpm and a scan rate of 10 mV s^{-1}. (b) ORR polarization curves after ten consecutive scans for $PrBa_{0.5}Sr_{0.5}Co_{2-x}Fe_xO_{5+\delta}$, respectively, in O_2-saturated 0.1 M KOH at rotation rate of 1600 rpm and scan rate of 10 mV s^{-1}. Note that, there are only perovskite oxides in the GC electrode for the comparison of those catalysts.

The optimal ratio of the PBSCF-P was initially determined based on the OER and ORR performance. The electrochemical performances of well-synthesized series of PBSCF-P samples were evaluated using rotating ring-disk electrode (RRDE) as shown in Fig. 7.2. The $PrBa_{0.5}Sr_{0.5}Co_{1.5}Fe_{0.5}O_{5+\delta}$ (x = 0.5, PBSC1.5F0.5) showed the highest active ORR and OER activity among the PBSCF-P series. Based on the general design principles of the perovskite oxides, the high oxidation state of transition metal (near 1 of e_g filling corresponds to maximum activity) is one of the reason to enhance the ORR/OER activity. As shown in Fig. 7.3, the X-ray photoelectron spectroscopy (XPS) results exhibited that the calculated ratio of Fe^{4+}/Fe^{3+} on the surface of the PBSC1.5F0.5 catalyst is 37.5/62.5, which will benefit its high catalytic activity.

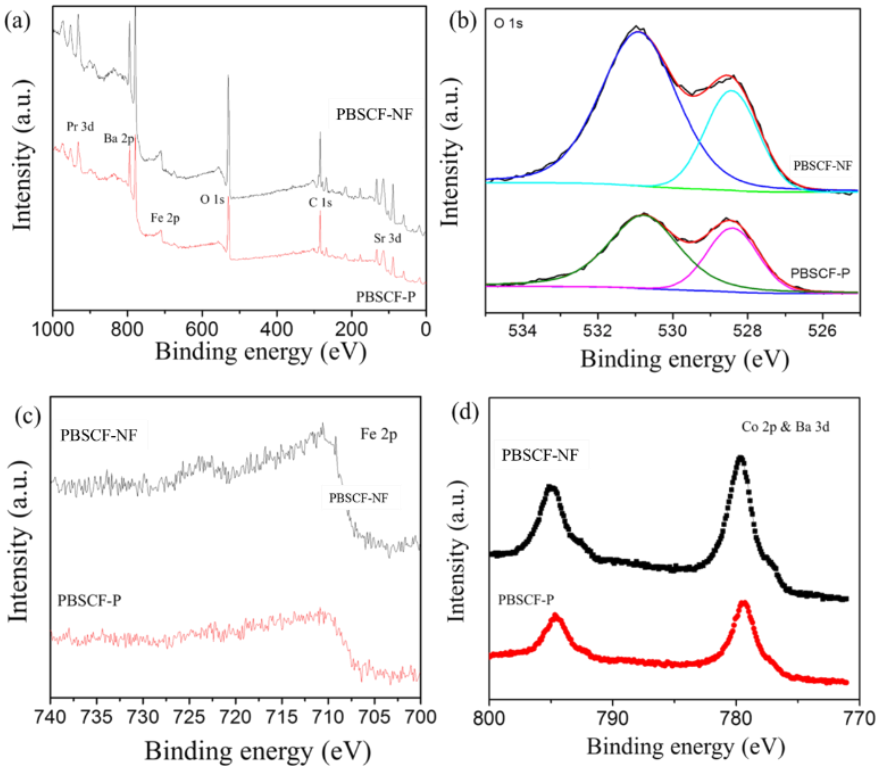

Figure 7.3 (a) XPS survey spectra of PBSCF-NF and PBSCF-P; (b) O 1s; (c) Fe 2p; (d) Co 2p and Ba 3d.

Mesoporous nanofiber of PBSCF (PBSCF-NF) with optimal ratio was synthesized by electrospinning and the subsequent experiments were conducted. The morphology of the PBSCF-NF was tailored by varying the precursor solutions and electrospinning parameters. The concentration of metal nitrate precursors in DMF was fixed at 1.0 mM, while the concentration of PAN was systematically controlled from 6 wt.% to 10 wt.%. Figure 7.4 showed the SEM images of PBSCF-NF containing various concentrations of PAN. As the concentration of PAN increase, it can be clearly seen that the size and number of beads were dramatically reduced, and the diameter of fiber was enlarged. The calcination temperature was also controlled to identify patterns of morphology and particle growth. The high calcination temperature increases the size of particles, reducing the size of the mesoporous of the nanofibers as shown in Fig. 7.4. The Brunauer–Emmett–Teller (BET) surface area of PBSCF-NF was measured as 16.2 m^2 g^{-1}, which was about 8 times higher than that of PBSCF-P as shown in Fig. 7.5. The spacious surface of PBSCF-NF can serve as an excellent electrocatalyst since it can provide many active sites.

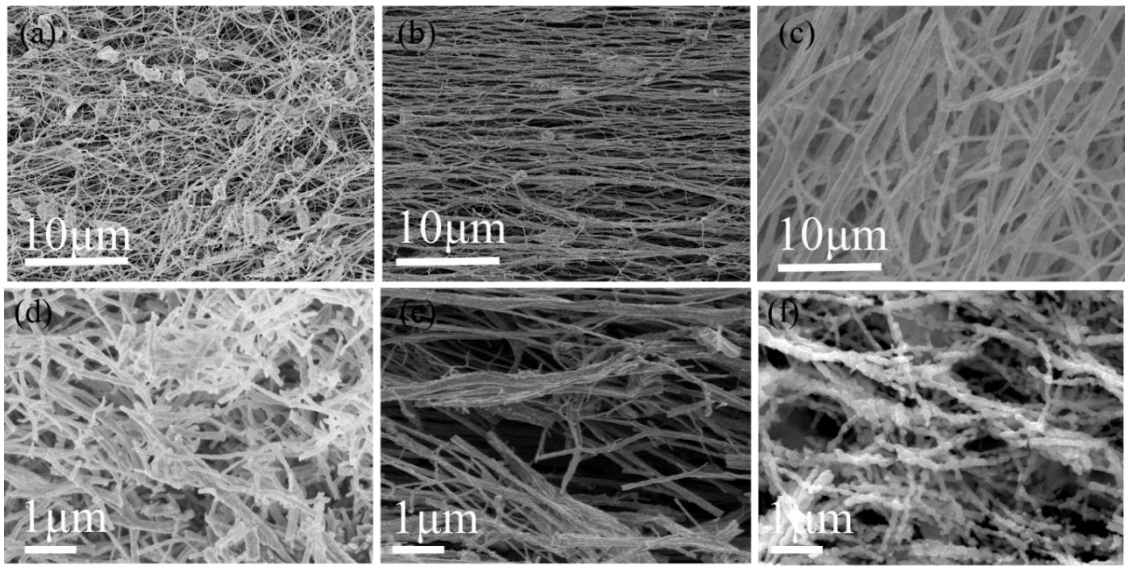

Figure 7.4 SEM images of electrospun PBSCF-NF with different concentrations of PAN, (a) 6 wt.% PAN, (b) 8 wt.% and (c) 10 wt.% PAN; PBSCF-NF calcined in air for 2 h, (d) 900 °C 2 h, (e) 950 °C 2 h and (f) 1000 °C 2 h.

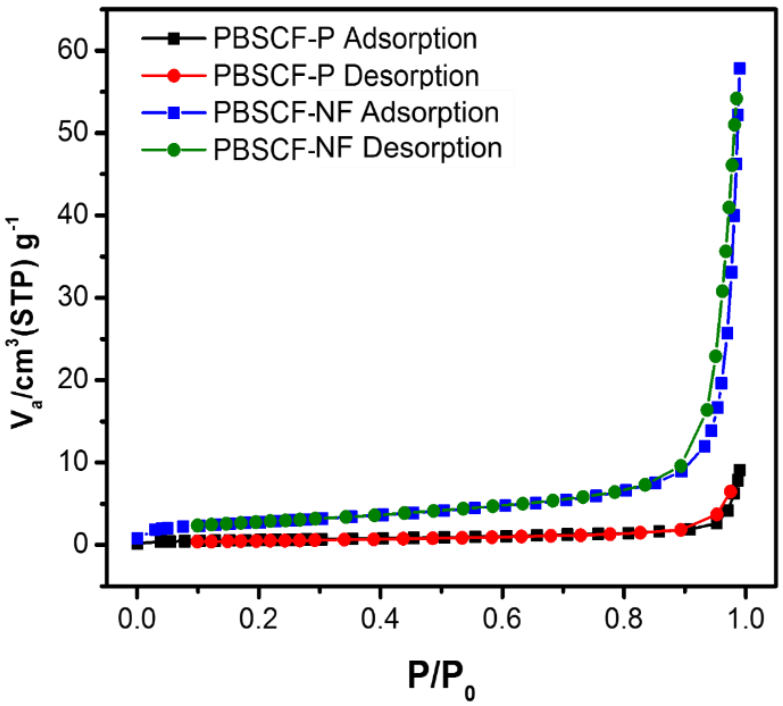

Figure 7.5 N_2 adsorption–desorption isotherms for the PBSCF-NF and PBSCF-P.

As shown in Fig. 7.6(a), all peaks of PBSCF-NF were indexed to tetragonal (P4/mmm) with lattice

parameters of a = 3.871 Å and c = 7.757 Å confirmed by the Rietveld refinement. The crystal structure and morphology of optimized PBSCF-NF were further precisely investigated by transmission electron microscopy (TEM). High resolution TEM (HR-TEM) showed that the crystal structure was confirmed as A-cation ordering, which provides the formation of an oxygen deficient square pyramidal symmetry. The localized oxygen vacancies in the Pr plane from the ordering crystalline structure lead to the oxygen kinetics and structural stability. The low-magnification TEM image in Fig. 7.6(b) showed that the mesoporous nanofiber with a diameter of 300 nm make from homogenously dispersed 20-40 nm sizes of nanoparticles and 5-10 nm range of mesoporous. Lattice spacing of the (001) and (100) planes in the tetragonal structure of the PBSCF-NF was 0.775nm and 0.385 nm, respectively (Fig. 7.6(c)). The electron energy-loss spectroscopy (EELS) profile measurement was performed to confirm the elements in the PBSCF-NF. Figure 7.6(e) and (f) showed the clearly visible peaks of the O, Fe, Co, and Pr elements at a point of the fiber (less than 1nm in diameter) and at the red cross-line on the PBSCF-NF shown in Fig. 7.6(d), respectively.

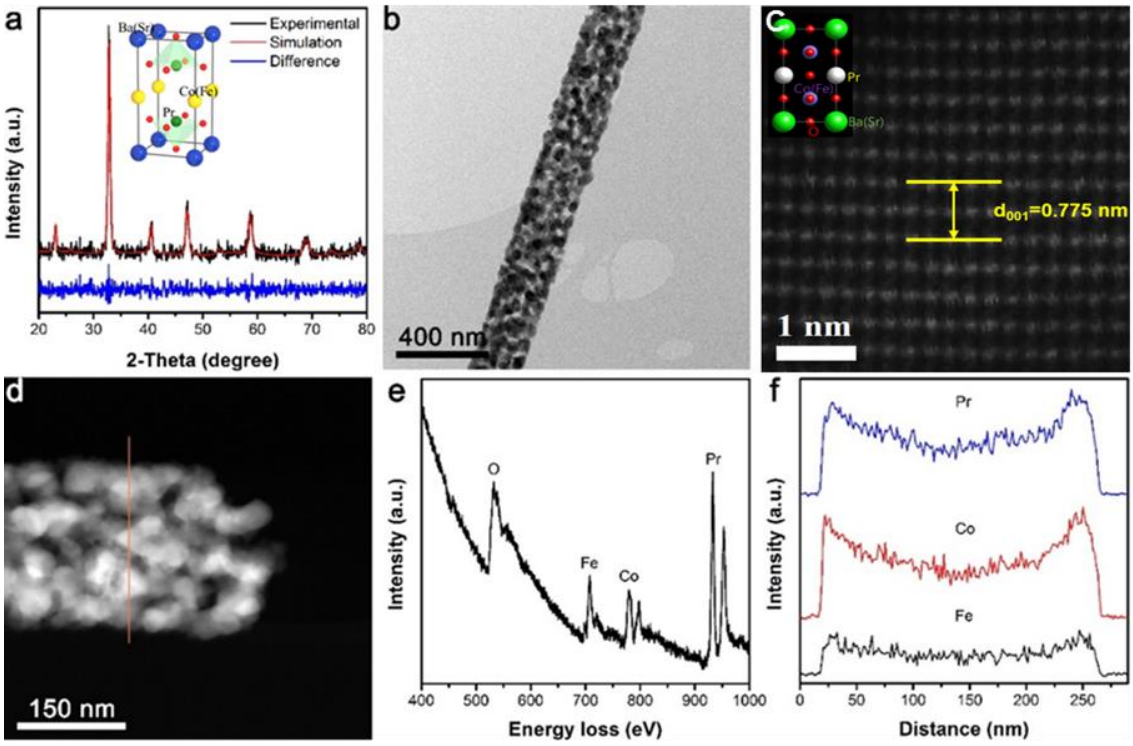

Figure 7.6 (a) Refined XRD profiles of the PBSCF-NF. (b) TEM image of PBSCF-NF. (c) High resolution TEM image of PBSCF-NF. (d) STEM image of PBSCF-NF. (e) Energy-loss spectrum of the PBSCF-NF. (f) Line scan across the PBSCF-NF from a red line on the nanofiber in (d).

The OER performance of PBSCF-NF was investigated in 0.1 M KOH solution (PH=13) and compared with PBSCF-P, IrO_2 and BSCF. As shown in Fig. 7.7(a), PBSCF-NF exhibited a small onset

potential of 1.52 V, which was much smaller than that of the state-of-art IrO_2 (1.56 V). In addition, the Tafel slope of the PBSCF-NF (81 mV dec^{-1}) was significantly lower than those of PBSCF-P (121 mV dec^{-1}), IrO_2 (115 mV dec^{-1}), and BSCF (196 mV dec^{-1}).[7] Because of the low Tafel slope, the OER current of PBSCF-NF increases rapidly with the increase of overvoltage, which makes PBSCF-NF more competitive in practical applications. At current density of 10 mA cm^{-2}, PBSCF-NF showed lower overpotential (0.3 V) compared to PBSCF-P, IrO_2, and BSCF (0.42 V, 0.45 V and 0.54 V) as shown in Fig. 7.7(c). It also has much smaller overpotential than other recently reported electrocatalysts. Moreover, the current density of PBSCF-NF, PBSCF-P, IrO_2, and BSCF at overpotential of 0.3 V was 9.1, 1.5, 1.0 and 1.5 mA cm^{-2}, respectively as shown in Fig. 7.7(d), indicating that PBSCF-NF is superior OER electrocatalytic activity. It is interesting to compare their specific activity (current per BET area, SA, mA cm_{BET}^{-2} at 1.55 V) due to assess the intrinsic OER activities of the catalysts without surface area. This result shows that the SA of PBSCF-NF (0.092 mA cm_{BET}^{-2}) was higher than that of PBSCF-P (0.029 mA cm_{BET}^{-2}) and IrO_2 (0.008 mA cm_{BET}^{-2}).

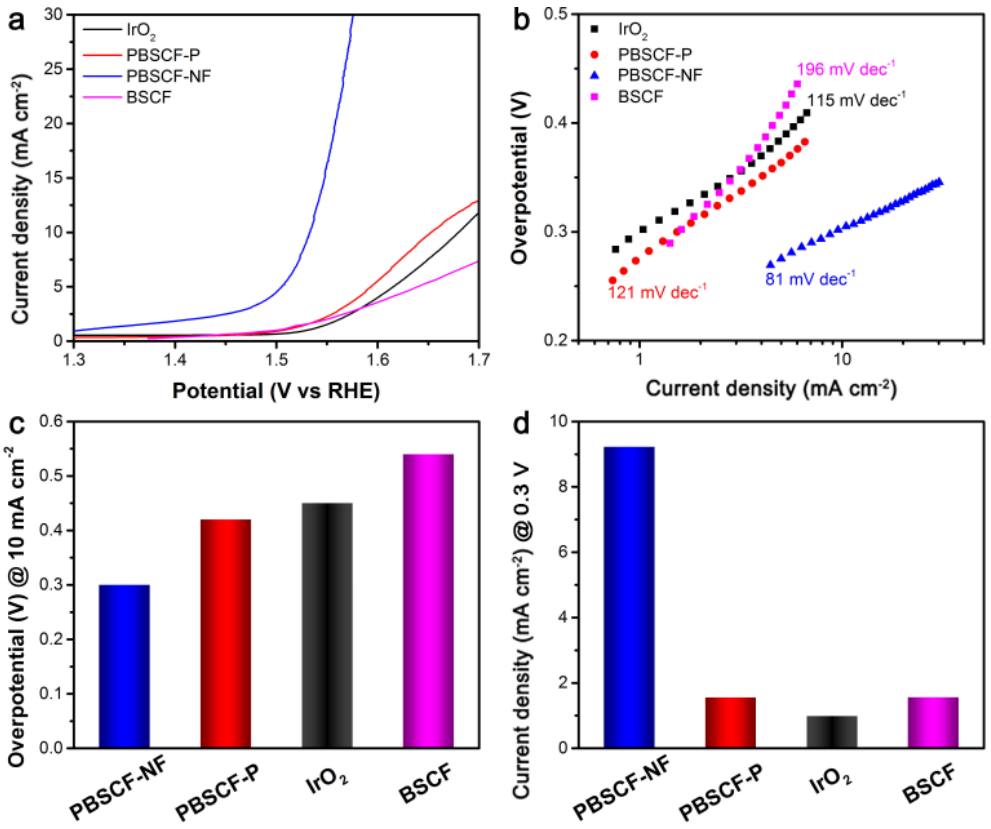

Figure 7.7 OER activities of PBSCF-NF, PBSCF-P, BSCF and IrO_2. (a) Polarization curves of PBSCF-NF, PBSCF-P, BSCF and IrO_2 electrocatalysts in 0.1 M KOH solution at 1600 rpm with 10 mV s^{-1} scan rate. (b) Tafel plots obtained from the polarization curves in (a). (c) Overpotentials of PBSCF-NF, PBSCF-P, BSCF and IrO_2 at a current density of 10 mA cm^{-2}. (d) Currents densities of PBSCF-NF, PBSCF-P, BSCF and IrO_2 at an overpotential of 0.3 V.

The XPS results reveal that the relative content of lattice oxygen species (528.4 eV) on the surface of PBSCF-NF is 19% smaller than that of PBSCF-P (Fig. 7.3(b)). Also, the oxygen non-stoichiometry (5+δ) of PBSCF-NF (5.822 ± 0.005) and PBSCF-P (5.910 ± 0.005) was quantified using iodometric titration, indicating that the nanofibers had a large amount of oxygen vacancies.[41, 42] Following the previous study, it has been demonstrated that the OER performance of the perovskite oxides is largely enhanced by the modification of the oxygen deficiency.[43] In summary, the superior performance of PBSCF-NF can be explained with the presence of faster mass transport active sites provided by the mesoporous fiber structure and the oxygen deficiency on the surface of oxides. In addition, the superior electrochemical stability of PBSCF-NF was confirmed by a long-term cycling test (5000 cycles) in 0.1 M KOH solution.

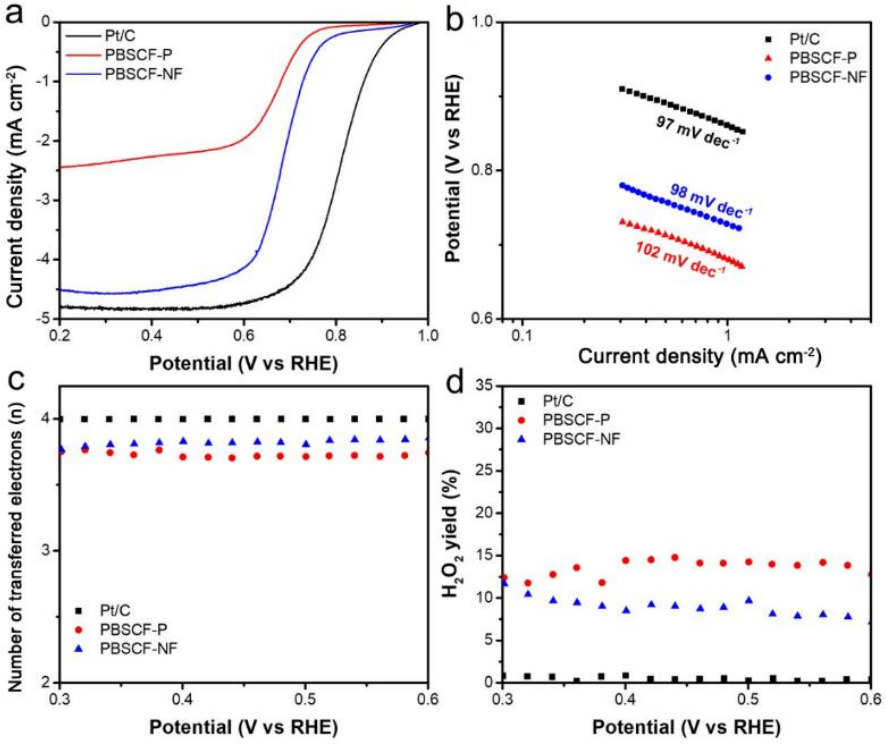

Figure 7.8 ORR activity of PBSCF-NF, PBSCF-P, and Pt/C. (a) Polarization curves of PBSCF-NF, PBSCF-P, and Pt/C electrocatalysts in 0.1 M KOH solution. (b) Tafel plots obtained from the polarization curves in (a). (c) The electron transfer numbers of PBSCF-NF, PBSCF-P, and Pt/C at different potentials. (d) H_2O_2 yield of PBSCF-NF, PBSCF-P, and Pt/C. (Electrode rotation speed: 1600 rpm, Scan rate: 10 mV s^{-1}, Catalyst loading = 0.796 mg cm^{-2})

The ORR performance was further studied in the same electrolyte (0.1 M KOH solution, PH=13). As shown in Fig. 7.8(a), PBSCF-NF showed more positive onset potential than PBSCF-P and BSCF.

Meanwhile, it showed compatible onset potential that was only 134 mV difference compared to Pt/C. The enhanced electrocatalytic activity of PBSCF-NF was identified by the smaller Tafel slope (98 mV dec^{-1}) relative to PBSCF-P (102 mV dec^{-1}), Pt/C (112 mV dec^{-1}), and BSCF (121 mV dec^{-1}).[15] Although the PBSCF-NF showed a relatively low half-wave potential compared to that of the Pt/C, the ORR performance was comparable to the recently reported non-perovskite-type catalysts. To obtain more information of the ORR process, the electron transfer number (n) and peroxide yield were calculated based on the RRDE results and following equations;

$$n = 4 \times \frac{I_d}{I_d + I_r/N} \qquad (1)$$

$$HO_2^-(\%) = 200 \times \frac{I_r/N}{I_d + I_r/N} \qquad (2)$$

where I_d is disk current, I_r is ring current, and the collection efficiency (N) is 0.41 determined by experimental measurement. The electron transfer number of PBSCF-NF in the potential range of 0.3-0.6 V was 3.77-3.89 which was larger than that of PBSCF-P (3.62-3.77) and BSCF (3.59-3.74).[44] It is very close to the n value of Pt/C (4.00), and it is possible to efficiently reduce oxygen to OH^- through highly desired four electron pathways (Fig. 7.8(c)). Furthermore, the peroxide yield was less than 11 % for PBSCF-NF in the potential range of 0.3-0.6 V, while it was much higher than 35 % for BSCF (Fig. 7.8(d)).[23] Interestingly, even though PBSCF-P exhibited smaller electron transfer number and higher peroxide yield when it compares to PBSCF-NF, two parameters were much better than those of perovskites and non-perovskite-type metal oxides. In other words, the intrinsic catalytic properties of PBSCF perovskite oxide are extremely admirable based on two parameters. Furthermore, the ORR stability of PBSCF-NF was investigated by a long-term cycling test (3000 cycles) in 0.1 M KOH solution and the HR-TEM images after cycling test, showing no significant performance degradation and maintaining its original crystalline structure after cycles (Fig. 7.9 and 7.10).

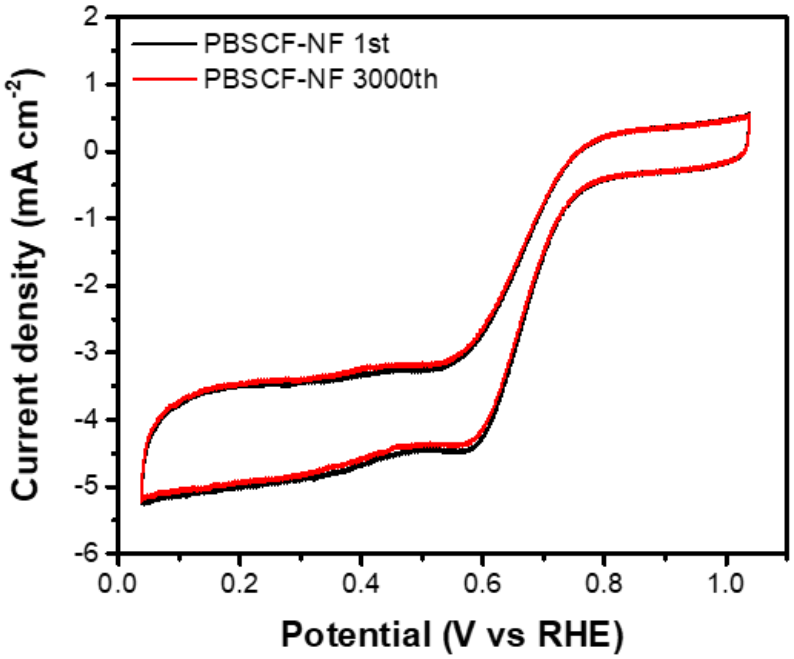

Figure 7.9 Cyclic voltammetry profiles of PBSCF-NF in an O_2-saturated 0.1 M KOH solution with scan rate of 10 mV s^{-1}.

The Zn-air battery was fabricated by using the gas diffusion layer loaded with catalysts for the cathode, Zn plate anode, and 6 M KOH electrolyte. The discharge polarization curves of PBSCF-NF and Pt/C were obtained by scanning current density upto 300 mA cm^{-2} as shown in Fig. 7.11(a). The power density of PBSCF-NF showed 127 mW cm^{-2}, higher than that of pristine air electrode (109 mW cm^{-2}) (Fig. 7.11(b)). Figure 7.11(c) presented the discharge curves of each electrode at a discharge current density of 10 mA cm^{-2}. Although PBSCF-NF exhibited a lower operating voltage (1.25 V) than Pt/C (1.38 V), the duration of PBSCF-NF (56k seconds) was much longer than that of the Pt/C (48k seconds) and pristine air electrode (43k seconds). Figure 7.11(d) displayed the charge-discharge cycling stability tests of the Zn–air battery at exceptional high current density of 10 mA cm^{-2}. Apparently, in early discharge cycles, the discharge voltage of PBSCF-NF cathode showed comparable results with the mixed Pt/C+IrO_2 composite. Even though PBSCF-NF cathode showed notably stable discharge voltage during whole cycling test (150 cycles), Pt/C+IrO_2 composite cathode rapidly decreased during the long-term cycling. The potential gaps between charge and discharge of PBSCF and Pt/C+IrO_2 were increased ~0.25 V and ~0.40 V during the cycle, respectively. Therefore, the cation ordered PBSCF-NF is one of the best performing nonprecious metal bifunctional catalysts for rechargeable zinc–air battery, evidenced by high round-trip efficiency with notable robust cycling test.

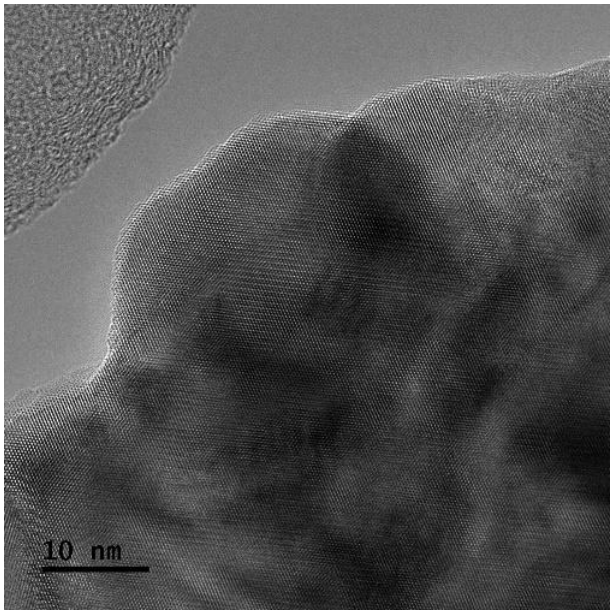

Figure 7.10 the HR-TEM picture after the long stability test.

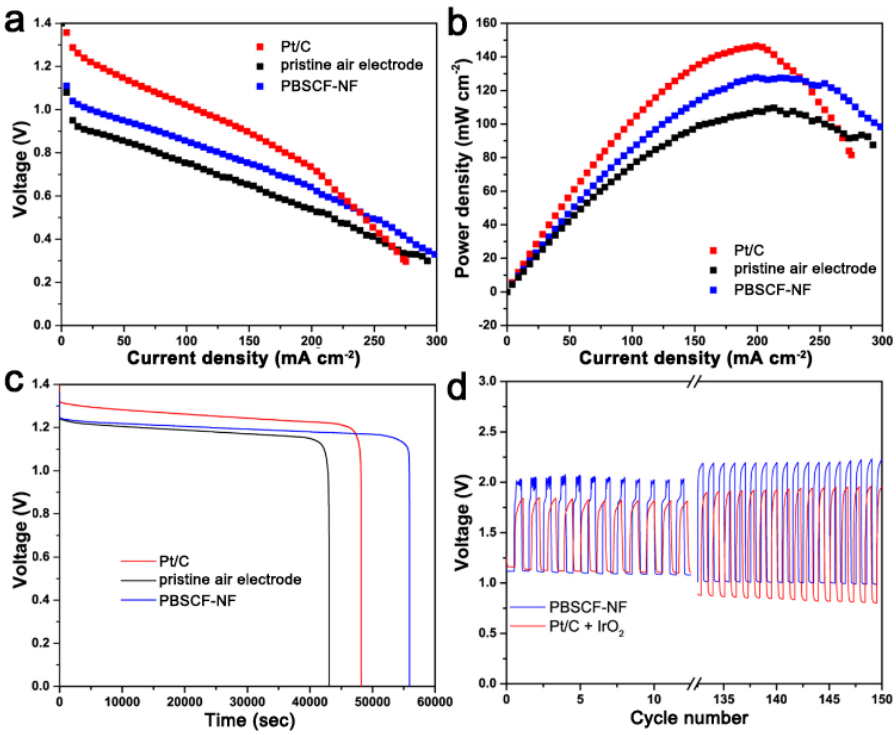

Figure 7.11 (a) Current density–voltage curves. (b) Power density curves. (c) Discharge curves at a current density of 10 mA cm^{-2} of Zn–air battery using Pt/C, PBSCF-NF and pristine air electrode. (d) Discharge and charge cycling curves of rechargeable Zn–air batteries based on PBSCF-NF and the mixed Pt/C+IrO_2 composite at a current density of 10 mA cm^{-2}.

7.4 Conclusion

In this study, we demonstrated the notable effects of the cation ordered perovskite oxide PBSCF-NF as a highly active and stable non-precious catalyst for the OER and ORR in alkaline media. The optimized PBSC1.5F0.5 nanofiber was exhibited much better OER and ORR performance than its bulk particle and BSCF perovskite. The enhanced catalytic performance of PBSCF-NF is originated from the mesoporous nanofiber structure and advanced intrinsic properties, such as high electrical conductivity, fast oxygen kinetics, and structural durability. Those favorable results lead the enhancement of the Zn-air battery performance and the charge-discharge cycling stability. Therefore, the mesoporous nanofiber PBSCF-NF is highly promising catalyst for rechargeable metal-air batteries because of efficient bi-functional ORR/OER activities and charge-discharge cycling stability in Zn-air battery.

References

1. W. Li, J. Liu, D. Zhao, Nat. Rev. Mats. 2016, 1, 16023.

2. J. S. Lee, G. S. Park, H. I. Lee, S. T. Kim, R. Cao, M. Liu, J. Cho, Nano Lett. 2011, 11, 5362−5366.

3. L. Li, S. -H. Chai, S. Dai, A. Manthiram, Energy Environ. Sci. 2014, 7, 2630−2636.

4. Z. Chen, A. Yu, D. Higgins, H. Li, H. Wang, Z. Chen, Nano Lett. 2012, 12, 1946−1952.

5. H. Yao, G. Zheng, W. Li, M. T. McDowell, Z. Seh, N. Liu, Z. Lu, Y. Cui, Nano Lett. 2013, 13, 3385−3390.

6. Y. Gorlin, T. F. Jaramillo, J. Am. Chem. Soc. 2010, 132, 13612−13614.

7. J. Zhang, Z. Zhao, Z. Xia, L. Dai, Nat. Nanotechnol. 2015, 10, 444−452.

8. J. Zhang, J. Fu, X. Song, G. Jiang, H. Zarrin, P. Xu, K. Li, A. Yu, Z. Chen, Adv. Energy Mater. 2016, 6, 1600476.

9. W. T. Hong, M. Risch, K. A. Stoerzinger, A. Grimaud, J. Suntivich, Y. Shao-Horn, Energy Environ. Sci. 2015, 8, 1404−1427.

10. G. Wu, A. Santandreu, W. Kellogg, S. Gupta, O. Ogoke, H. Zhang, H. -L. Wang, L. Dai, Nano Energy. 2016, 29, 83−110.

11. J. Yin, Y. Li, F. Lv, Q. Fan, Y. Q. Zhao, Q. Zhang, W. Wang, F. Cheng, P. Xi, S. Guo, ACS Nano 2017, 11, 2275−2283.

12. B. Y. Xia, Y. Yan, N. Li, H. B. Wu, XWD. Lou, X. Wang, Nat. Energy 2016, 1, 15006.

13. Y. Zhu, W. Zhou, Z. G. Chen, Y. Chen, C. Su, M. O. Tade, Z. Shao, Angew. Chem. Int. Ed. 2015, 54, 3897−3901.

14. J. Suntivich, K. J. May, H. A. Gasteiger, J. B. Goodenough, Y. Shao-Horn, Science. 2011, 334, 1383−1385.

15. A. Grimaud, K. J. May, C. E. Carlton, Y. L. Lee, M. Risch, W. T. Hong, J. Zhou, Y. Shao-Horn, Nat. Commun. 2013, 4, 2439.

16. D. G. Lee, O. Gwon, H. S. Park, S. H. Kim, J. Yang, S. K. Kwak, G. Kim, H. K. Song, Angew. Chem. Int. Ed. 2015, 54, 15730−15733.

17. O. Gwon, C. Kim, O. Kwon, H. Y. Jeong, H. K. Park, J. Shin, Y. W. Ju, G. Kim, J. Electrochem. Soc. 2016, 163, A1893−A1897.

18. C. Hwang, O. Gwon, H. Jo, K. M. Ok, G. Kim, ChemElectroChem. 2017, 4, 468−471.

19. D. Chen, C. Chen, Z. M. Baiyee, Z. Shao, F. Ciucci, Chem. Rev. 2015, 115, 9869−9921.

20. S. K. Tiwari, S. P. Singh, R. N. Singh, J. Electrochem. Soc. 1996, 143, 1505−1510.

21. J. I. Jung, H. Y. Jeong, J. S. Lee, M. G. Kim, J. Cho, Angew. Chem. Int. Ed. 2014, 53, 4582−4586.

22. J. Yu, J. Sunarso, Y. Zhu, X. Xu, R. Ran, W. Zhou, Z. Shao, Chem. Eur. J. 2016, 22, 2719−2727.

23. J. I. Jung, S. Park, M. G. Kim, J. Cho, Adv. Energy Mater. 2015, 5, 1501560.

24. B. Han, K. A. Stoerzinger, V. Tileli, A. D. Gamalski, E. A. Stach, Y. Shao-Horn, Nat. Mater. 2017,

16, 121−126.

25. S. Yoo, A. Jun, Y. W. Ju, D. Odkhuu, J. Hyodo, H. Y. Jeong, N. Park, J. Shin, T. Ishihara, G. Kim, Angew. Chem. Int. Ed. 2014, 53, 13064−13067.

26. Z. Shao, S. M. Haile, Nature. 2004, 431, 170−173.

27. J. I. Jung, M. Risch, S. Park, M. G. Kim, G. Nam, H. Y. Jeong, Y. Shao-Horn, J. Cho, Energy Environ. Sci. 2016, 9, 176−183.

28. S. Choi, S. Yoo, J. Kim, S. Park, A. Jun, S. Sengodan, J. Kim, J. Shin, H. Y. Jeong, Y. Choi, G. Kim, M. Liu, Sci. Rep. 2013, 3, 2426.

29. Y. Zhu, C. Su, X. Xu, W. Zhou, R. Ran, Z. Shao, Chem. Eur. J. 2014, 20, 15533−15542.

30. S. Sengodan, S. Choi, A. Jun, T. H. Shin, Y. W. Ju, H. Y. Jeong, J. Shin, J. T. S. Irvine, G. Kim, Nat. Mater. 2015, 14, 205−209.

31. J. Kim, S. Choi, A. Jun, H. Y. Jeong, J. Shin, G. Kim, ChemSusChem. 2014, 7, 1669−1675.

32. X. Xu, C. Su, W. Zhou, Y. Zhu, Y. Chen, Z. Shao, Adv. Sci. 2016, 3, 1500187.

33. J. Yu, G. Chen, J. Sunarso, Y. Zhu, R. Ran, Z. Zhu, W. Zhou, Z. Shao, Adv. Sci. 2016, 3, 1600060.

34. Y. Chen, Y. Bu, Y. Zhang, R. Yan, D. Ding, B. Zhao, S. Yoo, D. Dang, R. Hu, C. Yang, M. Liu, Adv. Energy Mater. 2017, 7, 1601890.

35. Y. Zhu, W. Zhou, Y. Zhong, Y. Bu, X. Chen, Q. Zhong, M. Liu, Z. Shao, Adv. Energy Mater. 2017, 7, 1602122.

36. Y. Chen, Y. Bu, B. Zhao, Y. Zhang, D. Ding, R. Hu, T. Wei, B. Rainwater, Y. Ding, F. Chen, C. Yang, J. Liu, M. Liu, Nano Energy. 2016, 26, 90−99.

37. M. G. Park, D. U. Lee, M. H. Seo, Z. P. Cano, Z. Chen, Small. 2016, 12, 2707−2714.

38. G. Nam, J. H. Park, M. Choi, P. Oh, S. Park, M. G. Kim, N. J. Park, J. Cho, J. S. Lee, ACS Nano. 2015, 9, 6493−6501.

39. B. Hua, Y. Q. Zhang, N. Yan, M. Li, Y. F. Sun, J. Chen, J. Li, J. L .Luo, Adv. Funct. Mater. 2016, 26, 4106−4112.

40. R. T. Sanderson, J. Am. Chem. Soc. 1983, 105, 2259−2261.

41. A. Grimaud, O. Diaz-Morales, B. Han, W. T. Hong, Y. L. Lee, L. Giordano, K. A. Stoerzinger, M. T. M. Koper, Y. Shao-Horn, Nat. Chem. 2017, 9, 457−465.

42. L. Xu, Q. Jiang, Z. Xiao, X. Li, J. Huo, S. Wang, L. Dai, Angew. Chem. Int. Ed. 2016, 55, 5277−5281.

43. J. R. Petrie, H. Jeen, S. C. Barron, T. L. Meyer, H. N. Lee, J. Am. Chem. Soc. 2016, 138, 7252−7255.

44. E. Fabbri, R. Mohamed, P. Levecque, O. Conrad, R. Kötz, T. J. Schmidt, ACS Catal. 2014, 4, 1061−1070.

Appendix I. List of Publications

1. **Ohhun Gwon**†, Keunsu Choi†, Hansol Lee, Chanseok Kim, Jun Hee Lee*, and Guntae Kim*, Enhancing Bifunctional Electrocatalytic Activities via Metal d-Band-Center-Lift in $Sm_{0.5}Sr_{0.5}CoO_{3-\delta}$ Perovskites, **This research will be published.**

2. Yunfei Bu, Haeseong Jang, **Ohhun Gwon**, Su Hwan Kim, Se Hun Joo, Gyutae Nam, Seona Kim, Yong Qin, Qin Zhong, Sang Kyu Kwak*, Jaephil Cho*, and Guntae Kim*, Synergistic interaction of perovskite oxides and N-doped graphene in versatile electrocatalyst, **J. Mater. Chem. A.** DOI: 10.1039/c8ta09919g

3. Chaehyun Lim, Changmin Kim, **Ohhun Gwon**, Hu Young Jeong, Hyun-Kon Song, Young-Wan Ju, Jeeyoung Shin, and Guntae Kim*, Nano-perovskite oxide prepared via inverse microemulsion mediated synthesis for catalyst of lithium-air batteries, **Electrochimica Acta.** 275, 248-255 (2018)

4. Seona Kim, Ohhun Kwon, Changmin Kim, **Ohhun Gwon**, Hu Young Jeong, Ka-Hyun Kim*, Jeeyoung Shin*, and Guntae Kim*, Strategy for Enhancing Interfacial Effect of Bifunctional Electrocatalyst: Infiltration of Cobalt Nano Oxide on Perovskite, **Adv. Mater. Interfaces.** 5, 1800123 (2018)

5. Javeed Mahmood†, Feng Li†, Changmin Kim†, Hyun-Jung Choi, **Ohhun Gwon**, Sun-Min Jung, Jeong-Min Seo, Sung-June Cho, Young-Wan Ju*, Hu Young Jeong*, Guntae Kim*, and Jong-Beom Baek*, Fe@C2N: A Highly-Efficient Indirect-Contact Oxygen Reduction Catalyst, **Nano Energy.** 44, 304-310 (2018)

6. Junyoung Kim†, Areum Jun†, **Ohhun Gwon**, Seonyoung Yoo, Meilin Liu, Jeeyoung Shin, Tak-Hyoung Lim*, and Guntae Kim*, Hybrid-solid oxide electrolysis cell: a new strategy for efficient hydrogen production, **Nano Energy.** 44, 121-126 (2018)

7. Yunfei Bu*†, **Ohhun Gwon**†, Gyutae Nam, Haeseong Jang, Seona Kim, a Qin Zhong, Jaephil Cho*, and Guntae Kim*, A Highly Efficient and Robust Cation Ordered Perovskite Oxides as a Bi-Functional Catalyst for Rechargeable Zinc-Air Batteries, **ACS Nano.** 11, 11594-11601 (2017)

8. JongTae Yoo, Young-Wan Ju, Ye-Ri Jang, **Ohhun Gwon**, Sodam Park, Ju-Myung Kim, Chang Kee Lee, Sun-Young Lee, Sun-Hwa Yeon*, Guntae Kim*, and Sang-Young Lee*, One-pot surface engineering of battery electrode materials with metallic SWCNT-enriched, ivy-like conductive nanonets, **J. Mater. Chem. A.** 5, 12103-12112 (2017)

9. Chahwan Hwang†, **Ohhun Gwon**†, Hongil Jo, Kang Min Ok*, and Guntae Kim*, Major role of surface area in perovskite electrocatalysts for alkaline systems, **ChemElectroChem.** 4, 468-471 (2017)

10. **Ohhun Gwon**, Changmin Kim, Ohhun Kwon, Hu Young Jeong, Heai-Ku Park, Jeeyoung Shin, Young-Wan Ju*, and Guntae Kim*, An Efficient Oxygen Evolution Catalyst for Hybrid Lithium Air Batteries: Almond Stick Type Composite of Perovskite and Cobalt Oxide, **J. Electrochem. Soc.** 163, A1893-A1897 (2016)

11. Changmin Kim, **Ohhun Gwon**, In-Yup Jeon, Youngsik Kim, Jeeyoung Shin, Young-Wan Ju*, Jong-Beom Baek*, and Guntae Kim*, Cloud-like graphene nanoplatelets on $Nd_{0.5}Sr_{0.5}CoO_{3-d}$ nanorod as an efficient bifunctional electrocatalyst for hybrid Li-air batteries, **J. Mater. Chem. A.** 4, 2122-2127 (2016)

12. Dong-Gue Lee†, **Ohhun Gwon†**, Han-Saem Park, Su Hwan Kim, Juchan Yang, Sang Kyu Kwak, Guntae Kim*, and Hyun-Kon Song*, Conductivity-Dependent Completion of Oxygen Reduction on Oxide Catalysts, **Angew. Chem. Int. Ed.** 127, 15730–15733 (2015)

13. **Ohhun Gwon**, Seonyoung Yoo, Jeeyoung Shin*, and Guntae Kim*, Optimization of $La_{1-x}Sr_xCoO_{3-d}$ perovskite cathodes for intermediate-temperature solid oxide fuel cells through the analysis of crystal structure and electrical properties, **Int. J. Hydrogen Energy.** 39, 20806-20811 (2014)

14. Areum Jun, Seonyoung Yoo, **Ohhun Gwon**, Jeeyoung Shin, and Guntae Kim*, Thermodynamic and electrical properties of $Ba_{0.5}Sr_{0.5}Co_{0.8}Fe_{0.2}O_{3-d}$ and $La_{0.6}Sr_{0.4}Co_{0.2}Fe_{0.8}O_{3-d}$ for intermediate-temperature solid oxide fuel cells**, Electrochim. Acta.** 89, 372– 376 (2013)

Appendix II. Permissions

Chapter II. (from “Conductivity-Dependent Completion of Oxygen Reduction on Oxide Catalysts”, doi: 10.1002/ange.201508129)

License Number	4456200788549
License date	Oct 25, 2018
Licensed Content Publisher	John Wiley and Sons
Licensed Content Publication	Angewandte Chemie
Licensed Content Title	Conductivity-Dependent Completion of Oxygen Reduction on Oxide Catalysts
Licensed Content Author	Dong-Gyu Lee, Ohhun Gwon, Han-Saem Park, et al
Licensed Content Date	Nov 16, 2015
Licensed Content Volume	127
Licensed Content Issue	52
Licensed Content Pages	4
Type of use	Dissertation/Thesis
Requestor type	Author of this Wiley article
Format	Print and electronic
Portion	Full article
Will you be translating?	No
Order reference number	10.1002/ange.201508129
Title of your thesis / dissertation	Systematic Study on Electrocatalytic Properties of Perovskite Oxides for Energy Conversion and Storage Systems
Expected completion date	Nov 2019
Expected size (number of pages)	1
Requestor Location	Ohhun Gwon Ulsan Ulsan, other Korea, Republic Of Attn:
Publisher Tax ID	EU826007151
Total	0.00 USD
Terms and Conditions	

Chapter III. (from “Major Role of Surface Area in Perovskite Electrocatalysts for Alkaline Systems”, doi: 10.1002/celc.201600755)

License Number	4456200862155
License date	Oct 25, 2018
Licensed Content Publisher	John Wiley and Sons
Licensed Content Publication	ChemElectroChem
Licensed Content Title	Major Role of Surface Area in Perovskite Electrocatalysts for Alkaline Systems
Licensed Content Author	Chahwan Hwang, Ohhun Gwon, Hongil Jo, et al
Licensed Content Date	Jan 13, 2017
Licensed Content Volume	4
Licensed Content Issue	3
Licensed Content Pages	4
Type of use	Dissertation/Thesis
Requestor type	Author of this Wiley article
Format	Print and electronic
Portion	Full article
Will you be translating?	No
Order reference number	10.1002/celc.201600755
Title of your thesis / dissertation	Systematic Study on Electrocatalytic Properties of Perovskite Oxides for Energy Conversion and Storage Systems
Expected completion date	Nov 2019
Expected size (number of pages)	1
Requestor Location	Ohhun Gwon Ulsan Ulsan, other Korea, Republic Of Attn:
Publisher Tax ID	EU826007151
Total	0.00 USD
Terms and Conditions	

Chapter IV. (from “Enhancing Bifunctional Electrocatalytic Activities via Metal d-Band-Center-Lift in $Sm_{0.5}Sr_{0.5}CoO_{3-\delta}$ Perovskites”, This research will be published.)

Chapter V. (from "Optimization of $La_{1-x}Sr_xCoO_{3-\delta}$ perovskite cathodes for intermediate temperature solid oxide fuel cells through the analysis of crystal structure and electrical properties", doi: 10.1016/j.ijhydene.2014.07.137)

Chapter VI. (from “An Efficient Oxygen Evolution Catalyst for Hybrid Lithium Air Batteries: Almond Stick Type Composite of Perovskite and Cobalt Oxide”, doi: 10.1149/2.0571609jes)

License Number	4455970224806
License date	Oct 25, 2018
Licensed content publisher	Electrochemical Society, Inc
Licensed content title	Journal of the Electrochemical Society
Licensed content date	Jan 1, 1948
Type of Use	Thesis/Dissertation
Requestor type	Author of requested content
Format	Print, Electronic
Portion	chapter/article
The requesting person/organization is:	Ohhun Gwon, UNIST
Title or numeric reference of the portion(s)	An Efficient Oxygen Evolution Catalyst for Hybrid Lithium Air Batteries: Almond Stick Type Composite of Perovskite and Cobalt Oxide
Title of the article or chapter the portion is from	An Efficient Oxygen Evolution Catalyst for Hybrid Lithium Air Batteries: Almond Stick Type Composite of Perovskite and Cobalt Oxide
Editor of portion(s)	N/A
Author of portion(s)	N/A
Volume of serial or monograph.	N/A
Page range of the portion	
Publication date of portion	2019.01.01
Rights for	Main product
Duration of use	Life of current edition
Creation of copies for the disabled	no
With minor editing privileges	no
For distribution to	Worldwide
In the following language(s)	Original language of publication
With incidental promotional use	no
The lifetime unit quantity of new product	More than 2,000,000
Title	Systematic Study on Electrocatalytic Properties of Perovskite Oxides for Energy Conversion and Storage Systems
Institution name	Ulsan National Institute of Science and Technology (UNIST)
Expected presentation date	Nov 2019
Order reference number	doi: 10.1149/2.0571609jes
Billing Type	Invoice
Billing Address	Ohhun Gwon Ulsan Ulsan, Korea, Republic Of Attn: Ohhun Gwon

Chapter VII. (from “A Highly Efficient and Robust Cation Ordered Perovskite Oxide as a Bifunctional Catalyst for Rechargeable Zinc-Air Batteries”, 10.1021/acsnano.7b06595)

Acknowledgement

Thank you to all those who support writing this dissertation, and to the unforgettable experiences and memories. Although only my name was on the cover, I want to give them a special thanks for many contributed to my research and supported my life.

I would like to express my gratitude to my advisor Prof. Guntae Kim for the continuous support of my Ph.D study and research, for his patience, motivation, enthusiasm, and immense knowledge. His guidance helped me in all the time of research and writing of this dissertation. I could not have imagined having a better advisor and mentor for my Ph.D study.

Besides my advisor, I would like to thank the all of my committee members: Prof. Jong-Beom Baek, Prof. Hu Young Jeong, Prof. Jeeyoung Shin, and Prof. Ikwhang Chang for very gracious and generous with their time, ideas, their encouragement, and insightful comments.

My great co-advisor, Professor Jeeyoung Shin has been always there to listen and give advice. I am deeply grateful to him for the long discussions that helped me sort out the technical details of my research.

I am also grateful to my gunslab members for their many helps and great memories: Dr. Seonyoung Yoo, Prof. Sivaprakashi Sengodan, Prof. Sihyuk Choi, Dr. Areum Jun, Ms. Jiyoun Kim, Ms. Seonhye Park, Dr. Junyoung Kim, Prof. Young-Wan Ju, Prof. Yunfei Bu, Dr. Arunchander Asokan, Seona Kim, Chaehyun Lim, Ohhun Kwon, Changmin Kim, Donghwi Jeong, Sangwook Joo, Jeongwon Kim, Gihyun Kim, Hyunmin Kim, Seongtae Lee, Hansol Lee, Arim Seong, and Yejin Yang. Studying for years would have been impossible without them. I wish you all the best for your work and would be always be happy to hear good news.

I also appreciate to my friends for always standing by my side and for always making me feel happy.

Last, but foremost, I would also like to thank my parents, brother and all of my family for their endless love, understanding, and support. They were always supporting me and encouraging me with their best wishes.